



저작자표시-비영리-변경금지 2.0 대한민국

이용자는 아래의 조건을 따르는 경우에 한하여 자유롭게

- 이 저작물을 복제, 배포, 전송, 전시, 공연 및 방송할 수 있습니다.

다음과 같은 조건을 따라야 합니다:



저작자표시. 귀하는 원저작자를 표시하여야 합니다.



비영리. 귀하는 이 저작물을 영리 목적으로 이용할 수 없습니다.



변경금지. 귀하는 이 저작물을 개작, 변형 또는 가공할 수 없습니다.

- 귀하는, 이 저작물의 재이용이나 배포의 경우, 이 저작물에 적용된 이용허락조건을 명확하게 나타내어야 합니다.
- 저작권자로부터 별도의 허가를 받으면 이러한 조건들은 적용되지 않습니다.

저작권법에 따른 이용자의 권리는 위의 내용에 의하여 영향을 받지 않습니다.

이것은 [이용허락규약\(Legal Code\)](#)을 이해하기 쉽게 요약한 것입니다.

[Disclaimer](#)

공학박사 학위논문

**Nucleation and Growth Studies of  
Graphene Synthesis on Cu Surfaces**

구리 표면 위에서의 그래핀 합성에 대한 핵 생성  
및 성장 연구

2015년 2월

서울대학교 대학원

재료공학부

조성용



# Nucleation and Growth Studies of Graphene Synthesis on Cu Surfaces

지도 교수 김 기 범

이 논문을 공학박사 학위논문으로 제출함

2015 년 2 월

서울대학교 대학원

재료공학부

조 성 용

조성용의 공학박사 학위논문을 인준함

2015년 2월

위 원 장 \_\_\_\_\_ 김 미 영 \_\_\_\_\_ (인)

부위원장 \_\_\_\_\_ 김 기 범 \_\_\_\_\_ (인)

위 원 \_\_\_\_\_ 남 기 태 \_\_\_\_\_ (인)

위 원 \_\_\_\_\_ 이 정 수 \_\_\_\_\_ (인)

위 원 \_\_\_\_\_ 박 성 준 \_\_\_\_\_ (인)



# **Nucleation and Growth Studies of Graphene Synthesis on Cu Surfaces**

구리 표면 위에서의 그래핀 합성에 대한 핵 생성  
및 성장 연구

A DISSERTATION SUBMITTED TO  
DEPARTMENT OF MATERIALS SCIENCE AND ENGINEERING  
SEOUL NATIONAL UNIVERSITY

FOR THE DEGREE OF  
DOCTOR OF PHILOSOPHY

Seong-Yong Cho

February 2015



## **Abstract**

In this dissertation, two major issues of graphene growth and solutions for two issues were discussed. First issue is developing transfer-free graphene growth process on target substrate (chapter 3 and 4) and the other issue is study on graphene growth and obtaining high-quality and large grain size graphene via understanding nucleation and growth kinetics (chapter 5 and 6).

In introductory part (chapter 1 and 2), general overview on graphene and growth methods is presented. Literature survey on previous graphene growth work and motivation for following work in this dissertation are also covered in chapter 1. In the chapter 2, review on various approaches for obtaining high-quality graphene will be covered based on its fundamental aspects of nucleation and growth. The relationships between each parameters of growing graphene and properties of as-grown graphene are discussed.

In chapter 3, a rapid graphene growth method that can be carried out on any desired substrate, including insulator, thus negating the need for the transfer from metal substrate is introduced. Rapid annealing of a bilayer of a-C and metal deposited on the surface leads to the formation of graphene film, and to subsequent breaking-up of the thin metal layer underneath the film, resulting in a formation of a graphene-metal hybrid film which is both transparent and electrically conducting.

In chapter 4, graphene film on silicon substrates having various orientations by simple heating in the presence of carbon source gas is discussed. We observed that a 3C-SiC (111) film would form upon carburizing silicon with carbon deposited from a carbon source because it is well lattice-matched with Si (110) (less than 2 %). Graphene grew on the buffer layer of 3C-SiC (111). The surface

consists of hexagonal arrays that can act as a template for graphene growth.

In chapter 5, the effect of gas transport inside a micrometre-scale jig gap on the growth of graphene on Cu foil located in the gap is reported. Due to the small size of the gap, a boundary layer is fully developed inside the gap, and the gas molecule transport is controlled by the molecular flow. First, the Cu surface is protected from the sublimation and re-deposition of Cu during pre-annealing, which results from the relatively static gas environment of the molecular gas flow. Second, suppression of the gas conductance resulted in strongly reduced overall graphene coverage with a smaller average grain size but with almost the same density as that of the graphene nuclei. Furthermore, the suppression of gas conductance leads to the formation of well-bounded graphene morphology instead of a dendritic morphology.

In chapter 6, continuous graphene layer was grown on top of liquid Cu surface and grain boundaries were revealed by SEM (Scanning electron microscopy) and optical characterization via Cu oxidation. Hydrogen etch revealed the grain boundaries of graphene on liquid Cu easily. Small gaps exist between graphene islands even after few hours of growth time, thus,  $\text{CH}_4$  flux was increased at the final step of chemical vapor deposition growth in order to confirm the stitching of graphene islands. Hydrogen etch and optical characterization clearly demonstrated that graphene islands are uniform before and even after the merging of its graphene grains and tiny gaps between graphene islands were fully stitched by two-step growth method. Transmission electron microscopy images and diffraction pattern study revealed the importance of self-assembly. The resistance was measured by TLM (Transfer length measurement) pattern. Grain boundary resistance was considered to be negligible if two grains meet in the same direction

without rotation of atomic lattice on liquid Cu, which has a great impact compared to typical grain boundary.

In conclusion, novel graphene growth methods for direct formation on target substrate were suggested. Also, based on the fundamental understanding of nucleation and growth of graphene synthesis, two approaches are studied which are enlarging grain size and self-assembly. Graphene growth on catalytic metal surfaces is governed by heteronuclei effect, and overcoming way is self-assembly via growth on liquid catalyst according to this study.

**Key words:** graphene, transparent conducting film, transfer-free, direct formation, SiC, Ni, Cu, nucleation and growth, heteronuclei, gas transport, jig, Mesoepitaxy, liquid Cu, Self-assembly

**Student number:** 2009-20638

## Table of contents

Abstract .....	i
List of tables .....	vii
List of figures .....	ix
<b>CHAPTER 1. Introduction .....</b>	<b>1</b>
1.1. Graphene as a two-dimensional material .....	3
1.1.1. General overview of graphene .....	3
1.1.2. Physical properties of graphene.....	
8	
1.2. Alternative graphene growth methods .....	
1	1
1.2.1. Reduction of graphene oxides .....	
1	1
1.2.2. Epitaxial growth (sublimation of SiC) .....	11
1.2.3. Chemical vapor deposition .....	
1	2
1.3. Understanding on graphene growth on Cu .....	
1	4
1.3.1. Graphene synthesis on Cu vs. Ni .....	14
1.3.2. Unique aspects of graphene growth on Cu .....	15
1.3.3. Motivation for work: Transfer issue and polycrystalline nature .....	
1	7
References .....	23

<b>CHAPTER 2. Review on graphene growth on Cu .....</b>	<b>9</b>
<b>2</b>	<b>9</b>
2.1. Introduction .....	31
2.2. Observation of growth kinetics .....	31
2.3. Surface treatment of Cu foil .....	38
2.4. Effect of growth temperature .....	43
2.5. Source gas feeding rate .....	45
2.6. Morphology evolution and hydrogen etching .....	47
2.7. Approaches for large single crystal graphene .....	
5	2
2.7.1. Gas transport control .....	52
2.7.2. Seeded growth .....	53
2.7.3. Graphene growth on liquid Cu .....	55
References .....	58
 <b>CHAPTER 3. Direct graphene growth on target substrate: Metal- induced crystallization of a-C .....</b>	 <b>3</b>
<b>6</b>	<b>3</b>
3.1. Introduction .....	65
3.2. Experimental details .....	68
3.2.1. Deposition and sample preparation .....	68
3.2.2. Analysis of the film .....	69
3.3. Results and discussion .....	
7	2

3.4. Summary and conclusions .....	8	4
References .....		85

**CHAPTER 4. Direct graphene growth: Graphene formation by direct carbon source feeding on Si substrate .....**

<b>8</b>	<b>7</b>
4.1. Introduction .....	89
4.2. Experimental details .....	92
4.3. Results and discussion .....	
9	4
4.4. Summary and conclusions .....	103
References .....	104

**CHAPTER 5. Gas transport control in graphene growth: Micro-meter scale gap jig effect .....**

<b>1</b>	<b>0</b>	<b>7</b>
5.1. Introduction .....		109
5.2. Experimental details .....		
1	1	1
5.3. Results and discussion .....		
1	1	4
5.3.1. Jig effect on pre-annealing .....		114
5.3.2. Gas transport effect on graphene growth .....		117
5.3.3. Morphology evolution of graphene grains .....		

1	2	5
5.4. Summary and conclusions .....		
1	2	9
References .....		130
<b>CHAPTER 6. Mesoepitaxy: Graphene growth on liquid Cu .....</b>		
<b>1</b>	<b>3</b>	<b>3</b>
6.1. Introduction .....		135
6.2. Experimental details .....		139
6.2.1. Graphene growth on liquid Cu and two-step growth .....		
1	3	9
6.2.2. Transfer and VDP pattern fabrication .....		139
6.2.3. Liftoff and TLM patterning .....		
1	4	0
6.3. Results and discussion .....		
1	4	1
6.3.1. Structural study of graphene grown on liquid Cu .....		
1	4	2
6.3.2. Revealing grain boundaries of graphene on liquid Cu .....		148
6.3.3. Two-step growth for continuous graphene .....		153
6.3.4. Electrical transport study .....		
1	5	8
6.4. Summary and conclusions .....		163
References .....		164



## **List of tables**

### **CHAPTER 1**

**Table 1-1.** Comparison of various properties and aspects of carbon allotrope including fullerene, carbon nanotube, and graphene.

**Table 1-2.** Maximum graphene flake size and electron mobility obtained from various graphene growth methods.

**Table 1-3.** Summary of advantages and drawbacks of each graphene growth method.

**Table 1-4.** Thermochemical data (enthalpy, entropy and Gibbs free energy) of thermal decomposition reactions for typical hydrocarbon source used for graphene growth.

### **CHAPTER 2**

**Table 2-1.** Domain shape, grain growth rate and maximum grain size of each graphene growth methods from literature which were calculated from SEM figures.

### **CHAPTER 4**

**Table 4-1.** Advantages and disadvantages of SiC epitaxial growth of graphene, CVD growth of SiC and followed sublimation, and direct deposition of graphene on SiC substrate.

**Table 4-2.** Relative orientation of Si surface and 3C-SiC planes formed by carburization process

## List of figures

### CHAPTER 1

**Figure 1-1.** Carbon allotropes and basic unit (graphene). Assembly of 60 carbons forms fullerene, stacking of graphene sheet forms graphite, and rolling up of graphene sheet forms carbon nanotube.

**Figure 1-2.** Typical optical microscope image of mono-, bi-, multi-layer graphene and graphite obtained from HOPG by mechanical exfoliation on oxidized Si substrate.

**Figure 1-3.**  $C^{12}$  and  $C^{13}$  isotope labeling experiment revealed by micro-Raman mapping on graphene grown on Ni and Cu. Graphene grown on Cu surface shows surface diffusion dominant growth and graphene grown on Ni shows randomly mixed carbon isotope due to precipitation of carbon atoms

**Figure 1-4.** Growth curves calculated by G. Eres *et al.*, and coverage as a function of growth time measured by X. Li and G. Eres *et al.*, which correspond to typical JMA equation.  $\theta$  means coverage and  $t/\tau$  means normalized growth time.

**Figure 1-5.** Schematic illustration of graphene growth on catalytic Cu surfaces showing random orientation of nuclei formation. Further growth results in polycrystalline film.

## CHAPTER 2

**Figure 2-1.** Schematic illustration for direct optical visualization of graphene islands on Cu substrate by oxidizing Cu surfaces which is not covered by graphene.

**Figure 2-2.** Atomic-resolution ADF (annular dark field)-STEM images of graphene domain boundaries observed by P. Y. Huang *et al.*, (a) Low magnification image showing TEM grid opening, (b) perfect graphene lattice, (c) atomic resolution image of graphene grain boundary and (d) atomic structure of grain boundary is drawn on (c).

**Figure 2-3.** (a) Bright field TEM image of two graphene grains showing different orientations of diffraction pattern, (b) metal electrodes on individual graphene grains touching each other, and (c) resistance of intra and inter-graphene grains.

**Figure 2-4.** AFM RMS (root-mean square) surface roughness measurement of various Cu foil before and after annealing. Foil A is 25  $\mu\text{m}$ -thick and purity of Cu is 99.8 % from Alfa Aesar (product #: 13382, unpolished), foil B is 25  $\mu\text{m}$ -thick and purity of Cu is 99,999 % from Alfa Aesar (product #: 10950, unpolished), and foil C is 50  $\mu\text{m}$ -thick and purity of Cu is 99.999 % from Alfa Aesar. Annealing temperature is 1050  $^{\circ}\text{C}$  at atmospheric pressure ( $\text{Ar}+\text{H}_2$ ).

**Figure 2-5.** (a) Schematic illustration of graphene growth on active site of Cu surface and (b) to (g) systematic control of surface treatment and growth

parameters in CVD graphene growth and typical graphene domain sizes from each recipe reported by Z. Yan *et al.*, E1 denotes typical graphene growth at 1060 °C, E2 denotes decreased CH<sub>4</sub> flux, E3 denotes high pressure annealing and electropolished, E4 denotes increased growth pressure, E5 denotes increased growth temperature and E6 denotes further increased growth temperature.

**Figure 2-6.** SEM images of partially grown graphene under different growth conditions: T (°C)/J<sub>CH<sub>4</sub></sub> (sccm)/P<sub>CH<sub>4</sub></sub> (mTorr): (a) 985/35/460, (b) 1035/35/460, (c) 1035/7/460, (d) 1035/7/160, Scale bars indicate 10 μm.

**Figure 2-7.** SEM images of graphene flakes grown on a liquid Cu surface with different shapes formed by varying the Ar/H<sub>2</sub> ratio and CH<sub>4</sub> gas flow. All the scale bars indicate 5 μm.

**Figure 2-8.** Pre-patterned graphene seeds and regrown graphene islands. (a) Graphene seed which were formed by pre-growth and e-beam lithography patterning, (b) Typical graphene grains after re-growth, (c) further growth results in larger grains, and (d) Low magnification image showing different growth behavior of graphene growth with seed area and random nucleation.

### CHAPTER 3

**Figure 3-1.** (a) Photographs of as-deposited, and annealed (from 300 °C to 800 °C in sequence) nickel film (without a-C). (b) Transmittance value of (a) at the

wavelength range of visible rays. (c) SEM image of 800 °C annealed sample showing nickel nano-crystallite. (Scale bar indicates 100 nm)

**Figure 3-2.** (a) Diagram showing the formation of the graphene-metal hybrid by metal-induced crystallization of a-C and agglomeration of ultra-thin metal film, (b) Bird's eye view of the film.

**Figure 3-3.** (a) Photographs of various thickness of as-deposited a-C. (b) Transmittance value of (a) at the wavelength range of visible rays. (c) Sheet resistance value of (a).

**Figure 3-4.** Sheet resistance versus transmittance curve of each samples made of various thickness of nickel catalyst, annealing temperature from 300 °C to 800 °C (a-C thickness was fixed as 1nm).

**Figure 3-5.** (a) Raman spectra of as-deposited and 300 °C, 400 °C, 500 °C, and 600 °C annealed bi-layer (Ni 10nm / a-C 1nm) sample. (b) Raman spectra of bilayer structure with various Ni thicknesses at annealing temperature of 500 °C. (c) Correlation between D/G peak ratio and sheet resistance (unit:  $\Omega/\text{sq.}$ ) of 600 °C (chosen as an arbitrary temperature, similar behaviors were shown at different temperature) annealed at each thickness of metal catalyst.

**Figure 3-6.** Raman spectra of as-deposited a-C and crystallized graphene layers on top of continuous nickel (350 nm) after heat treatment at various annealing temperatures. (Initial a-C layer was deposited on top of Ni in order to understand

crystallization behavior of a-C on thick Ni) (b) Estimated grain size of graphene based on D/G peak intensity ratio.

**Figure 3-7.** Plan-view TEM images of as-deposited (a), (b) 3-nm-thick, (c), (d) 10-nm-thick, and (e), (f) 30-nm-thick nickel films on carbon grid. (a), (c), (e) indicate bright-field TEM images and (b), (d), (f) indicate high-resolution TEM images. Scale bar in (a), (c), (e) corresponds to 20 nm.

**Figure 3-8.** Raman spectra of as-deposited a-C and crystallized graphene layers on top of continuous nickel (350 nm) after heat treatment at various annealing temperatures. (Initial a-C layer was deposited on top of Ni in order to understand crystallization behavior of a-C on thick Ni) (b) Estimated grain size of graphene based on D/G peak intensity ratio.

**Figure 3-9.** (a) Photographs of as-deposited, and annealed (300, 500, 700, and 900 °C) samples for Ni 3nm / a-C 1nm bilayer structure. (b) Transmittance curve at visible wavelength of samples in a). (c) plan-view bright field TEM image of 500 °C annealed bilayer structure (Ni 3nm / a-C 1nm). Scale bar in (c) indicates 200 nm.

**Figure 3-10.** (a) Cross-sectional TEM image of graphene-metal hybrid film layers (from Ni 10 nm / a-C 3 nm structure, annealed at 600 °C). (thicker a-C layer was used for better observation of graphene layers formed by UTMIC) (b) cross-

sectional TEM image of (a) structure showing that nickel agglomerate is surrounded by graphene layers.

## CHAPTER 4

**Figure 4-1.** Schematics showing graphene formation on SiC/Si substrate by direct carbon feeding.

**Figure 4-2.** (a) FT-IR spectra of the carburized (110) Si substrate as a function of annealing temperature, and (b) Raman spectra of the as-prepared Si substrate and graphene/3C-SiC(111)/Si(110) after 1,100 °C annealing for 1minute. Incident wavelength of laser was 532nm. Spectral resolution was  $1.47 \text{ cm}^{-1}$  and (c) Low magnification cross-sectional TEM image of graphene/3C-SiC(111)/Si(110) structure.

**Figure 4-3.** (a) High resolution TEM image of graphene/3C-SiC(111)/Si(110) structure, line profile indicating inter-layer distance, and FFT image from Si [111] zone axis, (b) high resolution TEM image of 3C-SiC (100) / Si (100) structure after carbon feeding, and FFT image (zone axis of Si is [110]), and (c) high resolution TEM image of 3C-SiC (111)/Si (111) structure after carbon feeding ,and FFT image (zone axis of Si is [110]). All the scale bars indicate 5 nm.

**Figure 4-4.** Expected interface crystallographic orientations of 3C-SiC(111)/Si(110), which causes only a 2% lattice misfit by finding well-matching

epitaxial plane. Carbon atoms in 3C-SiC is omitted for simple visualization.

**Figure 4-5.** XPS C 1s signal from graphene layers formed by carburization of (110) Si substrate at 1,100 °C. X-ray source is from Mg K<sub>α</sub>.

## CHAPTER 5

**Figure 5-1.** (a) Photographs of as-deposited, and annealed (from 300 °C to 800 °C in sequence) nickel film (without a-C). (b) Transmittance value of (a) at the wavelength range of visible rays. (c) SEM image of 800 °C annealed sample showing nickel nano-crystallite. (Scale bar indicates 100 nm)

**Figure 5-2.** (a) Photograph of Cu foil after pre-annealing using the micrometer-gap jig, showing clear evidence of the surface protection effect; (b) optical microscopy (OM) image of the Cu foil near the jig entrance; (c) magnified OM image of the jig exterior region (left section of (b)); and (d) magnified OM image of the jig interior region (right section of (b)). Pre-annealing: 1035 °C for 1 h.

**Figure 5-3.** SEM images of graphene grown on Cu foil with varied micrometer-gap jigs. (a) SEM images of the Cu foil when the jig gap is 1 mm taken at different positions with respect to the jig entrance and at the lateral positions marked above. SEM images of the Cu foil when the jig gap is (b) 500 μm, (c) 200 μm, and (d) 100 μm. Scale bar indicates 50 μm.

**Figure 5-4.** (a) Typical Raman spectrum of graphene fully grown on Cu foil after the transfer to a SiO<sub>2</sub> (285 nm)/Si substrate when the jig is applied after an extended growth time of 30 min. (b) Optical microscope image of graphene islands after transfer. (c) G-band micro-Raman mapping analysis over a 50 × 50 μm area with a step size of 1 μm for the area depicted in (b). A 532-nm DSSP laser and X100 objective lens were used.

**Figure 5-5.** (a) Fraction of graphene-covered area in SEM images in Fig. 3 as a function of lateral distance ( $D_L$ ) from the jig entrance when the jig gap ( $D_V$ ) varies from 1 mm to 100 μm and (b) fraction of graphene covered area in the SEM images as a function of  $D_L/D_V$ .

**Figure 5-6.** Average grain size of graphene islands as a function of lateral distance at each jig gap spacing and (b) nuclei density as a function of lateral distance ( $D_L$ ) at each jig gap spacing ( $D_V$ ).

**Figure 5-7.** SEM images showing the gas source suppression effect when the jig is used for graphene growth. (a) SEM image of typical graphene islands grown outside the jig. (b) SEM image of graphene seeds grown inside the jig. The graphene islands and seeds in (a) and (b) were from the same foil and were subjected to the same growth conditions. (Graphene growth was carried out at 1035 °C for 3 min; CH<sub>4</sub>, H<sub>2</sub>, and Ar fluxes were 1, 5, and 16 sccm, respectively). The inset depicts the well-defined grain morphology of graphene grown in the jig interior under the same conditions as (b) with extended growth time.

**Figure 5-8.** SEM images of graphene grown on Cu foil when a micrometer-gap jig is applied for gas transport control. SEM images of (a) the fully grown graphene film on the jig exterior, (b) 5 mm from the jig entrance, (c) 10 mm from the jig entrance, (d) 15 mm from the jig entrance, and (e) 20 mm from the jig entrance. CH<sub>4</sub> and H<sub>2</sub> flux: 2 sccm and 6 sccm, respectively. Scale bar indicates 50 μm.

## CHAPTER 6

**Figure 6-1.** Schematic illustration of graphene growth on liquid Cu and characterization of graphene growth (a) Schematic illustration of graphene growth on liquid Cu, (b) optical microscope image of as-grown graphene islands on liquid Cu/W support for 30 minutes of growth time showing self-assembled growth behavior, (after oxidizing Cu foil for observation of graphene islands due to selective oxidation) (c) SEM image of graphene grown on liquid Cu. Scale bar indicates 20 μm.

**Figure 6-2.** Schematic illustration of two-step graphene growth on liquid Cu. Process (1) describes continuous graphene layer formation on liquid Cu and followed cooling forms crack due to thermal stress induced by solidification of underlying Cu, and process (2) describes two-step growth after cooling Cu catalyst and no observable cracks formation.

**Figure 6-3.** Optical microscope images of graphene grown on liquid Cu varying

CH<sub>4</sub> flux. (a) CH<sub>4</sub> flux is 4 sccm, (b) 3.8 sccm, (c) 3.6 sccm, (d) 3.5 sccm, (e) 3.3 sccm, respectively.

**Figure 6-4.** Optical microscope images of graphene grown on liquid Cu at 5 minutes (a), 10 minutes (b) and 30 minutes (c), and (d) and (e) are magnified image of (a) and (b), respectively.

**Figure 6-5.** TEM studies of graphene grown on liquid Cu. (a) SEM image of graphene transferred to Quantifoil TEM grid, (b) TEM bright field image of (a) (images are inverted with respect to vertical axis due to TEM sample loading), and (c) diffraction patterns obtained from various positions marked in (b).

**Figure 6-6.** TEM analysis of three adjacent graphene grains on liquid Cu after transfer to TEM grid, (a) bright field image of grains, and (b) diffraction patterns of each position marked in (a).

**Figure 6-7.** SEM image of graphene on liquid Cu for 4 hours under optimized condition. (a) Typical graphene film on liquid Cu, (b) visible voids and revealed grain boundaries (indicated by arrows), (c) SEM image of grain boundaries clearly revealed by stopping growth and relatively wide gaps are indicated by arrows and (d) magnified image of (c).

**Figure 6-8.** (a) SEM image of graphene islands after 30 minutes of growth time, (b) SEM image of graphene after 2 hours of growth, (c) SEM image of graphene after

H<sub>2</sub> etching for 5 minutes of (b), and (d) SEM image of graphene after 5 minutes H<sub>2</sub> etching

**Figure 6-9.** (a) SEM image of semi-continuous graphene layer (just before stitching) and tearing of graphene islands can be clearly observed by solidification of underlying Cu, (b) SEM image of crack formation on continuous graphene layer which cannot release thermal stress induced solidification of Cu.

**Figure 6-10.** Optical microscope image of graphene layer transferred to SiO<sub>2</sub>/Si substrate showing crack and tearing due to thermal stress and transfer damage

**Figure 6-11.** SEM and optical characterization of continuous graphene layer formation by two-step growth. (a) SEM image of continuous graphene layer grown by two-step method, (b) graphene layer of (a) after experiencing hydrogen etching process, (c) optical microscope image of graphene layer (single step) on Cu after NaCl-assisted oxidation process, (d) optical microscope image of graphene layer on liquid Cu by two-step growth and no damages were observed.

**Figure 6-12.** Comparison of electrical transport properties of graphene grown on solid and liquid Cu. (a) Sheet resistance of graphene grown on typical solid and liquid Cu catalyst, (b) Hall mobility of graphene grown on solid and liquid Cu catalyst.

**Figure 6-13.** (a) Optical microscope image of two adjacent graphene islands which aligns in the same orientation and Ti/Au electrodes were deposited by lift-off

process, (b) current vs. applied bias curve from electrode #1 to various one including intra- and inter-grain.

# CHAPTER 1.

## **Introduction**



## 1.1. Graphene as a two-dimensional material

### 1.1.1. General overview of graphene

Graphene is a two-dimensional (2D) structure of hexagonal carbon  $sp^2$  lattice, which consists of a single sheet of graphite. Using tight-binding description model, the dispersion relation describes energy of the electrons with wave vector  $K$  is<sup>1,2</sup>

$$E = \pm\sqrt{\gamma_0^2\left(1 + 4\cos^2\frac{k_y a}{2} + 4\cos\frac{k_y a}{2} \cdot \cos\frac{k_x\sqrt{3}a}{2}\right)} \quad \dots 1-(1)$$

with the nearest-neighbor hopping energy  $\gamma_0 = 2.8 \text{ eV}$  and the lattice constant  $a \approx 2.46 \text{ \AA}$ . The conduction and valence bands, respectively, correspond to the different signs; they touch each other at six points, the “K-values” of the two-dimensional hexagonal Brillouin zone. Two of these points are independent, while the rest are equivalent by symmetry. The simplified equation describing the electrons’ linear dispersion relation is

$$E = \hbar v_F \sqrt{k_x^2 + k_y^2} \quad \dots 1-(2)$$

where the wave vector  $k$  is measured from the Dirac points (the zero of energy is chosen here to coincide with the Dirac points). This zero-gap semiconductor shows unique electronic properties which is quite different from other condensed matter systems. The theoretical studies was explored by P. R. Wallace in 1947 as a starting point for understanding the electronic properties of 3D graphite,<sup>1</sup> but single layer graphene was considered not to be existing in nature. The 2D crystal was first produced by Geim and Novoselov at the University of Manchester in 2004, and the method is simply exfoliating isolated single sheet of graphite from highly oriented pyrolytic graphite (HOPG) using adhesive tape on thermally oxidized silicon

wafer.<sup>3,4</sup> And, according to their report, graphene shows extraordinary behavior compared to previous Si based semiconductor. Ultra high electron mobility and quantum Hall effect are discovered in exfoliated graphene.<sup>5-8</sup> Thus, graphene has attracted a great interest of researchers and other two-dimensional systems such as *h*-BN, MoS<sub>2</sub> became new research field.

Before the era of two-dimensional atomic carbon sheet, other allotrope of carbon structure were already studied as shown in Table 1-1 and Figure 1-1.<sup>9,10</sup> Fullerene and carbon nanostructure have been investigated due to superior electrical transport behavior. 2D structure of graphene has attracted a great interest due to compatibility to thin film and lithography process contrary to previous carbon nanostructure which is hard to be applied for thin film process. Compared to carbon nanotube (CNT) which is classified into single-walled CNT and multi-walled CNT, and even semiconducting or metallic CNT, graphene doesn't have to be considered for its orientation and chirality. Typical graphene obtained from mechanical exfoliation method is shown in Figure 1-2. Optical interference of graphene on 300-nm-thick SiO<sub>2</sub>/Si substrate enhances contrast and graphene thickness can be easily figured out.<sup>11,12</sup>

	Fullerene	Carbon nanotube	graphene
Discovery	1985, Smalley	1991, Iijima	2004, Geim
Dimension	0D	1D	2D
Chirality	No	Yes	No
Classification	$C_{60}$ , $C_{70}$ , $C_{240}$ , $C_{540}$ , $C_{950}$	Single/multi-walled Metallic/semiconducting	Sheet
Processibility	Bottom-up	Bottom-up (Solution)	Top-down (Transfer)

**Table 1-1.** Comparison of various properties and aspects of carbon allotrope including fullerene, carbon nanotube, and graphene.

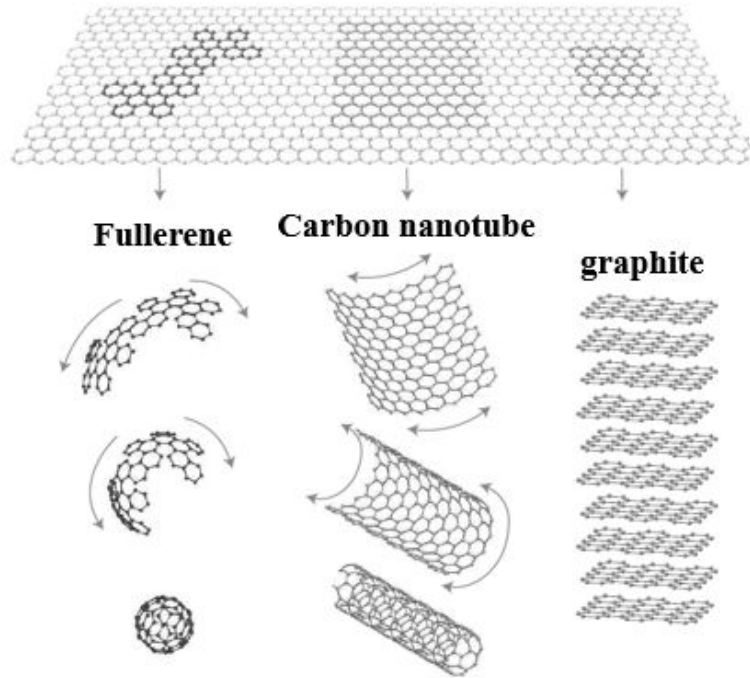


**Figure 1-1.** Carbon allotropes and basic unit (graphene). Assembly of 60 carbons forms fullerene, stacking of graphene sheet forms graphite, and rolling up of graphene sheet forms carbon nanotube. Figure adapted from [13]

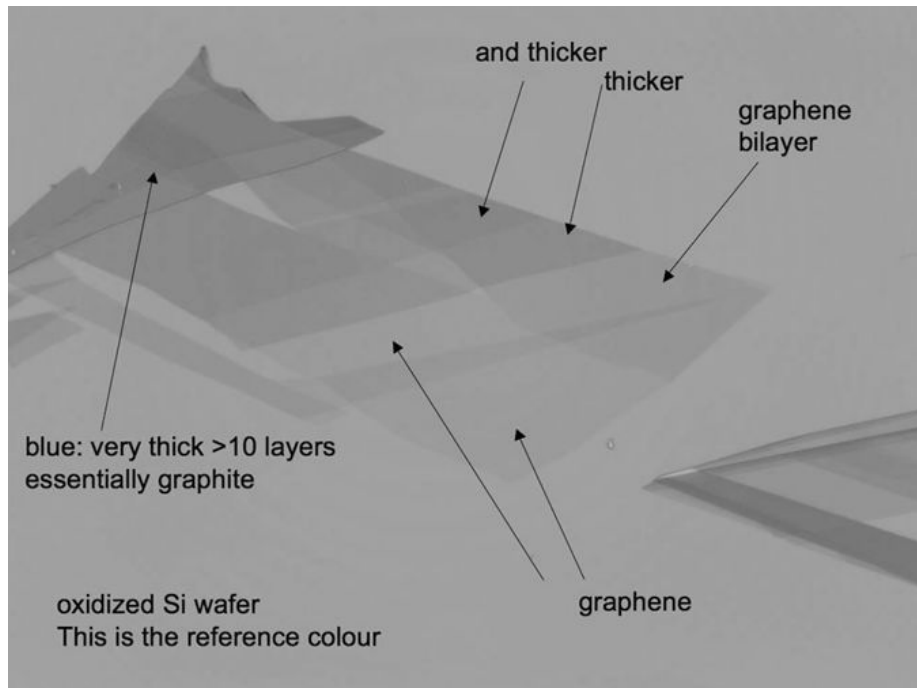


**Figure 1-2.** Typical optical microscope image of mono-, bi-, multi-layer graphene and graphite obtained from HOPG by mechanical exfoliation on oxidized Si substrate. Figure adapted from [14]

### 1.1.2. Physical properties of graphene

Outstanding electrical, optical, mechanical, thermal and optical properties were reported via mechanical exfoliation method by scotch tape. Graphene is believed to play vital role in future nanoelectronics such as ballistic transistors,<sup>15,16</sup> field emitter,<sup>17</sup> components of integrated circuits,<sup>18</sup> transparent conducting electrodes<sup>19-22</sup> and even sensors.<sup>23</sup> Freestanding graphene device was fabricated via mechanical exfoliation of HOPG to thermally oxidized Si substrate and followed wet-etch of SiO<sub>2</sub>. Achieved electron mobility was 230,000 cm<sup>2</sup>/V·sec which is two orders higher than that of Si.<sup>6</sup> The corresponding resistivity of the graphene sheet would be 10<sup>-6</sup> Ω·cm, less than the resistivity of silver, one of the lowest resistivity substances known at room temperature. Due to roughness of surface and carrier trap on SiO<sub>2</sub>, graphene on SiO<sub>2</sub> shows lower electron mobility compared to suspended graphene.<sup>24</sup> The values of electron mobility of various graphene are shown in Table 1-2. Despite of surface scattering and roughness of substrate, suspended graphene shows the highest electron mobility, and graphene on *h*-BN shows relatively high electron mobility.<sup>25</sup> Also, compared to exfoliated graphene,<sup>26,27</sup> graphene on Cu<sup>28</sup> and SiC<sup>29,30</sup> shows lower electron mobility which is expected to be polycrystalline nature and reduced graphene oxide<sup>31</sup> shows the lowest mobility value.

According to the report by P. R. Nair,<sup>32</sup> only 2.3 % of light can be absorbed by single layer graphene which means that graphene has 97.7 % of transmittance at visible light which makes graphene as a good candidate for optoelectronic devices. Even, monolayer graphene is distinguishable on thermally oxidized Si wafer, which is a result of interference between graphene/SiO<sub>2</sub>/Si.<sup>11,33-35</sup> In this aspect,

graphene is considered as a candidate material replacing current ITO (Sn-doped indium oxide) and other semiconductor oxides for transparent conducting film due to its high transmittance at visible wavelength compared to low electrical resistance.<sup>19-22</sup> Moreover, graphene is stretchable and highly resistant to mechanical bending and other tension because it consists of carbon bonds, otherwise, it breaks down like oxide semiconductors which is ionic bonding based material.

Also, graphene is one of the strongest materials known with a breaking strength over 100 times greater than a hypothetical steel film of the same thickness, with a Young's modulus of 1 TPa.<sup>36</sup> The spring constant of suspended graphene sheets has been measured using an atomic force microscope (AFM). Graphene sheets, held together by van der Waals forces, were suspended over SiO<sub>2</sub> cavities where an AFM tip was probed to test its mechanical properties. Its spring constant was in the range 1 – 5 N/m and the stiffness was 0.5 TPa, which differs from that of bulk graphite. These high values make graphene very strong and rigid.

Although graphene is atomically single layer thick, its barrier property is very outstanding. Oxygen molecules cannot penetrate through graphene layer and anti-oxidation property of graphene was studied.<sup>37</sup> Large surface-to-volume ratio enables graphene as a future candidate for sensor<sup>38</sup> and catalyst material.

Methods	Maximum flake size (mm)	RT carrier mobility ( $\text{cm}^2/\text{V}\cdot\text{sec}$ )	Ref.
Exfoliation	~ 1	~ $1 * 10^5$	[26], [27]
CVD on Cu	~ 1000	10,000	[21], [28]
Epitaxial growth on SiC	~ 100	10,000	[29], [30]
Reduced graphene oxide	~ 1000	~ 1	[31]

**Table 1-2.** Maximum graphene flake size and electron mobility obtained from various graphene growth methods.

## **1.2. Alternative graphene growth methods**

Mechanical exfoliation provides high performance graphene flakes, but graphene size is limited to tens of microns and the method is not reproducible. Undoubtedly, large scale and high quality graphene growth process is highly demanded for industrial application. Several synthesis methods have been suggested so far as below to replace micromechanical cleavage method.

### **1.2.1. Reduction of graphene oxides**

Liquid phase exfoliation of graphene oxide (GO) and reduction of GO is useful for large area synthesis on any substrate.<sup>39</sup> Graphite is usually hydrophobic and dispersion is hard to occur in water environment. Thus, graphite is oxidized and then GO is dispersed in aqueous solution. Few layers or single layer of GO flakes are reduced on target substrate. This method provides gram scale production of graphene layers on any substrate via simple coating of dispersion, but exact control of layer thickness is not facile. Also, reduced GO still remains functional group, which limits electrical transport behavior. For instance, charge mobility of graphene obtained via reducing GO is between 0.1 and 10 cm<sup>2</sup>/V·sec.<sup>31</sup> These values are much greater than the GO's, but still a few orders of magnitude lower than these of pristine graphene.

### **1.2.2. Epitaxial growth (sublimation of SiC)**

Epitaxial growth of graphene refers sublimation of silicon carbide (SiC) single crystal substrate at higher than 1400 °C and ultra-high vacuum.<sup>29,30</sup> High temperature annealing grows graphene with a well-defined orientation and its

lattice fits well on a reconstructed interfacial layer on Si-face SiC. Graphene size is dependent upon the size of SiC wafer. The face of the SiC used for graphitization, silicon- or carbon-terminated, highly influences the thickness, mobility, and carrier density of the resulting graphene. Actually, high electron mobility was first visualized on top of SiC. Exfoliated graphene is usually produced by mechanical drawing method, which lies on top of SiO<sub>2</sub>, limits electron mobility compared to suspended graphene. However, even without transfer, graphene on SiC exhibits massless Dirac fermions and high charge carrier mobility which is result of weak anti-localization between SiC and graphene. The weak van der Waals force provides direct device fabrication of graphene on SiC, but the cost of single crystal SiC wafer is too expensive.

### **1.2.3. Chemical vapor deposition**

Chemical vapor deposition (CVD) uses hydrocarbon source such as CH<sub>4</sub>, C<sub>2</sub>H<sub>2</sub>, C<sub>2</sub>H<sub>4</sub>, etc.<sup>19-22</sup> Hydrocarbon source is injected on catalytic metal, and annealing provides carbon monomers by decomposition of hydrocarbon source. Carbon monomers migrate on the metal surfaces and form nuclei for graphene growth. Further growth proceeds by attaching carbon monomers and another nuclei can be grown by nuclei formation. CVD graphene can be grown on large scale which is limited to underlying metal foil size and graphene quality can be manipulated by tuning process parameters. Also, CVD enables low cost and transfer of the film is relatively simple using supporting polymer layer coating and followed removal via polymer dissolution using such as acetone.

	Reduction of graphene oxide	Sublimation of silicon carbide	Chemical vapor deposition
Scale	possible	wafer size	possible
Grain size of graphene	small	large	adjustable
Cost	cheap	expensive	cheap
Process temperature	room temperature	high	variable
Transfer simplicity	easy	hard	easy
Preparation of facility	simple	complicated	moderate

**Table 1-3.** Summary of advantages and drawbacks of each graphene growth method.

### **1.3. Understanding on graphene growth on Cu**

The present thesis addresses the synthesis of graphene by CVD on Cu, which has become the most popular catalyst for graphene growth. A significant study on the graphene growth kinetics and mechanisms is presented in this thesis for the introductory part of chapter 5 and 6.

#### **1.3.1. Graphene synthesis on Cu vs. Ni**

Graphene growth by CVD was first proposed using nickel substrate.<sup>40,41</sup> In this case, carbon atoms which generated by the dissociation of hydrocarbon molecules are dissolved in the Ni and they are precipitated out to form graphene layers at the surface during cooling due to the solubility difference of carbon at high temperature and room temperature. Faster cooling rate produces quenching of carbon atoms in Ni, while wide range of medium cooling rate provides larger precipitation of carbons at the surfaces. The mechanism of graphene growth on Ni and Cu was resolved by Li and coworkers.<sup>42,43</sup> They suggested that Cu has negligible carbon solubility in bulk and isothermal graphene growth process of Cu makes it possible for single layer graphene growth. Followed experimental results on isotope labeling technique using C<sup>12</sup> and C<sup>13</sup> precursor clearly showed that isothermal growth of graphene occurs at Cu surface as compared to surface precipitation growth mode in Ni. In their elaborate experiment, C<sup>12</sup> and C<sup>13</sup> doses were exposed as an alternative sequence for growth kinetics study, and micro-Raman mapping revealed growth front of each isotope. Graphene grown on Ni shows randomly mixed isotope C<sup>12</sup> and C<sup>13</sup> due to precipitation, but graphene grown on Cu shows time-dependent domain structures confirmed by Raman

mapping as shown in Figure 1-3.

### **1.3.2. Unique aspects of graphene growth on Cu**

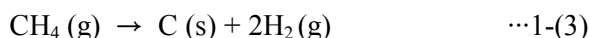
Graphene growth on Cu shows unique aspects contrary to conventional CVD system. The aspects are as follows;

(i) It needs metal catalyst in most cases of graphene growth. Dual role of metal is dissociating hydrocarbon source and crystallizing carbon monomers. Without catalytic metal such as Ni and Cu, hydrocarbon source decomposition temperature increases, and thermal decomposed carbon sources will not be able to crystallize and amorphous carbon will be deposited.<sup>44</sup> Several researchers have interested in direct thermal decomposition of hydrocarbon molecules in order to obtain hydrogen.<sup>45</sup> For instance, Abanades *et al.*, analyzed direct thermal cracking of methane molecules in a tube furnace at temperatures with relatively broad range.<sup>46</sup> Carbon black was deposited as a consequence of direct dissociation of methane molecules even at 1200 °C according to their experimental work. Thus, for lowering decomposition temperature of hydrocarbon source and crystallizing carbon phase, it is evident that metal catalyst is needed for high quality graphene growth.

(ii) Carbon monomers can only be decomposed on exposed Cu surface, which means that if the Cu surface is covered by graphene layers, carbon deposition does not occur in the assumption that multilayers are not formed. Thus, overall growth rate falls down with graphene layer covering exposed Cu surfaces. It shows similar behavior of Johnson-Mehl-Avrami (JMA) growth behavior which was already reported in graphene growth.<sup>47,48</sup> Growth rate decreases with increasing overall coverage, since growth rate is proportional to uncovered area. Also, total time for

fully covered graphene increases with smaller feeding rate and supersaturation ratio. As a consequence, graphene coverage as a function of time shows typical growth behavior of JMA as shown in Figure 1-4. This is two-dimensional crystallization kinetics of nucleation and growth.

Thermodynamically, overall reaction for graphene growth using methane source can be expressed simply;



According to the thermochemical data, Gibbs free energy of this equation 1-(3) is positive at room temperature. Since the reaction is endothermic, at higher growth temperature, overall free energy becomes negative. Thermochemical data of thermal decomposition process for typical hydrocarbon gas source are shown in Table 1-4. It is easily noticed that  $\text{CH}_4$  dissociation is the most unfavorable reaction to occur, which conversely means that nucleation rate can be minimized at the certain temperature for methane molecules. On the other hand, hydrocarbon sources with unsaturated carbon bonds or carbon di-, trimmers easily decompose at lower temperature. It also means that other hydrocarbon molecules provide larger number of carbon monomers at relatively low temperature. Thermochemical calculation of methane dissociation shows that free energy is positive at room temperature, but when temperature is higher than  $\sim 500$  °C, it becomes negative. It means that thermodynamically the reaction can occur at this temperature. However, the reaction temperature for graphene deposition is usually higher than 800 °C or even around 1000 °C. For the case of methane, the lowest temperature reported for graphene growth is about 720 °C. Systematic calculation on carbon source dissociation kinetics reveals that governing step for graphene growth is

dehydrogenation from  $\text{CH}_4$  to  $\text{CH}_3$  state. Without metal catalyst, thermal decomposition temperature for  $\text{CH}_4$  source is about  $1200\text{ }^\circ\text{C}$ , but with the help of catalytic activity, deposition can be done at below  $800\text{ }^\circ\text{C}$  according to the previous report.

### **1.3.3. Motivation for work: Transfer issue and polycrystalline nature**

In this thesis, two main issues are discussed. One is transfer process in graphene growth and followed device fabrication and the other is polycrystalline nature of graphene synthesis on catalytic metal. For the application of graphene, transfer to target substrate is essential. Target substrate is usually dielectric or polymer material for measurement of electrical transport of graphene. This transfer process is usually carried out by coating polymer material such as PDMS (polydimethylsiloxane) or PMMA (polymethylmethacrylate) and dissolving underlying catalytic metal. Floating PMMA/graphene layer is transferred to target substrate and residual PMMA is dissolved by acetone or organic solvent. Transfer process inevitably damages graphene layer and it would be desirable if we grow graphene layer on target substrate directly. Chapter 3 and 4 will cover direct graphene growth on target substrate.

The other one is polycrystalline nature of graphene growth. During the graphene growth on Cu surface, initial nuclei orientation is randomly distributed. Thus, as growth proceeds, different orientations of grains meet and grain boundaries are formed. This polycrystalline nature degrades the quality of graphene, and major issue for graphene growth is overcoming grain boundaries during polycrystalline graphene synthesis. In order to solve grain boundaries effect in graphene growth, two possible solutions can be suggested. First one is growing

grain size of graphene by suppressing nuclei density. The previous works on nucleation and growth study and empirical approaches are discussed in chapter 2. According to study of chapter 2, enlarging grain size by suppression initial nuclei density is possible by extreme feeding rate control, but growth rate inevitably decreased by low gas flow rate. The role of gas transport is discussed in chapter 5. Another approach for obtaining high-quality graphene is epitaxial growth which follow the same structure of underlying substrate. Generally, interaction between metal and graphene is weak, and the bonding is believed to be van der Waals nature, and epitaxy is hard to occur. Otherwise, self-assembly can be a solution for high-quality graphene growth. In chapter 6, Mesoepitaxy graphene growth is introduced. Graphene growth on liquid Cu shows unique behavior showing self-assembly of graphene islands. Even though grain size is not that large on liquid Cu, self-arrangement of each graphene island shows well aligned along the one axis, and grain boundaries will be much less in this self-assembly graphene film.

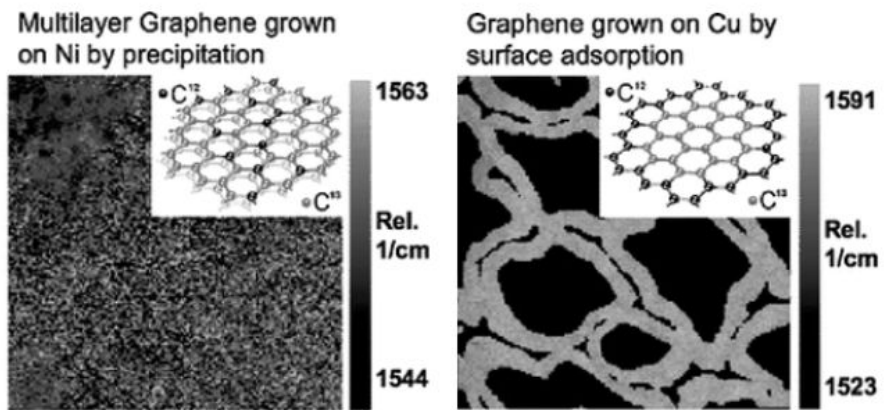


**Figure 1-3.**  $C^{12}$  and  $C^{13}$  isotope labeling experiment revealed by micro-Raman mapping on graphene grown on Ni and Cu. Graphene grown on Cu surface shows surface diffusion dominant growth and graphene grown on Ni shows randomly mixed carbon isotope due to precipitation of carbon atoms. (Adapted from [43])

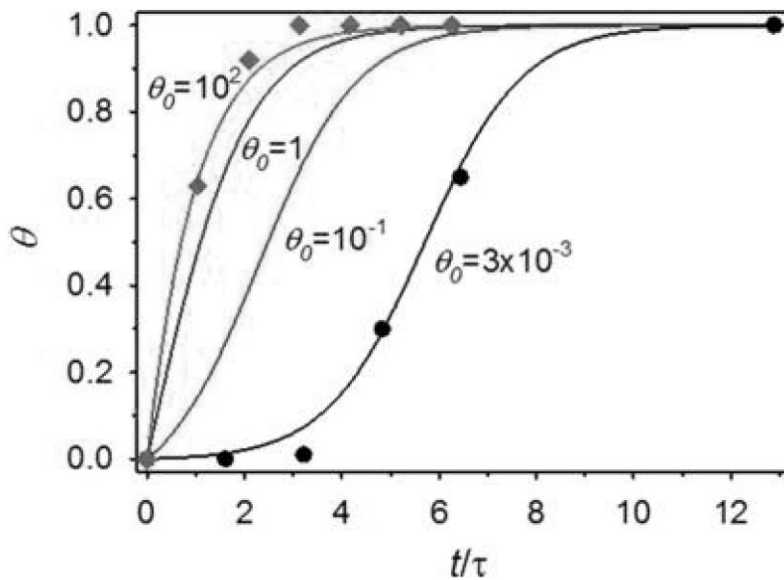


**Figure 1-4.** Growth curves calculated by G. Eres *et al.*, and coverage as a function of growth time measured by X. Li and G. Eres *et al.*, which correspond to typical JMA equation.  $\theta$  means coverage and  $t/\tau$  means normalized growth time. Graph adapted from [48]

CH <sub>4</sub> (g) → C (s) + 2H <sub>2</sub> (g) (methane)				C <sub>2</sub> H <sub>2</sub> (g) → 2C (s) + H <sub>2</sub> (g) (acetylene)				C <sub>2</sub> H <sub>4</sub> (g) → 2C (s) + 2H <sub>2</sub> (g) (ethylene)			
T (°C)	ΔH (kJ)	ΔS (J/K)	ΔG (kJ)	T (°C)	ΔH (kJ)	ΔS (J/K)	ΔG (kJ)	T (°C)	ΔH (kJ)	ΔS (J/K)	ΔG (kJ)
0	74.118	78.243	52.746	0	-226.774	-58.947	-210.672	0	-53.261	50.726	-67.117
100	77.144	87.686	44.424	100	-226.59	-58.373	-204.808	100	-50.175	60.377	-72.705
200	79.953	94.369	35.302	200	-226.371	-57.859	-198.995	200	-47.463	66.832	-79.085
300	82.451	99.168	25.612	300	-226.034	-57.216	-193.24	300	-45.089	71.394	-86.009
400	84.618	102.66	15.512	400	-225.57	-56.472	-187.555	400	-43.025	74.719	-93.323
500	86.453	105.208	5.112	500	-225.008	-55.696	-181.947	500	-41.257	77.174	-100.924
600	87.965	107.051	-5.506	600	-224.392	-54.946	-176.415	600	-39.775	78.98	-108.736
700	89.165	108.355	-16.28	700	-223.772	-54.274	-170.955	700	-38.573	80.286	-116.703
800	90.087	109.259	-27.164	800	-223.203	-53.717	-165.557	800	-37.646	81.194	-124.78
900	90.72	109.824	-38.121	900	-222.641	-53.216	-160.21	900	-36.89	81.868	-132.934
1000	91.112	110.147	-49.121	1000	-222.099	-52.773	-154.911	1000	-36.287	82.363	-141.147
C <sub>2</sub> H <sub>6</sub> (g) → 2C (s) + 3H <sub>2</sub> (g) (ethane)				C <sub>3</sub> H <sub>8</sub> (g) → 3C (s) + 4H <sub>2</sub> (g) (propane)				C <sub>4</sub> H <sub>10</sub> (g) → 4C (s) + 5H <sub>2</sub> (g) (n-butane)			
T (°C)	ΔH (kJ)	ΔS (J/K)	ΔG (kJ)	T (°C)	ΔH (kJ)	ΔS (J/K)	ΔG (kJ)	T (°C)	ΔH (kJ)	ΔS (J/K)	ΔG (kJ)
0	83.405	169.435	37.124	0	102.154	263.987	30.046	0	146.713	442.637	25.806
100	88.336	184.867	19.353	100	108.582	284.128	2.56	100	150.6	454.644	-19.05
200	92.571	194.954	0.329	200	113.911	296.825	-26.532	200	155.726	466.759	-65.121
300	96.189	201.908	-19.535	300	118.351	305.364	-56.668	300	161.935	478.634	-112.394
400	99.246	206.837	-39.986	400	122.025	311.288	-87.518	400	169.104	490.143	-160.836
500	101.777	210.351	-60.855	500	124.994	315.41	-118.866	500	177.098	501.203	-210.407
600	103.806	212.824	-82.021	600	127.294	318.217	-150.557	600	185.778	511.753	-261.06
700	105.351	214.504	-103.394	700	128.952	320.021	-182.476	700	195.005	521.753	-312.74
800	106.428	215.561	-124.901	800	129.986	321.037	-214.535	800	204.637	531.173	-365.391
900	107.153	216.209	-146.492	900	130.564	321.554	-246.667	900	214.737	540.167	-418.96
1000	107.585	216.564	-168.133	1000	130.764	321.719	-278.833	1000	225.249	548.765	-473.41

**Table 1-4.** Thermochemical data (enthalpy, entropy and Gibbs free energy) of thermal decomposition reactions for typical hydrocarbon source used for graphene growth.

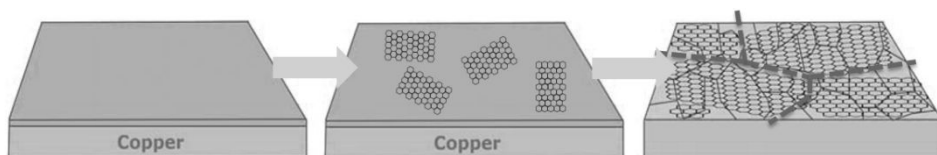


**Figure 1-5.** Schematic illustration of graphene growth on catalytic Cu surfaces showing random orientation of nuclei formation. Further growth results in polycrystalline film. Figure adapted from [49]

## References

1. P. R. Wallace, *Physical Review* **71**, 622 (1947)
2. P. Avouris, Z. Chen, V. Perebeinos, *Nat. Nanotechnol.* **2**, 605 (2007)
3. K. S. Novoselov, A. K. Geim, S. V. Morozov, D. Jiang, Y. Zhang, S. V. Dubonos, I. V. Grigorieva, A. A. Firsov, *Science* **306**, 666 (2004)
4. K. S. Novoselov, D. Jiang, F. Schedin, T. J. Booth, V. V. Khotkevich, S. V. Morozov, A. K. Geim, *Proc. Nat. Acad. Sci.* **102**, 10451 (2005)
5. K. S. Novoselov, A. K. Geim, S. V. Morozov, D. Jiang, M. I. Katsnelson, I. V. Grigorieva, S. V. Dubonos and A. A. Firsov, *Nature* **438** (7065), 197-200 (2005)
6. K. I. Bolotin, K. J. Sikes, Z. Jiang, M. Klima, G. Fudenberg, J. Hone, P. Kim and H. L. Stormer, *Solid State Commun.* **146** (9–10), 351-355 (2008).
7. K. S. Novoselov, Z. Jiang, Y. Zhang, S. V. Morozov, H. L. Stormer, U. Zeitler, J. C. Maan, G. S. Boebinger, P. Kim and A. K. Geim, *Science* **315** (5817), 1379-1379 (2007).
8. B. Ozyilmaz, P. Jarillo-Herrero, D. Efetov and P. Kim, *Appl. Phys. Lett.* **91** (19), - (2007).
9. H. W. Kroto, J. R. Heath, S. C. O'Brien, R. F. Curl and R. E. Smalley, *Nature* **318** (6042), 162-163 (1985).
10. S. Iijima, *J. Cryst. Growth* **50** (3), 675-683 (1980).
11. S. Roddaro, P. Pingue, V. Piazza, V. Pellegrini and F. Beltram, *Nano Letters* **7** (9), 2707-2710 (2007).
12. D. S. L. Abergel, A. Russell and V. I. Fal'ko, *Appl. Phys. Lett.* **91** (6), 063125 (2007).
13. A. K. Geim and K. S. Novoselov, *Nat. Mater.* **6** (3), 183-191 (2007).

14. N. M. R. Peres and M. R. Ricardo, *New Journal of Physics* **11** (9), 095002 (2009).
15. Y.-M. Lin, C. Dimitrakopoulos, K. A. Jenkins, D. B. Farmer, H.-Y. Chiu, A. Grill and P. Avouris, *Science* **327** (5966), 662 (2010).
16. L. Liao, J. W. Bai, R. Cheng, Y. C. Lin, S. Jiang, Y. Q. Qu, Y. Huang and X. F. Duan, *Nano Letters* **10** (10), 3952-3956 (2010).
17. A. T. T. Koh, Y. M. Foong, L. Pan, Z. Sun and D. H. C. Chua, *Appl. Phys. Lett.* **101** (18), 183107 (2012).
18. Y.-M. Lin, A. Valdes-Garcia, S.-J. Han, D. B. Farmer, I. Meric, Y. Sun, Y. Wu, C. Dimitrakopoulos, A. Grill, P. Avouris and K. A. Jenkins, *Science* **332** (6035), 1294-1297 (2011).
19. K. S. Kim, Y. Zhao, H. Jang, S. Y. Lee, J. M. Kim, K. S. Kim, J.-H. Ahn, P. Kim, J.-Y. Choi and B. H. Hong, *Nature* **457** (7230), 706-710 (2009).
20. X. Li, Y. Zhu, W. Cai, M. Borysiak, B. Han, D. Chen, R. D. Piner, L. Colombo and R. S. Ruoff, *Nano Letters* **9** (12), 4359-4363 (2009).
21. S. Bae, H. Kim, Y. Lee, X. Xu, J.-S. Park, Y. Zheng, J. Balakrishnan, T. Lei, H. Ri Kim, Y. I. Song, Y.-J. Kim, K. S. Kim, B. Ozyilmaz, J.-H. Ahn, B. H. Hong and S. Iijima, *Nat Nano* **5** (8), 574-578 (2010).
22. Y. Lee, S. Bae, H. Jang, S. Jang, S. E. Zhu, S. H. Sim, Y. I. Song, B. H. Hong and J. H. Ahn, *Nano Lett* **10** (2), 490-493 (2010).
23. S. Garaj, W. Hubbard, A. Reina, J. Kong, D. Branton and J. A. Golovchenko, *Nature* **467** (7312), 190-193 (2010).
24. J.-H. Chen, C. Jang, S. Xiao, M. Ishigami and M. S. Fuhrer, *Nat Nano* **3** (4), 206-209 (2008).
25. C. R. Dean, A. F. Young, MericI, LeeC, WangL, SorgenfreiS, WatanabeK,

- Taniguchi T, Kim P, K. L. Shepard and Hone J, *Nat Nano* **5** (10), 722-726 (2010).
26. A. S. Mayorov, R. V. Gorbachev, S. V. Morozov, L. Britnell, R. Jalil, L. A. Ponomarenko, P. Blake, K. S. Novoselov, K. Watanabe, T. Taniguchi and A. K. Geim, *Nano Letters* **11** (6), 2396-2399 (2011).
27. A. K. Geim, *Science* **324** (5934), 1530-1534 (2009).
28. Q. Yu, L. A. Jauregui, W. Wu, R. Colby, J. Tian, Z. Su, H. Cao, Z. Liu, D. Pandey, D. Wei, T. F. Chung, P. Peng, N. P. Guisinger, E. A. Stach, J. Bao, S.-S. Pei and Y. P. Chen, *Nat Mater* **10** (6), 443-449 (2011).
29. C. Berger, Z. M. Song, X. B. Li, X. S. Wu, N. Brown, C. Naud, D. Mayo, T. B. Li, J. Hass, A. N. Marchenkov, E. H. Conrad, P. N. First and W. A. de Heer, *Science* **312** (5777), 1191-1196 (2006).
30. K. V. Emtsev, A. Bostwick, K. Horn, J. Jobst, G. L. Kellogg, L. Ley, J. L. McChesney, T. Ohta, S. A. Reshanov, J. Rohrl, E. Rotenberg, A. K. Schmid, D. Waldmann, H. B. Weber and T. Seyller, *Nat Mater* **8** (3), 203-207 (2009).
31. T. Kobayashi, N. Kimura, J. Chi, S. Hirata and D. Hobara, *Small* **6** (11), 1210-1215 (2010).
32. R. R. Nair, P. Blake, A. N. Grigorenko, K. S. Novoselov, T. J. Booth, T. Stauber, N. M. Peres and A. K. Geim, *Science* **320** (5881), 1308 (2008).
33. L. B. Gao, W. C. Ren, F. Li and H. M. Cheng, *Acs Nano* **2** (8), 1625-1633 (2008).
34. Z. H. Ni, H. M. Wang, J. Kasim, H. M. Fan, T. Yu, Y. H. Wu, Y. P. Feng and Z. X. Shen, *Nano Letters* **7** (9), 2758-2763 (2007).
35. D. S. L. Abergel, A. Russell and V. I. Fal'ko, *Appl. Phys. Lett.* **91** (6), 063125 (2007).
36. C. Lee, X. Wei, J. W. Kysar and J. Hone, *Science* **321** (5887), 385-388 (2008).

37. S. Chen, L. Brown, M. Levendorf, W. Cai, S.-Y. Ju, J. Edgeworth, X. Li, C. W. Magnuson, A. Velamakanni, R. D. Piner, J. Kang, J. Park and R. S. Ruoff, *ACS Nano* **5** (2), 1321-1327 (2011).
38. M. D. Stoller, S. Park, Y. Zhu, J. An and R. S. Ruoff, *Nano Letters* **8** (10), 3498-3502 (2008).
39. S. Park and R. S. Ruoff, *Nat Nano* **4** (4), 217-224 (2009).
40. Q. K. Yu, J. Lian, S. Siriponglert, H. Li, Y. P. Chen and S. S. Pei, *Appl. Phys. Lett.* **93** (11), 113103 (2008).
41. S. J. Chae, F. Güneş, K. K. Kim, E. S. Kim, G. H. Han, S. M. Kim, H.-J. Shin, S.-M. Yoon, J.-Y. Choi, M. H. Park, C. W. Yang, D. Pribat and Y. H. Lee, *Adv. Mater.* **21** (22), 2328-2333 (2009).
42. X. S. Li, W. W. Cai, J. H. An, S. Kim, J. Nah, D. X. Yang, R. Piner, A. Velamakanni, I. Jung, E. Tutuc, S. K. Banerjee, L. Colombo and R. S. Ruoff, *Science* **324** (5932), 1312-1314 (2009).
43. X. Li, W. Cai, L. Colombo and R. S. Ruoff, *Nano Letters* **9** (12), 4268-4272 (2009).
44. H. Hussin, F. Mohamad, S. M. A. Hanapiah, M. Muhamad, M. Rusop, *Electronic Devices, Systems and Applications (ICEDSA)*, Intl Conf on; 11-14 April 2010.
45. H. F. Abbas, W. M. A. Wan Daud, A review. *Int J Hydrogen Energy*. **35**(3), 1160-90 (2010)
46. A. Abánades, E. Ruiz, E. M. Ferruelo, F. Hernández, A. Cabanillas, J. M. Martínez-Val et al., *Int J Hydrogen Energy* **36**(20), 12877-86 (2011)
47. H. Kim, C. Mattevi, M. R. Calvo, J. C. Oberg, L. Artiglia, S. Agnoli et al., *ACS Nano*. **6**(4), 3614-23 (2012)

48. G. Eres, M. Regmi, C. M. Rouleau, J. Chen, I. N. Ivanov, A. A. Poretzky et al., ACS Nano. (2014)
49. C. Mattevi, H. Kim and M. Chhowalla, J. Mater. Chem. **21** (10), 3324-3334 (2011).



## CHAPTER 2.

### **Review on graphene growth on Cu**



## 2.1. Introduction

Literature survey on previous works on graphene growth needs to be investigated. In order to overcome polycrystalline nature and to obtain high-quality graphene, fundamental understanding is needed in terms of thermodynamics and kinetics approach. Not only basic theories for graphene growth in a view of materials science, but also practical approaches in the previous literature for high-quality graphene growth should be covered. In this chapter, empirical parameter control and pioneering work in graphene growth will be discussed.

Generally, for the growth of graphene, hydrocarbon sources are injected at growth temperature. Carbon gas source decomposes at the catalytic Cu surface and carbon monomers are supplied. Carbon monomers migrate on the Cu surfaces, and nuclei forms when cluster size reaches critical level. Surface diffusion of carbon monomers can enlarge pre-existing nuclei and also forms new nuclei which is the result of random nucleation and growth. Graphene growth step can be understood as;

- (1) Gas phase delivery of hydrocarbon molecules
- (2) Dehydrogenation of  $C_xH_y$  molecules (thermal decomposition)
- (3) Adsorption of carbon molecules on Cu surface and adatom migration
- (4) Formation of critical nuclei (carbon clustering)
- (5) Adatom surface migration and attach to carbon cluster

All the above steps are combined and occur simultaneously. Step (4) and (5) result in random nucleation and growth.

## 2.2. Observation of growth kinetics

In order to analyze the quality of graphene, which is grain size of graphene, observation of graphene growth is required. Growth kinetics studies including average grain growth rate, nuclei density, and morphological changes are main topic in graphene growth. The simplest observation method<sup>1</sup> is stopping graphene growth before the final coverage and searching partially grown graphene islands as shown in Figure 2-1. Recently, direct optical visualization method was suggested by several groups.<sup>1-3</sup> By selective oxidation of Cu which is not covered by graphene, graphene islands can be distinguishable by optical microscope and even by naked eyes when the islands sizes are significantly large. Raman spectroscopy did a great role in developing graphene research due to its non-destructive and layer-resolved analysis.<sup>4-6</sup> Graphene quality can be investigated by Raman spectrum and mapping, but Raman spectroscopy is not quantitative analysis tool for observing grain size of graphene and measuring graphene quality.

Detailed local atomic arrangement of graphene lattices can be studied by *ex-situ* scanning electron microscopy (SEM), low energy electron diffraction and microscopy (LEED and LEEM),<sup>7,8</sup> transmission electron microscopy (TEM)<sup>9-12</sup> and scanning tunneling microscopy (STM)<sup>13-15</sup> analysis. At a certain growth time, samples were prepared without transfer and observed by SEM on Cu substrate. Grain shape, density, size and distribution can be analyzed as a function of growth time. Wofford *et al.*, studied polycrystalline nature of graphene islands grown on

Cu foil by LEED analysis.<sup>7</sup> To avoid Cu evaporation at high temperature, carbon was evaporated instead of thermal decomposition of methane source and supplied to Cu substrate at temperature lower than 1000 °C. Four-lobed graphene islands shape were the same as the graphene grown by CVD method, and they found out that the graphene islands were no single crystals and consist of domains with 4 different orientations. They also insisted that step and terrace on Cu act as nucleation sites for graphene growth indicating that the surface condition of Cu is quite an important factor. Moreover, Huang *et al.*, at Cornell University used STEM (Scanning TEM) high-angle annular dark field (HAADF) image for grain boundaries observation.<sup>10</sup> They revealed that grain boundary structure consists of carbon heptagon and pentagon buckling as confirmed by Figure 2-2, which was suggested few decades ago by theoretical calculations.<sup>16,17</sup> Dark field (DF) mapping clearly showed various grain orientations of as-grown continuous graphene film which is the result of polycrystalline nature due to random nucleation. They grew various graphene film by several recipes and compared films from each recipe and obtained different electrical properties from them. This clearly emphasizes the fact that graphene growth should be understood and well controlled. Kim *et al.*, also used grain boundaries (GBs) mapping based on diffraction pattern in STEM for grain orientation analysis. Statistical data of grain boundaries orientation they obtained showed similar results from polycrystalline growth nature.<sup>18</sup>

A. W. Tsen *et al.*, not only observed GBs structure and carried out DF mapping, but measured electrical transport behavior of graphene film from various recipes.<sup>19</sup> They insisted importance of grain boundaries shape rather than just grain size, which means that not only grain size, but the inter-domain connection should be considered. Smaller domain sized graphene with well stitched each other would be

better in transport than large domain sized graphene with poor stitching according to their report. Also, electrical transport measurement carried out by Q. Yu *et al.*,<sup>20</sup> revealed that electrical properties of device from intra-grain shows better performance than that from inter-grain as shown in Figure 2-3. Effective inter-grain resistivity was always higher than intra-grain resistivity according to their results, and also low temperature Hall measurement showed that inter-grain mobility was lower than intra-grain mobility indicating that grain boundaries are impeding electrical transport and avoiding grain boundaries are substantially beneficial.

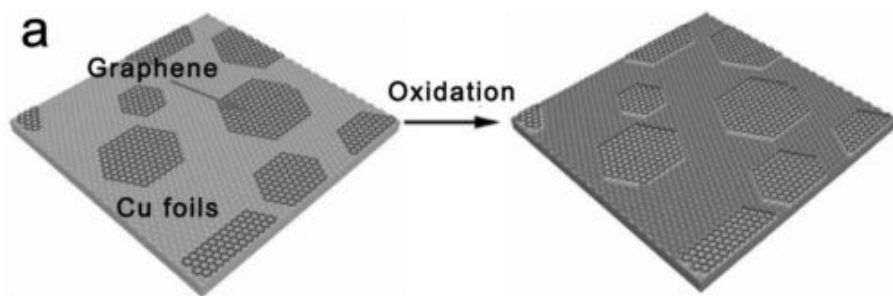


**Figure 2-1.** Schematic illustration for direct optical visualization of graphene islands on Cu substrate by oxidizing Cu surfaces which is not covered by graphene. Figure adapted from [1]

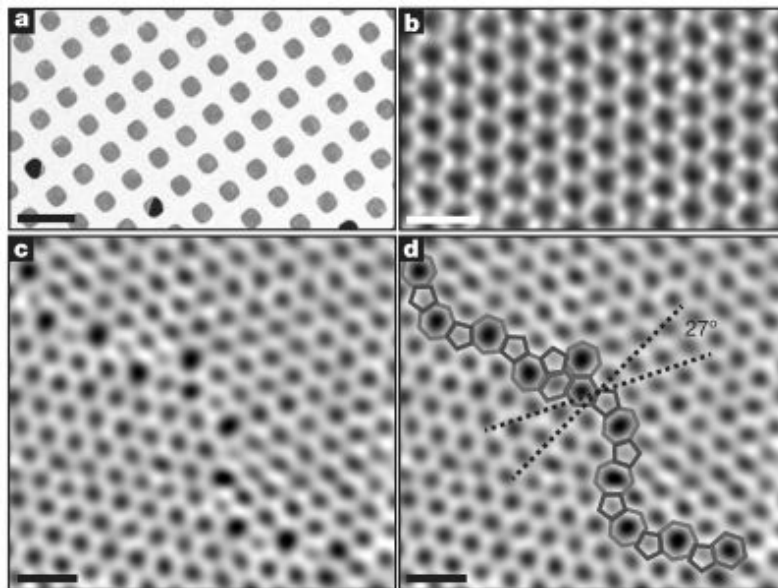


**Figure 2-2.** Atomic-resolution ADF (annular dark field)-STEM images of graphene domain boundaries observed by P. Y. Huang *et al.*,<sup>11</sup> (a) Low magnification image showing TEM grid opening, (b) perfect graphene lattice, (c) atomic resolution image of graphene grain boundary and (d) atomic structure of grain boundary is drawn on (c).

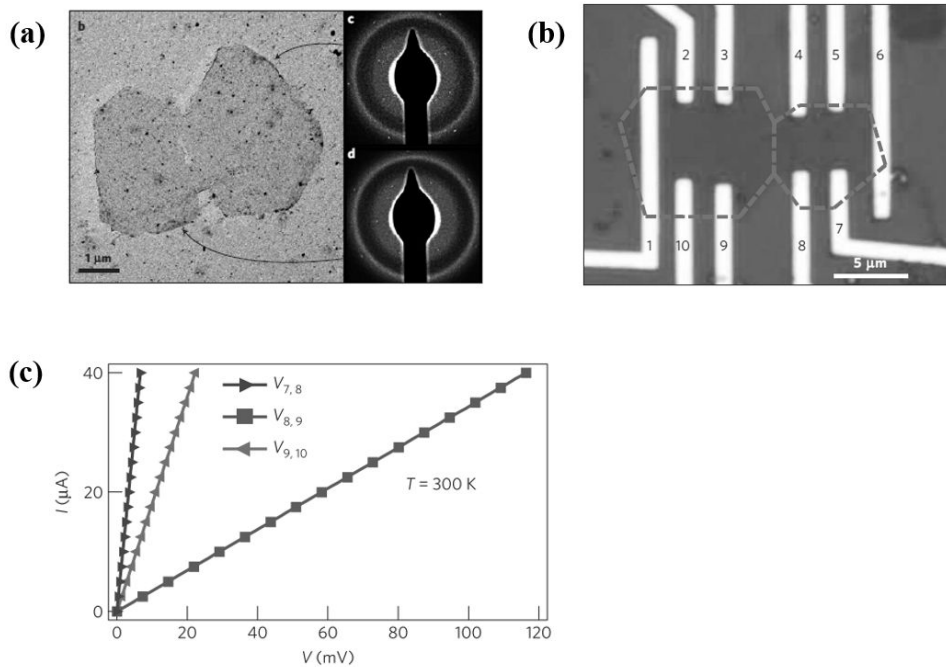


**Figure 2-3.** (a) Bright field TEM image of two graphene grains showing different orientations of diffraction pattern, (b) metal electrodes on individual graphene grains touching each other, and (c) resistance of intra (7,8), (9,10) and inter- (8,9) graphene grains. Figures adapted from [19]

### 2.3. Surface treatment of Cu

Although many researches have been done for understanding thermodynamic and kinetic behaviors of graphene growth, the Cu foils which we use for substrate in graphene growth are not ideal. Rolling feature, scratches, and many impurities formed during manufacturing process result in defect site for graphene growth. Various foils which provided by supplier show different surface RMS (root mean square) roughness as shown in Figure 2-4 by atomic force microscopy (AFM) measurement. Thus, overcoming heteronucleation due to surface roughness and impurities is one of the main concern when we grow graphene on Cu. Pre-anneal gives smoothing effect to certain level, but we cannot consider Cu foil as perfect substrate for graphene growth even after pre-anneal. Surface state and removing heteronucleation have been the most important issue in graphene growth practically since introduction of graphene CVD. According to classical theory for nucleation and growth, the number of stable nuclei can be expressed as equation 2-(1).

$$n^* = n_0 \exp\left(-\frac{\Delta G^*}{kT}\right) \quad \dots 2-(1)$$

Here,  $n^*$  denotes number of stable nuclei,  $\Delta G^*$  means activation barrier for nucleation,  $k$  is Boltzmann constant, and  $T$  is temperature. However, the  $n_0$  we consider as constant is not actually variable if our Cu substrate is not ideal. When terraces, ledges, and other topological defects such as scratches exist in the Cu,  $n_0$  cannot be fixed and nucleation rate is totally different. Several groups have tried to resolve surface defects problem. Luo *et al.*, used electropolishing (EP) for smoothing Cu surface.<sup>20</sup> Cu foil was immersed in acid solution with solvent mixed and current was applied for etching its surface. AFM surface roughness

measurement shows smoother Cu surface after EP process compared to as-purchased one. And, they claimed that step edges and surface textures such as valleys on Cu can be reactive site and act as nucleation sites. Many works have adopted EP process and reported similar results on the role of surface imperfections.<sup>21-24</sup> Also, it was reported that little etching of Cu surface by  $\text{CH}_3\text{COOH}$ ,<sup>25</sup>  $\text{HCl}$  and  $\text{FeCl}_3$ <sup>26</sup> can show the suppression of nuclei due to removing of surface impurities. Sometimes, ultra-sonication is used for organic impurities removal before the growth. Chemical mechanical planarization (CMP) can also be used for polishing Cu surface.<sup>27</sup> Han *et al.*, showed that graphene seeds grew along the polishing line of Cu surface which was formed during cold rolling process of Cu foil manufacturing. CMP process clearly decreased polishing damage which did not disappear by just heating. Density of graphene nucleation seeds was much lower on CMP treated Cu foil. However, residual CMP slurry particles should be removed which may result in another heteronuclei effect. Suppressing heteronucleation in graphene growth is critical issue in terms of defect control and enlarging graphene grain size.

Several technical breakthrough were reported in order to suppress heteronuclei effect and large single crystal graphene grains were achieved. For instance, Wang *et al.*, proposed high temperature (1045 °C) annealing for 3 hours before graphene growth at APCVD without surface treatment such as CMP and EP process.<sup>2</sup> They revealed that nuclei density can be highly reduced by prolonging pre-annealing time and grain size was enlarged up to 500  $\mu\text{m}$ . Their submillimeter-sized graphene was optically visible after oxidizing Cu surface due to selective oxidation of graphene-covered and uncovered region. Yan *et al.*, also applied high temperature annealing for smoothing Cu surface.<sup>24</sup> They systematically showed the results of

each surface treatment process step by step and followed graphene growth behavior including EP and high temperature annealing as shown in Figure 2-5. (Also, decreasing carbon flux and increasing temperature growth) Cu foil was annealed at 1070 °C and 1500 Torr for longer than 7 hours for suppression of heteronucleation. This extended annealing at high temperature was possible due to high pressure induced suppression of Cu sublimation. 2.3 mm sized graphene domains were achieved via reducing active sites and followed extremely decreased nuclei density.

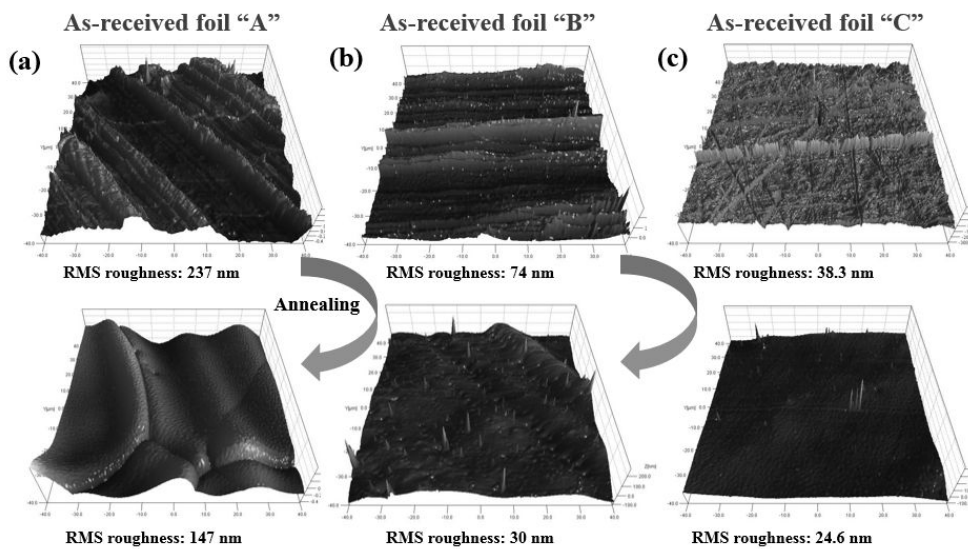


**Figure 2-4.** AFM RMS (root-mean square) surface roughness measurement of various Cu foil before and after annealing. Foil A is 25  $\mu\text{m}$ -thick and purity of Cu is 99.8 % from Alfa Aesar (product #: 13382, unpolished), foil B is 25  $\mu\text{m}$ -thick and purity of Cu is 99,999 % from Alfa Aesar (product #: 10950, unpolished), and foil C is 50  $\mu\text{m}$ -thick and purity of Cu is 99.999 % from Alfa Aesar. Annealing temperature is 1050  $^{\circ}\text{C}$  at atmospheric pressure ( $\text{Ar}+\text{H}_2$ ).

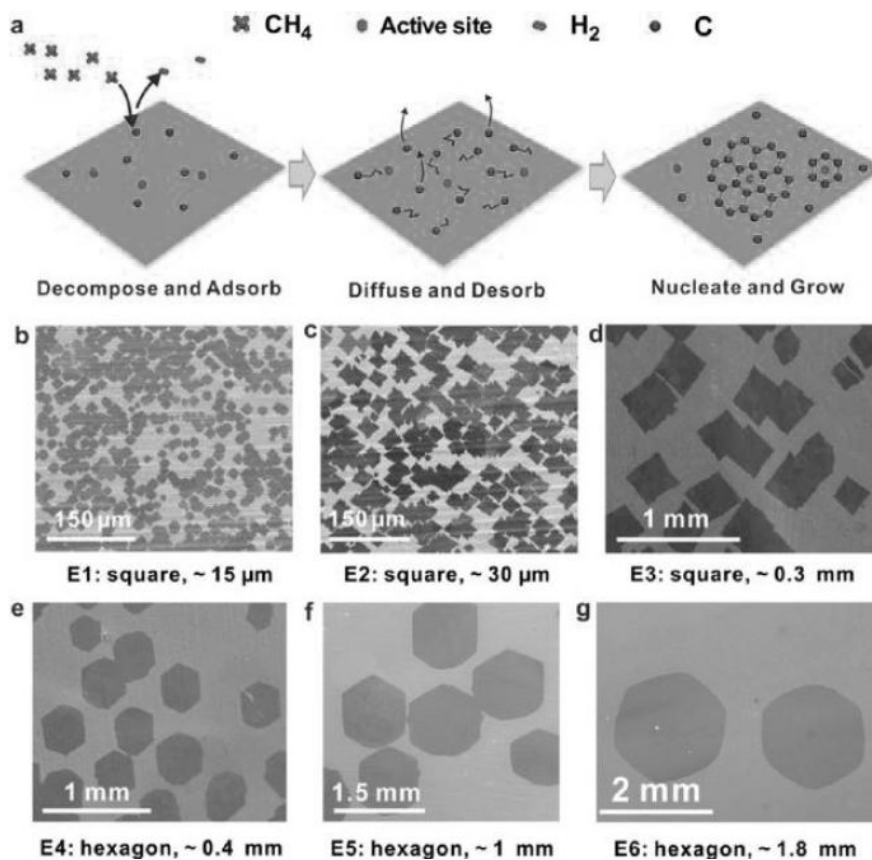


**Figure 2-5.** (a) Schematic illustration of graphene growth on active site of Cu surface and (b) to (g) systematic control of surface treatment and growth parameters in CVD graphene growth and typical graphene domain sizes from each recipe reported by Z. Yan *et al.*,<sup>24</sup> E1 denotes typical graphene growth at 1060 °C, E2 denotes decreased CH<sub>4</sub> flux, E3 denotes high pressure annealing and electropolished, E4 denotes increased growth pressure, E5 denotes increased growth temperature and E6 denotes further increased growth temperature.

## 2.4. Effect of growth temperature

We always should consider two factors when considering graphene nuclei density (inversely, grain size), which are dissociation of hydrocarbon source and surface diffusion of dissociated carbon monomers. At higher temperature, two possible growth behaviors compete. Due to larger amount of carbon monomers given by hydrocarbon dissociation, nuclei formation is favored. This influences higher growth rate and degrades film quality in general CVD mode.

However, according to the many results, larger graphene grain sizes can be achieved at higher temperature.<sup>1,28-30</sup> Rather, it indicates that graphene growth is not nucleation limited process, but growth limited process. Grain size of graphene are larger at higher growth temperature. Namely, the nucleation rate does not change that much with the temperature increase. Surface diffusion length which is expressed by equation 2-(2)

$$X = \sqrt{2D_s \tau_s} \quad \dots 2-(2)$$

where  $D_s$  is diffusion coefficient of carbon monomers at the surface and  $\tau_s$  is residence time of monomer. Thus, increased surface diffusion length at high temperature governs the graphene quality compared to nuclei density dependence. Of course, high temperature annealing also smoothen Cu surface also. This makes researchers favors high temperature graphene growth. For instance, Kim *et al.*, did systematical works on temperature dependence of graphene growth.<sup>31</sup> They considered graphene growth as the crystallization of supersaturated fraction of carbon species and competition between adatom capture and surface diffusion

procedure. They divided two regimes for graphene growth in terms of temperature in order to calculate saturated nuclei density which is also related to grain size, one is carbon adatom species capture controlled regime at low temperature and the other is desorption controlled regime at high temperature. In both cases, high temperature is favored for low nuclei density. The increase in capture probability of a supercritical nucleus relative to the nucleation rate can be explained by increase of carbon adatom mobility or desorption rate of unstable carbon species at high temperature.

Temperature dependent graphene growth was also studied by other groups and similar results were reported.<sup>21,28</sup> Hwang *et al.*, studied initial stage of graphene growth, and measured nuclei density varying temperature and H<sub>2</sub>/CH<sub>4</sub>. Their logarithmic plot of graphene nuclei density shows temperature dependence similar to that of Kim's work. Vlasiouk *et al.*, also measured nuclei density as a function of growth temperature for the case of LPCVD and APCVD. They extracted activation energy from the plot of nuclei density vs. 1/T and the value was different at LP and APCVD cases.

## 2.5. Source gas feeding rate

Carbon source feeding rate can be controlled easily during the CVD step by the gas flow. Smaller feeding rate provides larger graphene grain size by decreasing nuclei density. Many experimental works have reported that smaller methane flow forms larger graphene island growth.<sup>1,24,29,32,33</sup> Smaller hydrocarbon feeding source provides small degree of carbon supersaturation and nuclei formation is suppressed according to classical nucleation theory.<sup>34</sup> However, small supersaturation ratio also decreases growth rate because of small carbon flux and gap fill exists between graphene grains without stitching. Li *et al.*, adopted two-step graphene growth method, which uses small feeding rate at the initial stage (see Figure 2-6) and increase of feeding rate at later stage to fill the gap between graphene grains.<sup>29</sup> Not only Li *et al.*, but A. W. Tsen also reported that when carbon source feeding rate is too small, obtaining fully covered graphene film is not possible due to low supersaturation ratio.<sup>19,29</sup> On the other hand, higher CH<sub>4</sub> flow rate leads to shorter time to reach critical nuclei formation and faster film growth.<sup>35</sup> Since graphene growth can be carried out at both low pressure and atmospheric pressure, pressure and carbon feeding rate window are quite wide, thus self-limiting graphene growth cannot be applied at wide range. Sun *et al.*, used very wide window for partial pressure of methane for graphene growth, they obtained multilayered graphene including bi-, tri-, and tetra-layers and this fact shows that graphene growth on Cu is not always self-limited to single layer formation.<sup>36,37</sup> Manipulation of hydrocarbon source is related to CH<sub>4</sub>/H<sub>2</sub> feeding ratio and total pressure of chamber also, it is hard to figure out which factor is governing the graphene growth.

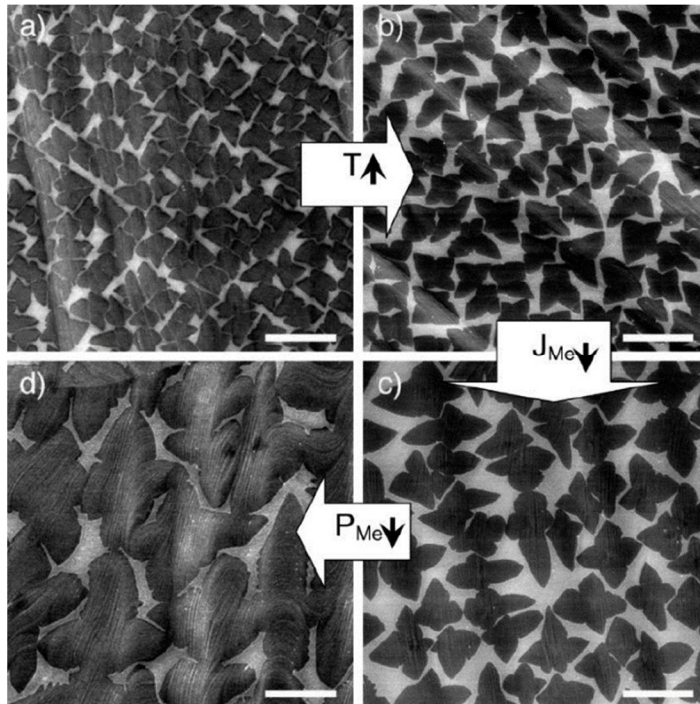


**Figure 2-6.** SEM images of partially grown graphene under different growth conditions: T (°C)/J<sub>CH<sub>4</sub></sub> (sccm)/P<sub>CH<sub>4</sub></sub> (mTorr): (a) 985/35/460, (b) 1035/35/460, (c) 1035/7/460, (d) 1035/7/160, Scale bars indicate 10 μm. Figures adapted from [29]

## 2.6. Morphology evolution and hydrogen etching

One of the notable things in graphene growth is the morphology evolution of graphene domains. Graphene shows various morphologies from dendritic to polygon shape as a result of various growth conditions. Usually, LPCVD growth gives usually dendritic shape,<sup>22,29,33,38,39</sup> but APCVD shows polygon shape with no flowerlike edges.<sup>20,24,35,39,40</sup> High working pressure of APCVD enables high H<sub>2</sub>/CH<sub>4</sub> flow rate ratio (>100) and compact hexagon shape was frequently observed due to H<sub>2</sub> induced etching effect. Since gas flow is stationary and CH<sub>4</sub> gas can be build up without vacuum pump, multilayered graphene can be formed with low concentration of H<sub>2</sub> and high flow rate of CH<sub>4</sub> in APCVD.<sup>35</sup> Contrary to APCVD, H<sub>2</sub>/CH<sub>4</sub> flow rate ratio is low in LPCVD and supersaturation ratio for nuclei formation is hard to obtain at high H<sub>2</sub> flow.

Morphology difference also can be attributed to high desorption carbon desorption rate at low pressure and diffusion-limited growth mode. Vlassioug *et al.*, compared LP and APCVD systematically.<sup>21</sup> In their study, different activation energies and followed nuclei density were measured for each case. They claimed that growth morphology difference between LP and APCVD is due to higher sublimation rate of carbon monomers in LPCVD growth, resulting high desorption rate. Fan *et al.*, investigated morphological evolution of graphene based on APCVD and revealed that underlying Cu substrate orientation is related to lobe shape.<sup>41</sup> Theoretical calculation study by E. Meca *et al.*, support the idea that morphological evolution is derived from gas pressure difference.<sup>42</sup> Hexagon shape graphene usually obtained by APCVD is due to relative stability of zigzag edge

compared to armchair edge.<sup>43,44</sup> Thus, at the static gas environment in APCVD, surface reaction-limited growth favors zigzag edge of graphene with the help of hydrogen etching.

Graphene domain morphology is a result of competition between surface diffusion of carbon monomer and edge-migration of attached monomers. According to the work by B. Wu *et al.*,<sup>45</sup> graphene growth morphology can be delicately controlled from dendritic to compact hexagon and even to circular shape as shown in Figure 2-7. This elaborate control was possible since graphene growth on liquid Cu shows unique behavior with grain boundary-free and heteronuclei effect reduced nature. At given concentration of CH<sub>4</sub>, low H<sub>2</sub>/Ar flow rate gives highly fractal-like growth front, but further increase of H<sub>2</sub> etches dendrite, and finally obtained compact hexagon. Also, they manipulated CH<sub>4</sub> rate and observed circular grain morphology.

When carbon monomer supply rate to the graphene domain is slow, carbon monomers can rearrange at the edges of graphene domain. However, as carbon monomer flux increases, dendritic shape appears as a result of interface instability. This result means that carbon atoms do not have enough time for rearrange at the edges of graphene lattices due to overflux. We summarized domain shape obtained from literature as a function of grain growth rate and it is well matched as shown in Table 2-1. Faster grain growth rate (calculated simply from SEM images in the report) shows dendritic shape, but all the slow grain growth rate shows typical hexagon. Some of the hexagon shape occurs despite of fast grain growth, which is thought as a consequence of surface treatment causing surface diffusion enhancement via smoothing Cu surface.

It has been already known that hydrogen (H<sub>2</sub>) etches graphene lattice such as

hydrogenated atomic edges. Actually, hydrogen etch of graphene is reverse of its growth step.



Vlassioug *et al.*,<sup>46</sup> systematically studied the role of hydrogen in graphene growth. Increasing hydrogen partial pressure changes dendritic graphene islands to polygons shape which they explained edges of graphene can be etched by hydrogen. Not only variation of hydrogen partial pressure during growth, but post-annealing of as-grown graphene also shows etching behavior. Thus, hydrogen etching can explain polygon shape usually obtained in APCVD which adopt relatively high partial pressure of hydrogen. Zhang *et al.*,<sup>47</sup> also showed hydrogen induced etching during graphene growth by CVD. They showed similar anisotropic etching behavior of graphene on Cu by hydrogen. Although their graphene was continuous before etching experiment, hexagonal openings were formed during etching process and propagated further.

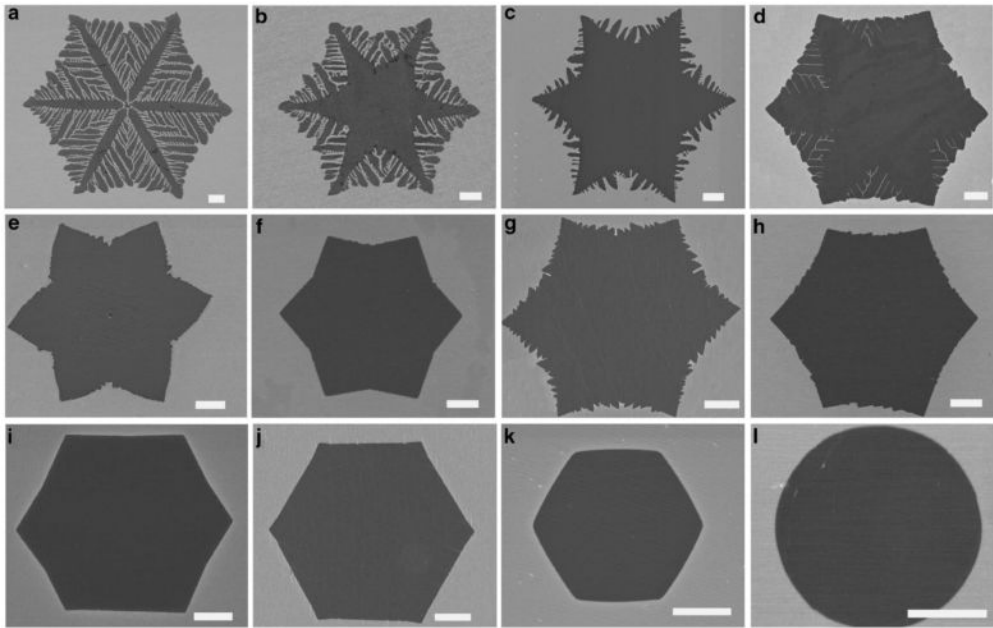


**Figure 2-7.** SEM images of graphene flakes grown on a liquid Cu surface with different shapes formed by varying the Ar/H<sub>2</sub> ratio and CH<sub>4</sub> gas flow. All the scale bars indicate 5 μm. Figures from [45]

<b>Method</b>	<b>Domain shape</b>	<b>Grain growth rate</b>	<b>Maximum lateral grain size</b>	<b>Reference</b>
<b>APCVD (multilayered)</b>	Hexagon	0.2	2	[35]
<b>PMMA seed, APCVD</b>	Hexagon	0.5	10	[48]
<b>CVD grown seed, APCVD</b>	Hexagon	1	15	[20]
<b>Ar anneal</b>	Hexagon	1.73	5000	[32]
<b>Ar anneal</b>	Hexagon	2	5900	[26]
<b>Resolidified Cu</b>	Hexagon	3.33	1000	[49]
<b>Vapor trapping</b>	Dendritic	5	100	[38]
<b>Suppression of Cu evaporation</b>	Dendritic	5.5	2000	[22]
<b>Cu enclosure</b>	Dendritic	6	400	[33]
<b><u>Liquid Cu</u></b>	Hexagon	6.66	100	[50]
<b>Two-step growth</b>	Four-lobed	10	10	[29]
<b><u>Liquid Cu</u></b>	Hexagon	10	100	[51]
<b>LPCVD</b>	Dendritic	10	50	[52]
<b>LPCVD</b>	Dendritic	16.6	100	[1]
<b><u>High pressure anneal</u></b>	Hexagonal	18.4	2300	[24]
<b>APCVD</b>	Dendritic	32.3	500	[2]

**Table 2-1.** . Domain shape, grain growth rate and maximum grain size of each graphene growth methods from literature which were calculated from SEM figures.

## 2.7. Approaches for large single crystal graphene

Following works are breakthrough in graphene growth in terms of grain size. Compared to few microns or tens of micrometer grain sizes which usually obtained by typical CVD, few studies report hundreds of micrometer sized graphene grains or even mm size single crystal by unique approaches.

### 2.7.1. Gas transport control

Several works have been done for understanding the role of gas transport and controlled growth for large single crystal graphene layer. Li *et al.*, used Cu foil enclosure for graphene growth.<sup>33</sup> They found out that growth behavior of interior and exterior of enclosure structure is quite different and mechanism of this gas transport controlled growth is still unclear. Due to limited supply of carbon source, growth rate was decreased in the interior of foil enclosure and graphene grown in the interior of foil shows large single crystal as 0.5 mm with highly dendritic shape. Also, Zhang and coworkers reported that vapor trapping growth in inner quartz tube results in similar growth behaviors.<sup>38</sup> Graphene grown in static gas flow in inner quartz tube shows highly dendritic shape and even flower-like edges and grain sizes are typically hundreds of microns. W. Fang *et al.*, also obtained different graphene interior and exterior of Cu foil enclosure.<sup>33</sup> Compared to large single crystal dendritic shape graphene interior of graphene, graphene grown on outside of the enclosure shows bilayer feature. Chen *et al.*, showed large single crystal graphene with mm-size by suppressing evaporative loss of Cu during the CVD growth, which was also gas transport control.<sup>22</sup> They claimed that suppressing evaporation of Cu results in smoother surface by sandwich structure, stacking Cu

foil and rolling foil. All those structures provided static vapor environment similar to previous works. S. Bhavirpudi *et al.*, investigated gas transport by comparing LP and APCVD system and achieved uniform graphene thickness at LPCVD.<sup>53</sup> They divided total CVD graphene growth as mass transfer by convection, diffusion through boundary layer and surface diffusion of active carbon species. Decreasing total pressure leads to fewer collisions and a higher diffusivity coefficient, consequently diffusion through boundary layer is no longer limiting step for graphene growth. So, at low pressure, surface reaction regime is rate limiting, which explains thickness uniformity of LPCVD graphene growth.

### **2.7.2. Seeded growth**

Pre-patterned graphene seeds were sometimes used for graphene growth. Q. Yu *et al.*,<sup>20</sup> grew graphene on Cu and patterned for seed formation, and then, regrew graphene by APCVD for periodic arrangements of graphene nuclei as shown in Figure 2-8. According to their results, other nuclei was not observed after regrowth process due to pre-existing seeds. Also, they measured electrical characteristics of inner and inter-grain graphene, which emphasized control of graphene grains during CVD. The same group did similar works by pre-patterning polymer seeds using poly-methyl methacrylate (PMMA).<sup>48</sup> Solid carbon source has been already known for graphene conversion by several groups, thus, they coated PMMA layer and patterned it for graphene seeds, and growth of pre-patterned PMMA shows well aligned graphene arrays.

Several papers reported that pre-anneal in Ar environment without hydrogen and smaller carbon feeding rate can reduce nuclei density of graphene at the growth

stage and enlarge grain sizes. For instance, L. Gan *et al.*,<sup>26</sup> explained that decreased nuclei density is owing to the seeded growth via Cu oxide passivation. According to their report, slight oxidation of Cu in Ar only atmosphere produces small CuO<sub>x</sub> nanoparticles, which controls graphene domain density eventually. Finally, they obtained 5.6 mm sized graphene grains. H. Zhou *et al.*, also obtained large single crystal via Ar anneal.<sup>32</sup> Graphene nucleation density was 4 nuclei/cm<sup>2</sup> and domain size was 5 mm according to their report, which was possible due to catalytic inactive Cu<sub>2</sub>O layer at the initial stage of growth. Their growth method anneals Ar only environment which can explain presence of Cu<sub>2</sub>O and its role as a high activation barrier for graphene nucleation. This fact is quite contradictory to previous idea that hydrogen anneal is required for reduction of Cu oxide for graphene growth. However, in order to provide low graphene nuclei density, CH<sub>4</sub> feeding rate should be extremely suppressed and followed growth rate is too slow. For instance, fully covered graphene films was not achieved with even 48 hours of growth time. Y. Hao *et al.*, well explained the role of surface oxygen which can be the reason for Ar anneal in graphene growth and centimeter scale graphene was achieved.<sup>25</sup> Oxygen rich Cu shows substantially decreased graphene nuclei density via passivation of active Cu surface. Oxygen also accelerated graphene domain growth and promoted diffusion-limited growth rather than edge-attachment-limited growth which was shown by dendritic growth behavior. They explained that pre-adsorbed oxygen on the Cu surface can enhance the dissociation of hydrocarbons by lowering activation energy and accelerating graphene growth.

### **2.7.3. Graphene growth on liquid Cu**

Graphene growth on liquid Cu can also be regarded as one of the way for

surface treatment of Cu. Geng *et al.*, proposed graphene growth on liquid state Cu.<sup>45,51,54</sup> Since Cu cannot wet on dielectric surfaces, Cu forms a ball and does not maintain its original sheet. Graphene was observed on the surface of liquid Cu ball, and it was found out that graphene islands on liquid Cu are uniform in their shape and arranged in the same orientation. They insisted that because the substrate is in the liquid state, there is no care for Cu orientation, grain boundaries, and even surface roughness. Graphene grown on liquid Cu shows self-assembled arrangement with the same orientation each other, which is believed to be the liquid nature of underlying substrate. If the graphene islands are arranged in the same orientation each other, followed grain boundaries would have no defects. Thus, despite of not that large size of graphene domains on liquid Cu, its importance should not be underestimated. They also used refractory metal as a platform for graphene growth on liquid Cu in order to maintain planar Cu sheet and graphene was grown.

Y. Wu *et al.*, also investigated liquid Cu for graphene growth substrate.<sup>50</sup> Hexagonal graphene flakes and continuous film was obtained on liquid Cu with Mo and W support. Similar alignment of graphene grains were confirmed and CH<sub>4</sub> and H<sub>2</sub> feeding rates were systematically controlled to achieve 200 μm sized single crystal. Not only liquid form of Cu, but resolidified form (solidified after melt) of Cu was known to be effective for smoothing Cu surface and advantageous for graphene growth.<sup>49</sup> Millimeter sized graphene grains with hexagon-shaped and monolayer were reported by melting and subsequent resolidification of Cu on W support. They compared surface treatment for Cu including thermal annealing, EP and resolidification. It was found out that resolidification provides the lowest graphene nuclei density. This low nuclei density is owing to the improvement of

surface flatness according to their AFM results.

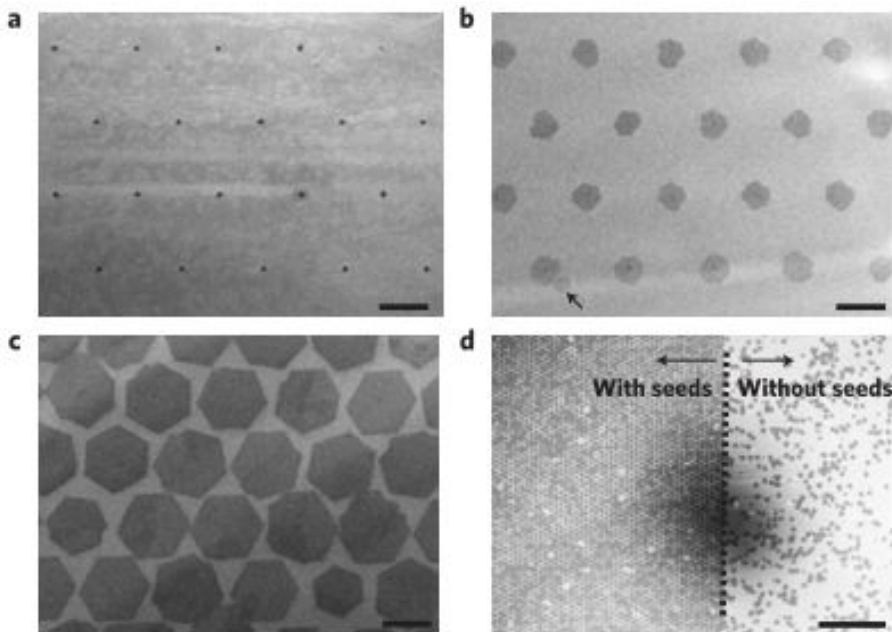


**Figure 2-8.** Pre-patterned graphene seeds and regrown graphene islands. (Figures adapted from [21]) (a) Graphene seed which were formed by pre-growth and e-beam lithography patterning, (b) Typical graphene grains after re-growth, (c) further growth results in larger grains, and (d) Low magnification image showing

different growth behavior of graphene growth with seed area and random nucleation.

## References

1. C. Jia, J. Jiang, L. Gan and X. Guo, *Scientific reports* **2**, 707 (2012).
2. H. Wang, G. Wang, P. Bao, S. Yang, W. Zhu, X. Xie and W.-J. Zhang, *J. Am. Chem. Soc.* **134** (8), 3627-3630 (2012).
3. D. L. Duong, G. H. Han, S. M. Lee, F. Gunes, E. S. Kim, S. T. Kim, H. Kim, Q. H. Ta, K. P. So, S. J. Yoon, S. J. Chae, Y. W. Jo, M. H. Park, S. H. Chae, S. C. Lim, J. Y. Choi and Y. H. Lee, *Nature* **490** (7419), 235-239 (2012).
4. D. L. Duong, G. H. Han, S. M. Lee, F. Gunes, E. S. Kim, S. T. Kim, H. Kim, Q. H. Ta, K. P. So, S. J. Yoon, S. J. Chae, Y. W. Jo, M. H. Park, S. H. Chae, S. C. Lim, J. Y. Choi and Y. H. Lee, *Nature* **490** (7419), 235-239 (2012).
5. A. C. Ferrari, J. C. Meyer, V. Scardaci, C. Casiraghi, M. Lazzeri, F. Mauri, S. Piscanec, D. Jiang, K. S. Novoselov, S. Roth and A. K. Geim, *Phys. Rev. Lett.* **97** (18), 187401 (2006).
6. L. G. Cancado, K. Takai, T. Enoki, M. Endo, Y. A. Kim, H. Mizusaki, A. Jorio, L. N. Coelho, R. Magalhaes-Paniago and M. A. Pimenta, *Appl. Phys. Lett.* **88** (16), 163106-163103 (2006).
7. J. M. Wofford, S. Nie, K. F. McCarty, N. C. Bartelt and O. D. Dubon, *Nano Letters* **10** (12), 4890-4896 (2010).
8. S. Nie, J. M. Wofford, N. C. Bartelt, O. D. Dubon and K. F. McCarty, *Physical Review B* **84** (15), 155425 (2011).
9. J. An, E. Voelkl, J. W. Suk, X. Li, C. W. Magnuson, L. Fu, P. Tiemeijer, M. Bischoff, B. Freitag, E. Popova and R. S. Ruoff, *ACS Nano* **5** (4), 2433-2439 (2011).
10. P. Y. Huang, C. S. Ruiz-Vargas, A. M. van der Zande, W. S. Whitney, M. P.

- Levendorf, J. W. Kevek, S. Garg, J. S. Alden, C. J. Hustedt, Y. Zhu, J. Park, P. L. McEuen and D. A. Muller, *Nature* **469** (7330), 389-392 (2011).
11. A. W. Robertson and J. H. Warner, *Nanoscale* **5** (10), 4079-4093 (2013).
12. F. Banhart, J. Kotakoski and A. V. Krashennnikov, *ACS Nano* **5** (1), 26-41 (2010).
13. H. I. Rasool, E. B. Song, M. J. Allen, J. K. Wassei, R. B. Kaner, K. L. Wang, B. H. Weiller and J. K. Gimzewski, *Nano Letters* **11** (1), 251-256 (2010).
14. J. Cho, L. Gao, J. Tian, H. Cao, W. Wu, Q. Yu, E. N. Yitamben, B. Fisher, J. R. Guest, Y. P. Chen and N. P. Guisinger, *ACS Nano* **5** (5), 3607-3613 (2011).
15. J. Tian, H. Cao, W. Wu, Q. Yu and Y. P. Chen, *Nano Lett* **11** (9), 3663-3668 (2011).
16. L. Li, S. Reich and J. Robertson, *Physical Review B* **72** (18), 184109 (2005).
17. T. G. Schmalz, W. A. Seitz, D. J. Klein and G. E. Hite, *J. Am. Chem. Soc.* **110** (4), 1113-1127 (1988).
18. K. Kim, Z. Lee, W. Regan, C. Kisielowski, M. F. Crommie and A. Zettl, *ACS Nano* **5** (3), 2142-2146 (2011).
19. A. W. Tsen, L. Brown, M. P. Levendorf, F. Ghahari, P. Y. Huang, R. W. Havener, C. S. Ruiz-Vargas, D. A. Muller, P. Kim and J. Park, *Science* **336** (6085), 1143-1146 (2012).
20. Q. Yu, L. A. Jauregui, W. Wu, R. Colby, J. Tian, Z. Su, H. Cao, Z. Liu, D. Pandey, D. Wei, T. F. Chung, P. Peng, N. P. Guisinger, E. A. Stach, J. Bao, S.-S. Pei and Y. P. Chen, *Nat Mater* **10** (6), 443-449 (2011).
20. Z. Luo, Y. Lu, D. W. Singer, M. E. Berck, L. A. Somers, B. R. Goldsmith and A. T. C. Johnson, *Chem. Mater.* **23** (6), 1441-1447 (2011).
21. I. Vlassioux, S. Smirnov, M. Regmi, S. P. Surwade, N. Srivastava, R. Feenstra,

- G. Eres, C. Parish, N. Lavrik, P. Datskos, S. Dai and P. Fulvio, *The Journal of Physical Chemistry C* **117** (37), 18919-18926 (2013).
22. S. Chen, H. Ji, H. Chou, Q. Li, H. Li, J. W. Suk, R. Piner, L. Liao, W. Cai and R. S. Ruoff, *Adv. Mater.* **25** (14), 2062-2065 (2013).
23. T. Wu, G. Ding, H. Shen, H. Wang, L. Sun, D. Jiang, X. Xie and M. Jiang, *Adv. Funct. Mater.* **23** (2), 198-203 (2013).
24. Z. Yan, J. Lin, Z. Peng, Z. Sun, Y. Zhu, L. Li, C. Xiang, E. L. Samuel, C. Kittrell and J. M. Tour, *ACS Nano* **6** (10), 9110-9117 (2012).
25. Y. Hao, M. S. Bharathi, L. Wang, Y. Liu, H. Chen, S. Nie, X. Wang, H. Chou, C. Tan, B. Fallahzad, H. Ramanarayan, C. W. Magnuson, E. Tutuc, B. I. Yakobson, K. F. McCarty, Y. W. Zhang, P. Kim, J. Hone, L. Colombo and R. S. Ruoff, *Science* **342** (6159), 720-723 (2013).
26. L. Gan and Z. Luo, *ACS Nano* **7** (10), 9480-9488 (2013).
27. G. H. Han, F. Güneş, J. J. Bae, E. S. Kim, S. J. Chae, H.-J. Shin, J.-Y. Choi, D. Pribat and Y. H. Lee, *Nano Letters* **11** (10), 4144-4148 (2011).
28. C. Hwang, K. Yoo, S. J. Kim, E. K. Seo, H. Yu and L. P. Biró, *The Journal of Physical Chemistry C* **115** (45), 22369-22374 (2011).
29. X. Li, C. W. Magnuson, A. Venugopal, J. An, J. W. Suk, B. Han, M. Borysiak, W. Cai, A. Velamakanni, Y. Zhu, L. Fu, E. M. Vogel, E. Voelkl, L. Colombo and R. S. Ruoff, *Nano Letters* **10** (11), 4328-4334 (2010).
30. K. Celebi, M. T. Cole, K. B. K. Teo and H. G. Park, *Electrochem. Solid State Lett.* **15** (1), K1-K4 (2012).
31. H. Kim, C. Mattevi, M. R. Calvo, J. C. Oberg, L. Artiglia, S. Agnoli, C. F. Hirjibehedin, M. Chhowalla and E. Saiz, *ACS Nano* **6** (4), 3614-3623 (2012).
32. H. Zhou, W. J. Yu, L. Liu, R. Cheng, Y. Chen, X. Huang, Y. Liu, Y. Wang, Y.

- Huang and X. Duan, *Nat Commun* **4**, 2096 (2013).
33. X. Li, C. W. Magnuson, A. Venugopal, R. M. Tromp, J. B. Hannon, E. M. Vogel, L. Colombo and R. S. Ruoff, *J. Am. Chem. Soc.* **133** (9), 2816-2819 (2011).
34. D. A. Porter and K. E. Easterling, *Phase transformations in metals and alloys*. (Chapman & Hall, 1992).
35. B. Wu, D. Geng, Y. Guo, L. Huang, Y. Xue, J. Zheng, J. Chen, G. Yu, Y. Liu, L. Jiang and W. Hu, *Adv. Mater.* **23** (31), 3522-3525 (2011).
36. Z. Sun, A.-R. O. Raji, Y. Zhu, C. Xiang, Z. Yan, C. Kittrell, E. L. G. Samuel and J. M. Tour, *ACS Nano* **6** (11), 9790-9796 (2012).
37. W. Wei, Y. Qingkai, P. Peng, L. Zhihong, B. Jiming and P. Shin-Shem, *Nanotechnology* **23** (3), 035603 (2012).
38. Y. Zhang, L. Zhang, P. Kim, M. Ge, Z. Li and C. Zhou, *Nano Letters* **12** (6), 2810-2816 (2012).
39. A. T. Murdock, A. Koos, T. B. Britton, L. Houben, T. Batten, T. Zhang, A. J. Wilkinson, R. E. Dunin-Borkowski, C. E. Lekka and N. Grobert, *ACS Nano* **7** (2), 1351-1359 (2013).
40. Y. A. Wu, A. W. Robertson, F. Schaffel, S. C. Speller and J. H. Warner, *Chem. Mater.* **23** (20), 4543-4547 (2011).
41. F. Lili, Z. Jie, L. Zhen, L. Xiao, W. Kunlin, W. Jinquan, Z. Minlin, W. Dehai, X. Zhiping and Z. Hongwei, *Nanotechnology* **23** (11), 115605 (2012).
42. E. Meca, J. Lowengrub, H. Kim, C. Mattevi and V. B. Shenoy, *Nano Lett* **13** (11), 5692-5697 (2013).
43. Ç. Ö. Girit, J. C. Meyer, R. Erni, M. D. Rossell, C. Kisielowski, L. Yang, C.-H. Park, M. F. Crommie, M. L. Cohen, S. G. Louie and A. Zettl, *Science* **323** (5922), 1705-1708 (2009).

44. Z. Luo, S. Kim, N. Kawamoto, A. M. Rappe and A. T. Johnson, *ACS Nano* **5** (11), 9154-9160 (2011).
45. B. Wu, D. Geng, Z. Xu, Y. Guo, L. Huang, Y. Xue, J. Chen, G. Yu and Y. Liu, *NPG Asia Mater* **5**, e36 (2013).
46. X. Zhang, L. Wang, J. Xin, B. I. Yakobson and F. Ding, *J Am Chem Soc* **136** (8), 3040-3047 (2014).
47. Y. Zhang, Z. Li, P. Kim, L. Zhang and C. Zhou, *ACS Nano* **6** (1), 126-132 (2011).
48. W. Wu, L. A. Jauregui, Z. Su, Z. Liu, J. Bao, Y. P. Chen and Q. Yu, *Adv Mater* **23** (42), 4898-4903 (2011).
49. A. Mohsin, L. Liu, P. Liu, W. Deng, I. N. Ivanov, G. Li, O. E. Dyck, G. Duscher, J. R. Dunlap, K. Xiao and G. Gu, *ACS Nano* **7** (10), 8924-8931 (2013).
50. Y. A. Wu, Y. Fan, S. Speller, G. L. Creeth, J. T. Sadowski, K. He, A. W. Robertson, C. S. Allen and J. H. Warner, *ACS Nano* **6** (6), 5010-5017 (2012).
51. D. Geng, B. Wu, Y. Guo, L. Huang, Y. Xue, J. Chen, G. Yu, L. Jiang, W. Hu and Y. Liu, *Proceedings of the National Academy of Sciences of the United States of America* **109** (21), 7992-7996 (2012).
52. Y. Wu, Y. Hao, H. Y. Jeong, Z. Lee, S. Chen, W. Jiang, Q. Wu, R. D. Piner, J. Kang and R. S. Ruoff, *Adv Mater* **25** (46), 6744-6751 (2013).
53. S. Bhaviripudi, X. Jia, M. S. Dresselhaus and J. Kong, *Nano Letters* **10** (10), 4128-4133 (2010).
54. D. Geng, B. Luo, J. Xu, Y. Guo, B. Wu, W. Hu, Y. Liu and G. Yu, *Adv. Funct. Mater.* **24** (12), 1664-1670 (2014).



## CHAPTER 3.

# **Direct graphene growth on target substrate: Metal-induced crystallization of a-C**

This chapter is based on the article published in  
Nanotechnology **23**, 115301 (2012).



### 3.1. Introduction

Graphene has attracted a great interest not only for its scientific purpose, but also for its outstanding electrical, optical and other properties.<sup>1-4</sup> Large area graphene film is typically grown by chemical vapor deposition (CVD) methods with a transition metal such as nickel and copper as catalyst<sup>5-9</sup> or heating a solid carbon source on a metal.<sup>10</sup> Although the metal can be removed in-situ by evaporating the metal on an insulator at 1,000 °C under vacuum for more than several hours,<sup>11</sup> the metal is usually removed by a suitable method such as wet etching and then the recovered graphene film is transferred to the substrate of interest.<sup>5-9</sup> It would be desirable to be able to grow graphene film on any surface (mainly dielectric) *in-situ* without restrictions on the size and the location of the film formation, and without too demanding process conditions. These attributes that are highly desirable of graphene film growth and essential for device applications are realized in this work in the form of graphene-metal hybrid film for transparent and conductive film.

Although metals have been used as a catalyst for converting hydrocarbon materials to graphene, they can also be used for metal-induced crystallization (MIC) of amorphous materials. In fact, utilization of MIC for graphitic carbon formation was already suggested a few decades ago.<sup>12-14</sup> Physical contact between metal crystal and carbon source is considered to be important for its catalytic effect. However, the mechanism of crystallization has not been clearly established. A recent work utilized MIC to grow a graphene film with controllable thickness.<sup>15-17</sup> The crystallization method offers certain advantages over CVD methods and

thermal annealing techniques in that it involves conversion of only amorphous carbon to graphene whereas the others require, in addition, dissociation of hydrocarbon source material. A net result is a significant reduction in the growth temperature, which was reduced to 500~700 °C<sup>15,18</sup> from 800 ~ 1,000 °C<sup>5-9</sup> that is needed for the other thermal CVD method without plasma.

The main concept in our approach, which is the utilization of an ultra-thin metal layer in MIC, or ultra-thin MIC (UTMIC), came from our preliminary experiment in which thin layers of metal on quartz were annealed to obtain high transmittance under annealing conditions. We expected that the thin metal layers less than 10 nm thick would break up upon annealing, leading to formation of nano-crystallites. We found, in addition, that the transmittance in the visible range increases with increasing annealing temperature and that, for 10 nm thick metal layer, for instance, there was very little loss of transmittance upon annealing at 600 °C as shown in Figure 3-1. Use of an ultra-thin metal layer, as we will find, provides one with a capability to enhance transmittance of graphene film. The thin metal layer also makes it possible to grow graphene at 400 °C, one of the lowest conversion temperature ever reported, in a short time of 10 seconds, which is the shortest heating time ever for graphene formation based on dry synthesis. The low temperature and in particular the short annealing time must have to do with the diffusion of carbon through the metal layer that is needed for the graphene formation on top of the metal layer. In an earlier work involving MIC,<sup>15</sup> it took an annealing time of 15 minutes at 800 °C to form graphene with 300 nm thick nickel layer. The time needed for diffusion<sup>19</sup> is proportional to the square of the diffusion length. Therefore, the diffusion time for 300-nm-thick layer is almost 1,000 times longer than for 10-nm-thick layer, which explains the short annealing time.



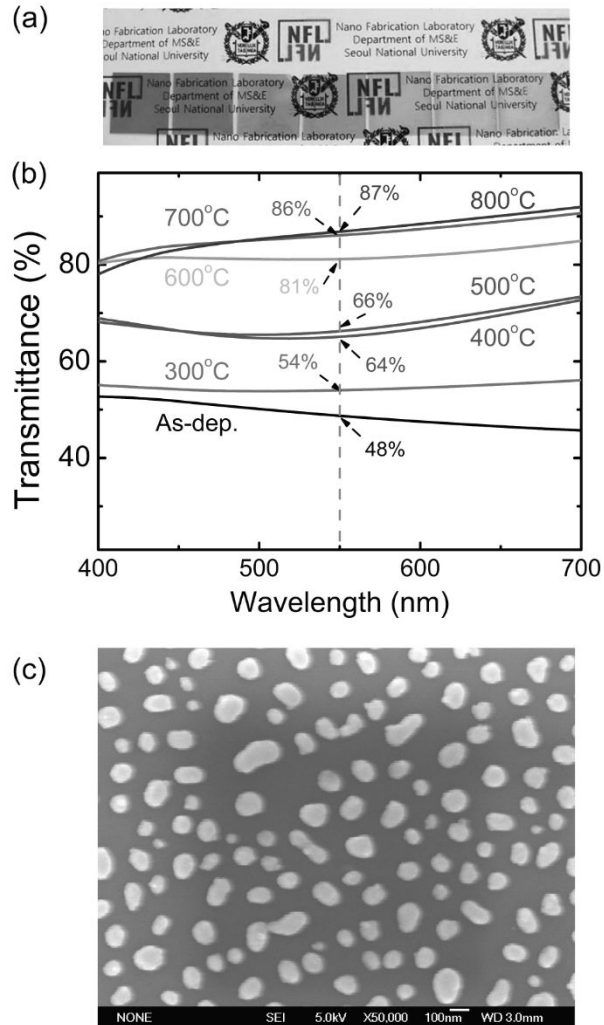


**Figure 3-1.** (a) Photographs of as-deposited, and annealed (from 300 °C to 800 °C in sequence) nickel film (without a-C). (b) Transmittance value of (a) at the wavelength range of visible rays. (c) SEM image of 800 °C annealed sample showing nickel nano-crystallite. (Scale bar indicates 100 nm)

## 3.2. Experimental details

The formation of graphene-metal hybrid film for transparent electrodes by the rapid UTMIC process is schematically illustrated in Figure 3-2. If needed, on any given surface, regardless of the size, or only on a patterned surface if desired, amorphous carbon (a-C) can be deposited followed by deposition of a metal. The graphene-metal hybrid film is a continuous film of graphene underneath of which lie nano-crystallites of metal, as illustrated in Figure 3-2. (b). The thickness of a-C should be as thin as possible for high transmittance of light. When the thickness was less than 1 nm, however, no continuous film of a-C formed, as indicated by inability of four point probe equipment to produce any measured value (measurable limit for sheet resistance was  $108 \Omega/\text{sq.}$  by our 4-point probe equipment) as shown in Figure 3-3. Therefore, the thickness of a-C was fixed to 1 nm for all experiments, unless otherwise noted. Nickel was chosen as the metal in UTMIC for faster agglomeration of metal nano-crystallites upon annealing because its surface energy is one of the highest among metals.<sup>20</sup>

### 3.2.1. Deposition and sample preparation

1 nm-thick a-C and 3, 8, and 10 nm-thick Ni layers were sequentially deposited without exposure to ambient condition using electron beam evaporator. Evaporation was done after evacuating the chamber to base pressure  $\sim 9 * 10^{-6}$  Torr (1 Torr = 133.32 Pa). All the films were deposited at the deposition rate of  $\sim 0.5$  Å/second which was slow enough to control the thickness of very thin layers. Both quartz (thickness: 500  $\mu\text{m}$ ) and thermally grown  $\text{SiO}_2$  100 nm / Si (100) wafer (for

cross-sectional transmission electron microscopy (TEM) specimen preparation by ion beam milling) were used as a substrate. Heat treatment was done with Rapid thermal annealing (RTA) system with quartz tube chamber around halogen lamp. Heating rate was  $\sim 80$  °C /second while temperature was varied from 300 to 1,000 °C. Process pressure was 5 Torr with Ar/H<sub>2</sub> = 2:1 ambient. Ten seconds of heating was sufficient for the formation of the graphene film. After annealing, chamber was cooled down under Ar ambient to the room temperature prior to unloading samples.

### **3.2.2. Analysis of the film**

Transmittance was measured by UV-Vis spectroscopy (Varian Cary 50 Series) in the visible wavelength from 400 nm to 700 nm. Bare quartz was used as a reference for transmittance measurement. High resolution TEM (HRTEM) analysis was done by JEOL JEM-3000F system. Scanning electron microscopy (SEM) analysis was carried out by JEOL-7401F. Sheet resistance was measured by four-point probe. Raman analysis was done by LabRAM HR-800 System, Horiba with 532 nm solid-state laser, and objective lens magnification was 100x. Spectral resolution of Raman was  $1.47$  cm<sup>-1</sup>.

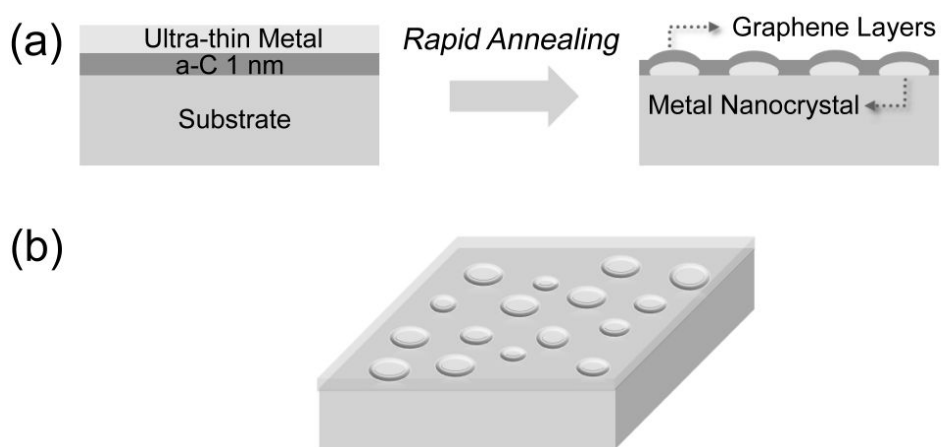


**Figure 3-2.** (a) Diagram showing the formation of the graphene-metal hybrid by metal-induced crystallization of a-C and agglomeration of ultra-thin metal film, (b) Bird's eye view of the film.

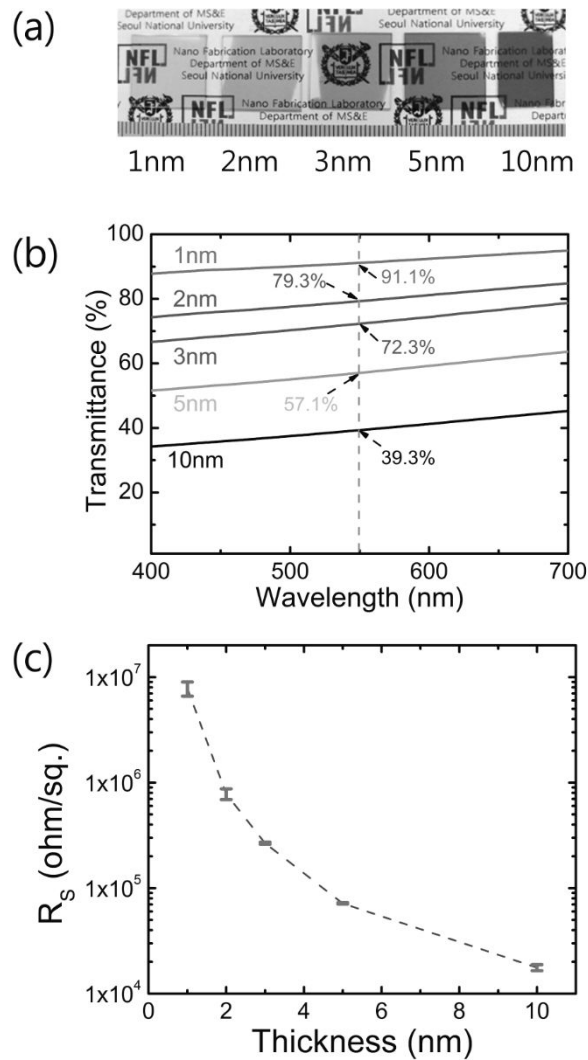


**Figure 3-3.** (a) Photographs of various thickness of as-deposited a-C. (b) Transmittance value of (a) at the wavelength range of visible rays. (c) Sheet resistance value of (a).

### 3.3. Results and Discussion

There are two main properties of interest for a transparent electrode, which are light transmittance in the visible range and sheet resistance or resistivity. The sheet resistance plotted against the transmittance is shown in Figure 3-4 for the graphene-metal hybrid films generated with nickel layers of three different thicknesses: 3, 8, and 10 nm. For each layer thickness, the annealing temperature was varied from 300 to 800 °C to follow the trends of the two properties that accompany the changes in the temperature. The initial states in terms of the transmittance and resistance for the three cases can readily be understood, in that a thicker metal layer results in a lower transmittance and at the same time a lower sheet resistance. The fact that the resistance can be measured, even though the metal is fully aggregated, is an indication that the graphene films formed are continuous for all the different conditions.

One trend that is common to all three cases is that the resistance increases sharply with increasing temperature, which is accompanied by a gradual increase in the transmittance, and then it reaches a plateau, where the sheet resistance remains almost the same with increasing temperature. However, the transmittance keeps increasing with increasing temperature. The picture emerging here is that when the metal layer breaks up, the conduction paths through the metal layer are lost and eventually the metal structure reaches the conduction percolation threshold beyond which there is no conduction contribution from the metal and the conduction is entirely by graphene film. The plateau reached as the temperature is increased must be the sheet resistance of the graphene film. We also confirmed resistance of a-C

without Ni as a comparison as you can see in the Figure 3-3, the value is far higher than graphene layers formed by catalytic effect. All the graphene film shows lower resistance than a-C without Ni.

The behavior of the graphene-metal hybrid film at the plateau needs further explanation. When nano-crystallites form after the break up, they sinter faster at higher temperature, leading to more agglomeration of the crystallites. Therefore, more exposed surface for light transmission becomes available with increasing annealing temperature, resulting in a higher transmittance. Since the metal no longer contributes to the conduction once it reaches the plateau, the resistance remains constant with increasing temperature. The dependence of the ultimate transmittance, or the transmittance that will eventually be reached upon increasing temperature, on the nickel layer thickness that is shown in Figure 3-4, is self-evident in that a thicker layer and thus larger crystallites should result in a lower transmittance due to more blockage of light.

The dependence of the sheet resistance on the metal layer thickness requires further elaboration. Shown in Figure 3-5 (a) are the Raman spectra (excitation wavelength: 532 nm) obtained as a function of annealing temperature for the bilayer structure consisting of 10 nm Ni on 1 nm a-C. It is immediately clear from G and 2D peaks that the graphene film forms at 400 °C. A close examination of the spectra at three different temperatures should reveal that the intensity ratio of peak D to peak G, or D/G peak intensity ratio, is independent of temperature, which starkly contrasts the typical temperature dependence of the D/G intensity ratio for thick metal layer, as shown in Figure 3-6. The grain size of graphene can be correlated to the D/G peak ratio<sup>21</sup> as follows,

$$L_a (nm) = (2.4 \times 10^{-10}) \lambda^4 \left( \frac{I_D}{I_G} \right)^{-1} \quad \dots 3-(1)$$

where  $L_a$  is the grain size,  $\lambda$  is the excitation wavelength,  $I_D$  and  $I_G$ , respectively, are the intensities of D and G peak. It follows from the relationship that the graphene grain size is independent of annealing temperature for the ultra-thin metal layer while it depends on the temperature for thick metal layer. To gain an understanding of the resistance behavior at the plateau as affected by the metal thickness, the Raman spectra for the three different metal thicknesses were obtained at the annealing temperature of 500 °C, as shown in Figure 3-6. (b). The figure clearly shows that the D/G intensity ratio decreases with increasing metal thickness, which means that the graphene grain size increases with increasing metal thickness according to equation (1). It is natural that the resistance increases with decreasing grain size, which explains the lowering of the sheet resistance with increasing metal thickness as is shown in Figure 3-4 at the plateau.

To have an understanding of the way the metal thickness affects the graphene grain size, the grain size of metal was measured for various metal thicknesses since the grain size is known to decrease with decreasing metal thickness, as the data in Figure 3-7 reveals, and since a reduction in the metal grain size could be related to a decrease in the grain size of graphene. A smaller metal grain size offer much more nucleation sites<sup>22, 23</sup> and therefore the grain size of graphene should decrease with decreasing metal grain size. For this nucleation-controlled growth, there is no temperature dependence but only thickness dependence or dependence on metal grain size, which contrasts the grain growth for thick metal layer in Figure 3-6 where surface diffusion controls the growth and hence the growth depends on

temperature. Shown in Figure 3-5 (c) are the D/G intensity ratio of graphene film and the sheet resistance plotted as a function of the metal thickness. The two curves in the figure nearly coincide, which means that the sheet resistance is proportional to the D/G intensity ratio. Thus, this nucleation-controlled growth in UTMIC can explain that we can nearly detect 2D peak evolution in 3 nm UTMIC in Figure 3-5 (b) since smaller grain size of Ni can provide larger nuclei density.

Uniformity of the graphene-metal hybrid film quality in terms of D/G intensity ratio is relatively good as the micro Raman mapping over an area of 39  $\mu\text{m}$  by 39  $\mu\text{m}$  in Figure 3-8 shows. The intensity ratio in the mapping ranges between 1.05 and 1.28 for the graphene film grown from the bilayer of 3 nm Ni / 1 nm a-C. The relationship between D/G intensity ratio and sheet resistance, which is established here for the first time, indicates that the sheet resistance lies between 5 and 7 \* 10<sup>5</sup>  $\Omega/\text{sq}$ . over the mapping area. The transmittance behavior of the graphene-metal hybrid film as affected by the ultra-thin metal layer is shown in Figure 3-9 (a) for the film grown from the bilayer of 3 nm Ni on 1 nm a-C. The transmission electron microscopy (TEM) image in Figure 3-9 (b) for the sample annealed to 500 °C reveals that the underlying substrate surface is exposed with completely separated metal crystallites, typically less than 100 nm in size, dotting the surface underneath the graphene film. For thicker Ni case, (10 nm Ni / 1 nm a-C or 8 nm Ni / 1 nm a-C) the crystallites size was also less than micron. As the size of the crystallites is smaller than the wavelength in the visible range, the film appears quite transparent as the optical photographs shows. The transmittance curves given in Figure 3-9 (c) for various annealing temperatures indicate that the transmittance can easily be made to exceed 80 %. We also tried wet-etching of nickel islands in Figure 3-9 (c), but the islands are nearly etched and do not change performance even after few

hours of dipping in  $\text{FeCl}_3$  / HCl solution which is frequently used as a nickel etchant. This fact indicates that graphene layers covers nickel islands after annealing, which is also an evidence of our proposed mechanism that graphene covers metal nanoparticles as shown in Figure 3-10.

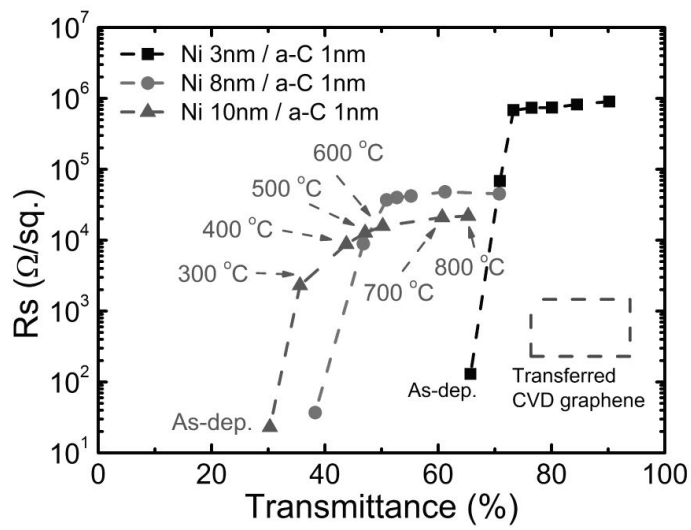


**Figure 3-4.** Sheet resistance versus transmittance curve of each samples made of various thickness of nickel catalyst, annealing temperature from 300 °C to 800 °C (a-C thickness was fixed as 1nm).

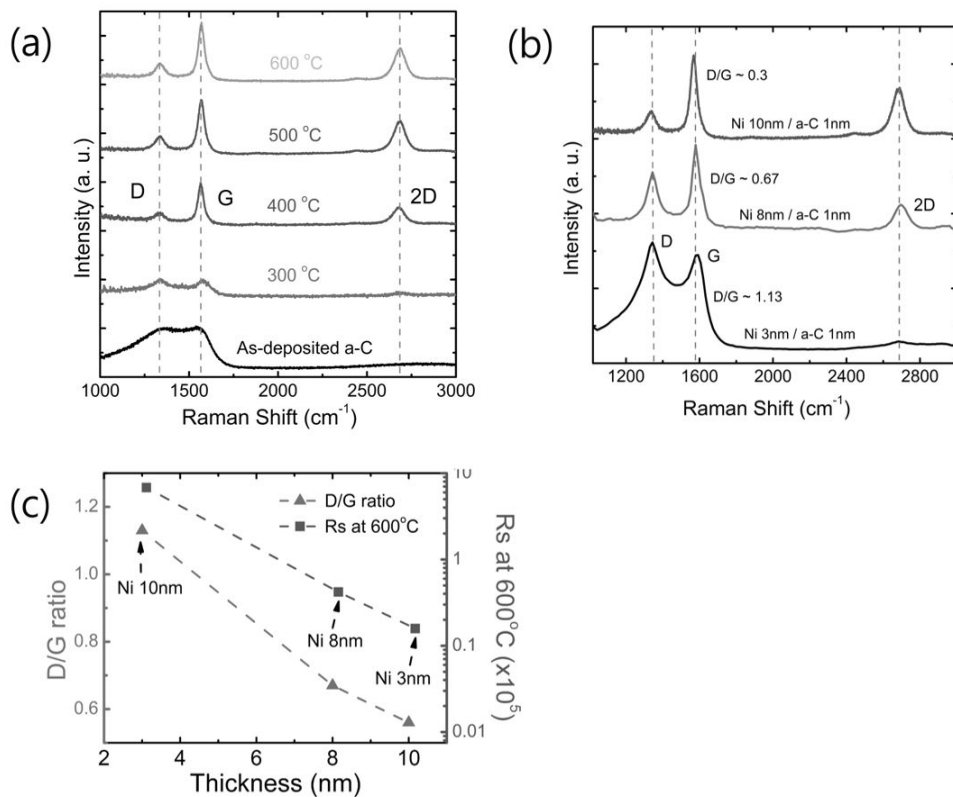


**Figure 3-5.** (a) Raman spectra of as-deposited and 300 °C, 400 °C, 500 °C, and 600 °C annealed bi-layer (Ni 10nm / a-C 1nm) sample. (b) Raman spectra of bilayer structure with various Ni thicknesses at annealing temperature of 500 °C. (c) Correlation between D/G peak ratio and sheet resistance (unit: Ω/sq.) of 600 °C (chosen as an arbitrary temperature, similar behaviors were shown at different temperature) annealed at each thickness of metal catalyst.

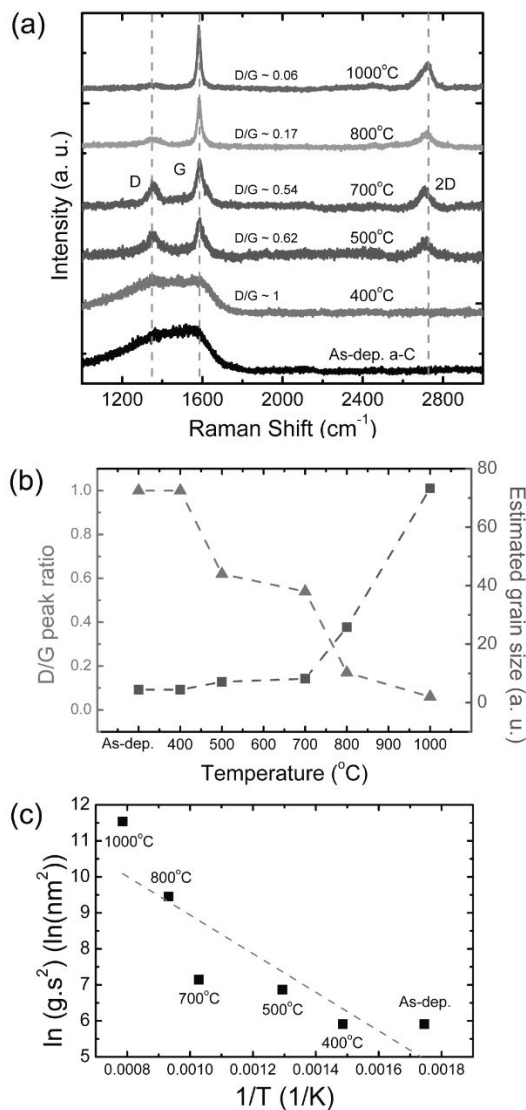


**Figure 3-6.** Raman spectra of as-deposited a-C and crystallized graphene layers on top of continuous nickel (350 nm) after heat treatment at various annealing temperatures. (Initial a-C layer was deposited on top of Ni in order to understand crystallization behavior of a-C on thick Ni) (b) Estimated grain size of graphene based on D/G peak intensity ratio.

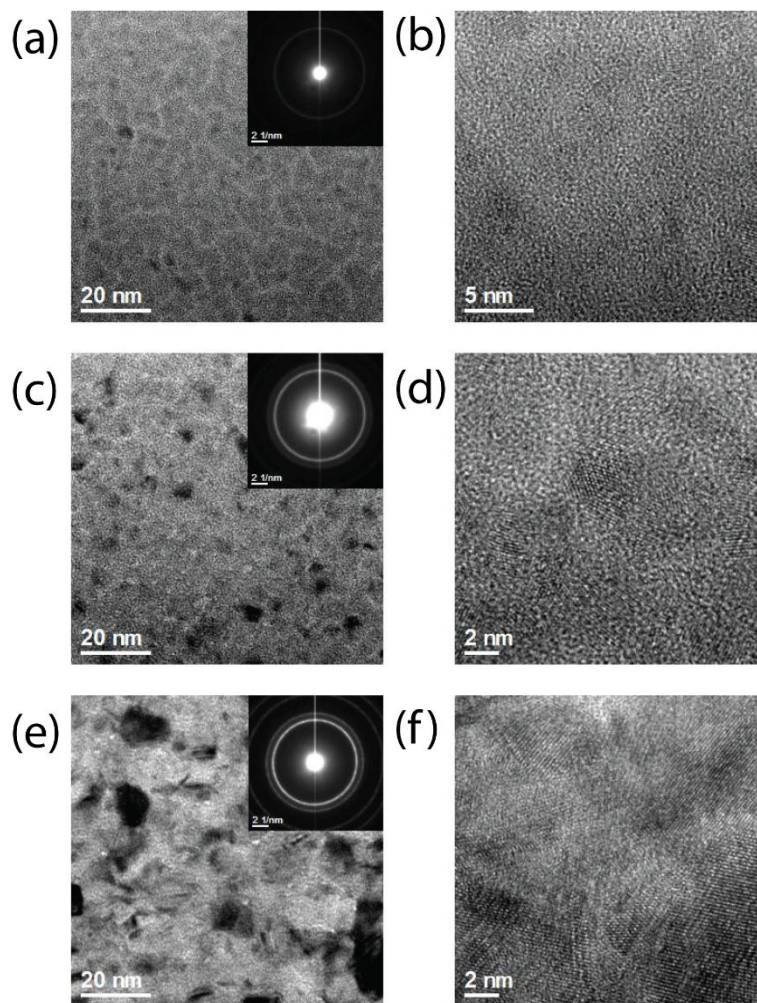


**Figure 3-7.** Plan-view TEM images of as-deposited (a), (b) 3-nm-thick, (c), (d) 10-nm-thick, and (e), (f) 30-nm-thick nickel films on carbon grid. (a), (c), (e) indicate bright-field TEM images and (b), (d), (f) indicate high-resolution TEM images. Scale bar in (a), (c), (e) corresponds to 20 nm.

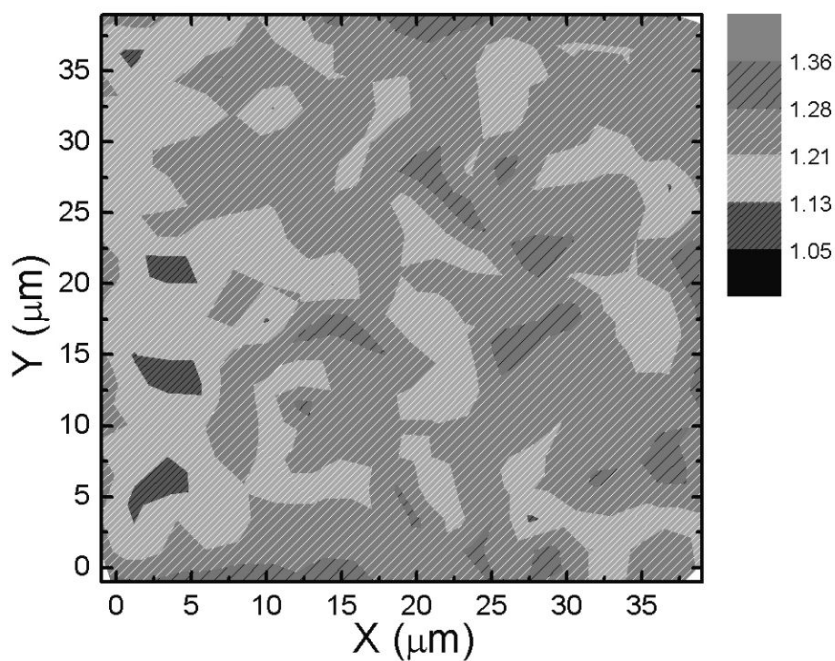


**Figure 3-8.** Raman spectra of as-deposited a-C and crystallized graphene layers on top of continuous nickel (350 nm) after heat treatment at various annealing temperatures. (Initial a-C layer was deposited on top of Ni in order to understand crystallization behavior of a-C on thick Ni) (b) Estimated grain size of graphene based on D/G peak intensity ratio.

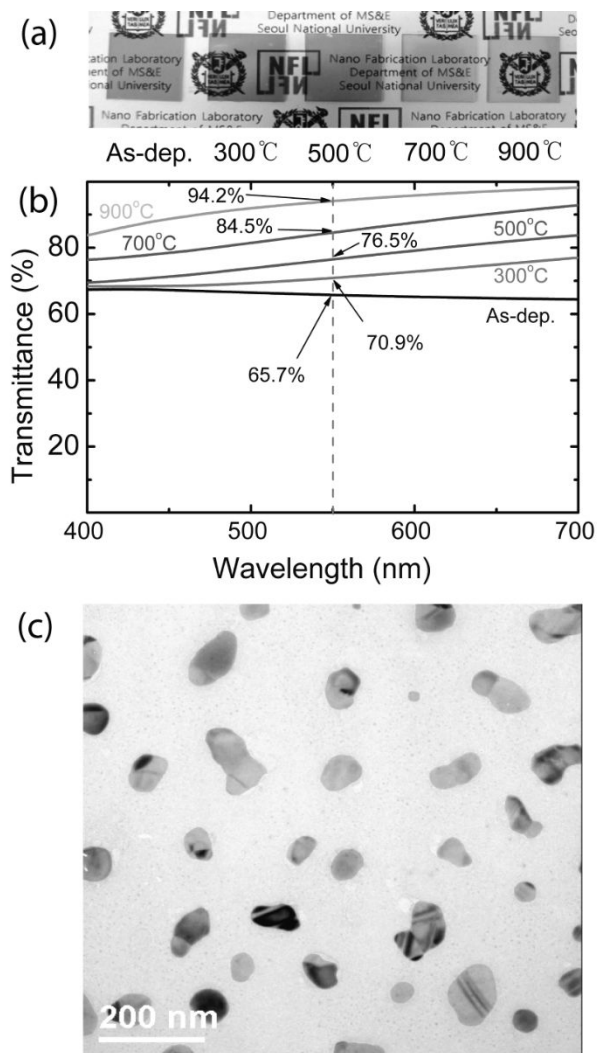


**Figure 3-9.** (a) Photographs of as-deposited, and annealed (300, 500, 700, and 900 °C) samples for Ni 3nm / a-C 1nm bilayer structure. (b) Transmittance curve at visible wavelength of samples in a). (c) plan-view bright field TEM image of 500 °C annealed bilayer structure (Ni 3nm / a-C 1nm). Scale bar in (c) indicates 200 nm.

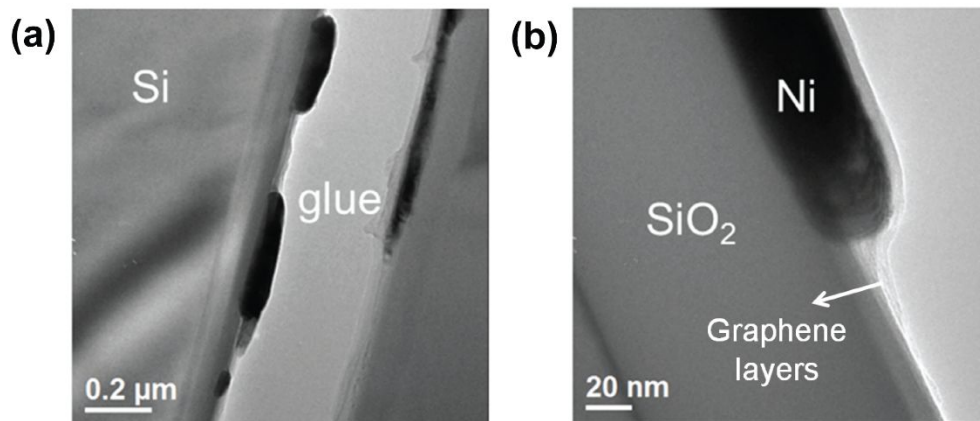


**Figure 3-10.** (a) Cross-sectional TEM image of graphene-metal hybrid film layers (from Ni 10 nm / a-C 3 nm structure, annealed at 600 °C). (thicker a-C layer was used for better observation of graphene layers formed by UTMIC) (b) cross-sectional TEM image of (a) structure showing that nickel agglomerate is surrounded by graphene layers.

### **3.4. Summary and Conclusions**

The fate of the graphene film formed by UTMIC as a transparent electrode is entirely determined by the ultra-thin metal layer. The ultra-thin metal layer allows the formation of graphene transparent electrode film, without requiring any transfer of the film, on any substrate regardless of the size, patterned or non-patterned, and only on desired locations if desired, in 10 seconds of heating. In so doing, it does not contribute to electrical conduction nor does it impede light transmission. Because of the sintering taking place, the transmittance can easily reach better than 90 %. The sheet resistance of graphene, which is more than three orders of magnitude away from the practical level of  $10^2 \Omega/\text{sq.}$ , is also entirely determined by the metal layer. The resistance is high because of the small grain size that usually comes with thin metal layer.

## References

1. K. S. Novoselov, A. K. Geim, S. V. Morozov, D. Jiang, Y. Zhang, S. V. Dubonos, I. V. Grigorieva, A. A. Firsov, *Science* **306**, 666 (2005)
2. K. S. Novoselov, D. Jiang, F. Schedin, T. J. Booth, V. V. Khotkevich, S. V. Morozov, A. K. Geim, *Proc. Nat. Acad. Sci.* **102**, 10451 (2005)
3. K. S. Novoselov, A. K. Geim, S. V. Morozov, D. Jiang, M. I. Katsnelson, I. V. Grigorieva, S. V. Dubonos, A. A. Firsov, *Nature* **438**, 197 (2005)
4. R. R. Nair, P. Blake, A. N. Grigorenko, K. S. Novoselov, T. J. Booth, T. Stauber, N. M. R. Peres, A. K. Geim, *Science* **320**, 1308 (2008)
5. K. S. Kim, Y. Zhao, H. Jang, S. Y. Lee, J. M. Kim, K. S. Kim, J. -H. Ahn, P. Kim, J.-Y. Choi, B. H. Hong, *Nature* **457**, 706 (2009)
6. X. S. Li, W. W. Cai, J. H. An, S. Kim, J. Nah, D. Yang, R. Piner, A. Velamakanni, I. Jung, E. Tutuc, S. K. Banerjee, L. Colombo, R. S. Ruoff, *Science* **324**, 1312 (2009)
7. S. Bae, H. Kim, Y. Lee, X. Xu, J.-S. Park, Y. Zheng, J. Balakrishnan, T. Lei, H. R. Kim, Y. I. Song, Y.-J. Kim, K. S. Kim, B. Ozyilmaz, J.-H. Ahn, B. H. Hong, S. Iijima, *Nat. Nanotech.* **5**, 574 (2010)
8. X. Li, Y. Zhu, W. Cai, M. Borysiak, B. Han, D. Chen, R. D. Piner, L. Colombo, R. S. Ruoff, *Nano Lett.* **9**, 4359 (2009)
9. A. Reina, X. Jia, J. Ho, D. Nezich, H. Son, V. Bulovic, M. S. Dresselhaus, J. Kong, *Nano Lett.* **9**, 30 (2008)
10. Z. Sun, Z. Yan, J. Yao, E. Beitler, Y. Zhu, J. M. Tour, *Nature* **468**, 549 (2012)
11. A. Ismach, C. Druzgalski, S. Penwell, A. Schwartzberg, M. Zheng, A. Javey, J. Bokor, Y. Zhang, *Nano Lett.* **10**, 1542 (2012)

12. H. Marsh, A. P. Warburton, *J. Appl. Chem.* **20**, 133 (1970)
13. R. Lamber, N. Jaeger, G. Schulz-Ekloff, *Surf. Sci.* **197**, 402 (1988)
14. A. G. Ramirez, T. Itoh, R. Sinclair, *J. Appl. Phys.* **85**, 1508 (1999)
15. M. Zheng, K. Takei, B. Hsia, H. Fang, X. Zhang, N. Ferralis, H. Ko, Y. L. Chueh, Y. Zhang, R. Maboudian, A. Javey, *Appl. Phys. Lett.* **96**, 063110 (2010)
16. N. Liu, L. Fu, B. Dai, K. Yan, X. Liu, R. Zhao, Y. Zhang, Z. Liu, *Nano Lett.* **11**, 297 (2010)
17. X. Liu, L. Fu, N. Liu, T. Gao, Y. Zhang, L. Liao, Z. Liu, *J. Phys. Chem. C* **115**, 11976 (2011)
18. Z. Li, P. Wu, C. Wang, X. Fan, W. Zhang, X. Zhai, C. Zeng, Z. Li, J. Yang, J. Hou, *ACS Nano* **5**, 3385 (2011)
19. B. S. Berry, *J. Appl. Phys.* **44**, 3792 (1973)
20. L. Vitos, A. V. Ruban, H. L. Skriver, J. Kollár, *Surf. Sci.* **411**, 186 (1998)
21. L. G. Cancado, K. Takai, T. Enoki, M. Endo, Y. A. Kim, H. Mizusaki, A. Jorio, L. N. Coelho, R. Magalhaes-Paniago, M. A. Pimenta, *Appl. Phys. Lett.* **88**, 163106 (2006)
22. T. Stefan, R. Alfonso, H. Paul, K. Jakub, W. Peter, H. Pei-Lan, K. Craig, S. Juergen, K. Jing, *Nanotechnology* **21**, 015601 (2010)
23. S. Yoshii, K. Nozawa, K. Toyoda, N. Matsukawa, A. Odagawa, A. Tsujimura, *Nano Lett.* **11**, 2628 (2011)

## CHAPTER 4.

# **Direct graphene growth: Graphene formation by direct carbon source feeding on Si substrate**

This chapter is based on the article published in  
*Current Applied Physics* **12**, 1088 (2012).



## 4.1. Introduction

Graphene is a single atomic layer consisting of hexagonal array of  $sp^2$  bonded carbon atoms. Since its discovery,<sup>1</sup> research interest for graphene has drastically increased due to its outstanding electrical,<sup>1-3</sup> optical,<sup>4</sup> thermal,<sup>5</sup> and mechanical<sup>6</sup> properties. Graphene can be formed by top-down approaches such as liquid exfoliation,<sup>7</sup> or by bottom-up approaches such as chemical vapor deposition (CVD)<sup>8,9</sup> on metal substrate, and epitaxial growth on silicon carbide (SiC) substrate.<sup>10</sup> In the epitaxy on silicon carbide substrate, SiC becomes a template for graphene growth with Si atoms selectively sublimating, thereby making high quality graphene growth possible. Direct fabrication of graphene devices can be realized with a SiC substrate<sup>11</sup> due to the wide energy gap of SiC (3.05 eV for 6H-SiC), contrary to the graphene formed on a metal substrate in the CVD process.

Many polytypes of SiC (6H-,<sup>12</sup> 4H-,<sup>13</sup> 3C-SiC<sup>14</sup>) have been used for graphene growth. However, high cost of SiC substrate is a major hindrance to practical application of graphene on SiC. To overcome this problem, a well-established method of growing SiC on Si substrate has been utilized,<sup>14-16</sup> in which SiC is grown by chemical vapor deposition (CVD) on silicon with carbon and silicon gas sources and then the resulting structure is subjected to vacuum sublimation, thereby leading to the formation of graphene (graphene/3C-SiC/Si). Whatever technique is used, however, vacuum sublimation is involved. The sublimation temperature is quite high ( $\sim 1400$  °C), which in turn causes defects in silicon substrate.

In this chapter, direct graphene formation on Si substrate by simply heating the substrate in the presence of a carbon source gas will be covered. The carbon in the

gas carburizes the surface of silicon substrate, which results in the formation of a SiC structure (3C-SiC). The growth of the SiC layer is self-regulated due to the limitation of Si out-diffusion and carbon in-diffusion at a given temperature<sup>18</sup>, and therefore, graphene starts forming on the grown SiC (3C-SiC/Si) with the carbon supplied from the gas phase. Graphene deposition on hexagonal SiC surface has already been demonstrated<sup>17</sup>, which does not require as high a temperature as in the traditional SiC growth because it does not involve sublimation of Si atoms. The key concept in this work is that graphene can be grown directly on SiC substrate, which is made possible by forming a 3C-SiC film on Si substrate by carburizing<sup>18</sup> Si substrate *in situ* prior to growing graphene.

The lattice match between 3C-SiC and the orientation of the underlying Si surface would have a significant effect on the growth of graphene. Therefore, various Si surface orientations ((100), (110), (111)) were used in this study to optimize 3C-SiC/Si interface and to subsequently investigate graphene/3C-SiC interface. The thickness of 3C-SiC is self-regulated due to diffusion limitation of silicon and carbon atoms at a given temperature.<sup>18</sup> The 3C-SiC formed on Si substrate here is not used as a platform that is self-converted to graphene but rather as a host structure for graphene to grow on it. The attractive feature of the proposed method is its conciseness and simplicity.

	<i>Pros.</i>	<i>Cons.</i>
SiC epitaxial growth	Graphene on SiC (wide gap) High quality	High process temperature Costly SiC wafer
SiC CVD and sublimation	Costly SiC substrate is replaced	Defective on Si substrate
Direct deposition of graphene on SiC	Lower temperature	Also, SiC substrate is required

**Table 4-1.** Advantages and disadvantages of SiC epitaxial growth of graphene, CVD growth of SiC and followed sublimation, and direct deposition of graphene on SiC substrate.

## 4.2. Experimental details

The formation of graphene via carburization process is illustrated in Figure 4-1. Si wafers were loaded in a quartz type rapid thermal annealing chamber after dipping into diluted hydrofluoric (HF) acid (diluted 10:1 in water) solution for 5 minutes without rinsing to avoid native oxide formation. The chamber was evacuated to ~1 mTorr, and only C<sub>2</sub>H<sub>4</sub> gas was introduced. Process pressure was 5 Torr and temperature was raised to 1100 °C by halogen lamp heating (heating rate was 80 °C/second such that the temperature was reached in 15 seconds). After just 1 minute of annealing, a few-layer graphene was formed on top of 3C-SiC (111) / Si (110). As discussed earlier, 3C-SiC forms on Si substrate first, followed by graphene growth on the 3C-SiC. Formation of SiC structure was confirmed by Fourier transform Infrared spectroscopy (FT-IR, Nicolet 6700, Thermo Scientific), and graphene layers were observed by Raman (Horiba Jobin Yvon, LabRam) spectroscopy. Microstructure (inter-plane relationship) of the samples were investigated by high-resolution Transmission electron microscopy (TEM; JEOL 3000F) and X-ray photoelectron spectroscopy (XPS; AXIS-His, KRATOS) was used for the carbon phase analysis.

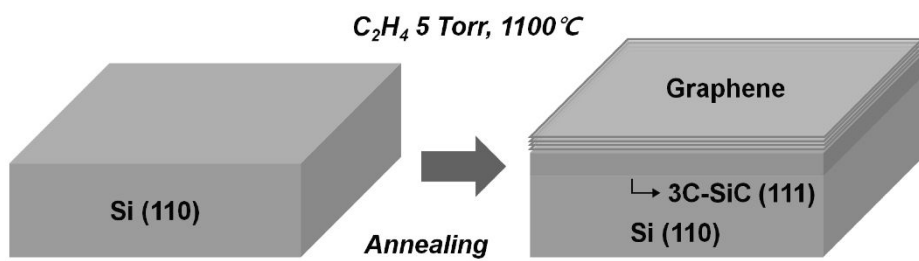


**Figure 4-1.** Schematics showing graphene formation on SiC/Si substrate by direct carbon feeding.

### 4.3. Results and Discussion

Spectroscopic studies were carried out to investigate the formation of SiC on Si surface and that of graphene on the SiC. FT-IR absorbance is shown in Figure 4-2 (a). It is quite surprising that we observed chemisorbed hydrocarbon molecules at 1000 °C, Si-CH<sub>2</sub> bond forms with the breaking of carbon to carbon bonding as indicated by the peak at ~1080 cm<sup>-1</sup>.<sup>19</sup> At higher temperatures, Si-C bond is seen to form as confirmed by the peak at ~790 cm<sup>-1</sup>.<sup>20</sup> IR absorption gradually increases with increasing annealing temperature, indicating a thicker SiC formation. We couldn't observe SiC formation at a certain condition such as high partial pressure of hydrocarbon source, which is from amorphous carbon (a-C) deposition. We believe that this is due to overfeeding of carbon source gas, in which carbon atoms cannot form SiC structure because carbon monomer flux is too high compared to surface reaction rate for SiC formation. We found out the formation of relatively thick a-C (depending on pressure and temperature) by HR-TEM analysis, so adequate partial pressure of carbon source is critical in this process.

Shown in Figure 4-2 (b) are Raman spectra of the graphene grown on 3C-SiC formed on Si. Prominent in the spectra are D (~1350 cm<sup>-1</sup>) and G (~1580 cm<sup>-1</sup>) peaks.<sup>21</sup> However, 2D (~2650 cm<sup>-1</sup>) peak was rarely detected, indicating the formation of low quality graphene due to pit formation in the Si substrate as shown in the low magnification TEM images in Figure 4-2(c). The peak at around 990 cm<sup>-1</sup> is the 2nd order peak of Si substrate. Comparison between Raman spectra of bare Si substrate and those of graphene grown on 3C-SiC in Figure 4-2 (b) clearly indicate that graphene was formed on Si substrate. Graphene growth is possible

since 3C-SiC formation is limited due to diffusion limitation of silicon and carbon through the SiC. The 3C-SiC layer was only several nanometers thick. Once this thin self-limited film of 3C-SiC forms, the subsequent carbon from the source gas appears to deposit on the hexagonal arrays of 3C-SiC that acts as a template for graphene growth. High-resolution TEM study in Figure 4-3 (a) revealed that a few-layer graphene (<10 layers) was grown on top of 3C-SiC (111) layer. We confirmed that the spacing between graphene layers is  $\sim 0.34$  nm. Figure 4-3 (a) also shows that a 3~4 nm-thick 3C-SiC layer was grown with inter-layer-distance of 0.25nm. It is certain that graphene layers are on top of 3C-SiC (111) plane judging from the high-resolution cross-sectional TEM image and its fast Fourier transform (FFT) image. The FFT image shows clearly parallel plane directions of graphene layers / 3C-SiC (111) / Si (110). We believe that the 3C-SiC (111) plane acts as a template for graphene growth since the hexagonal lattice plane is known to be a template for graphene growth according to a previous study.<sup>18</sup> We also studied carburizing behavior of Si (100) and (111) surfaces (Figure 4-3 (b) and (c)). The 3C-SiC planes grown on top of Si (100) and (111) surfaces show same orientation with underlying Si substrate, i.e., 3C-SiC (100)/Si(100) and 3C-SiC(111)/Si(111). The Si (111) substrate can also be a template for graphene growth since 3C-SiC (111) film can be grown, but the lattice misfit between Si and SiC is too large and consequently the mismatch degraded the quality of SiC. In almost all of the area in Si (111), the TEM images and FFTs show epitaxial relationship between 3C-SiC and Si, but graphene formation was rarely detected. The interface relationships between 3C-SiC and various orientations of Si surfaces are given in Table 4-2.

Since the structure of Si is diamond cubic, it is natural that cubic 3C-SiC should form when its surface is carburized. A surprising point here, however, is that

3C-SiC (111) plane can be grown on top of Si (110) plane. A similar result has already been reported in the case of CVD growth.<sup>22</sup> Carburization is not a deposition process of a new phase, but rather involves consumption of Si atoms by carbon that diffuses into a certain depth in forming SiC. In this way, the same crystal structure is assured between 3C-SiC and Si. The formation of 3C-SiC (111) on Si (110) may have something to do with epitaxial relationship between the two planes. Possible interface relationship is shown in Figure 4-4. Although a further study on interfacial relationship would be helpful between graphene/3C-SiC layers, HR-TEM and the corresponding FFT images show that 3C-SiC (111) planes was grown successfully on Si (110) plane. Only 2% lattice mismatch exists between the two planes even though each miller index orientation of plane is different. Consequently, hexagonal 3C-SiC (111) can serve as a template for graphene growth. We also observed C 1s spectrum for graphene layers formed carburization (1100 °C on (110) Si) using XPS for further investigation of carbon phase as shown in Figure 4-5. Two prominent peaks were detected at binding energy (B. E.) of 284.5 and 285.1 eV. Even after sputtering (~ 1 nm) the surface, no difference was found which means that hydrocarbon adsorption effect at the surface was negligible. Graphene layers shows distinctive  $sp^2$  bonding status (meaning graphitic phase similar to previous report) at 284.5 eV,<sup>23</sup> but also gives defective structure as confirmed by  $sp^3$ -like chemical shift at 285.1 eV (with relatively weak intensity).<sup>24</sup> The sum of two peaks well matched to measured spectrum. Full width at half maximum (FWHM) value of each peak ( $sp^2$  and  $sp^3$ ) was 1.49 and 2.64 eV, respectively. Our graphene shows  $sp^2$  bonding characteristics, but contains defects which induce broad  $sp^3$  spectrum. On the other hand, SiC bonding was not detectable in C 1s spectrum which might be from weak signal limited by escape

depth of photoelectron. Si 2p spectrum intensity was about 10 times lower than C 1s peak at the surface.

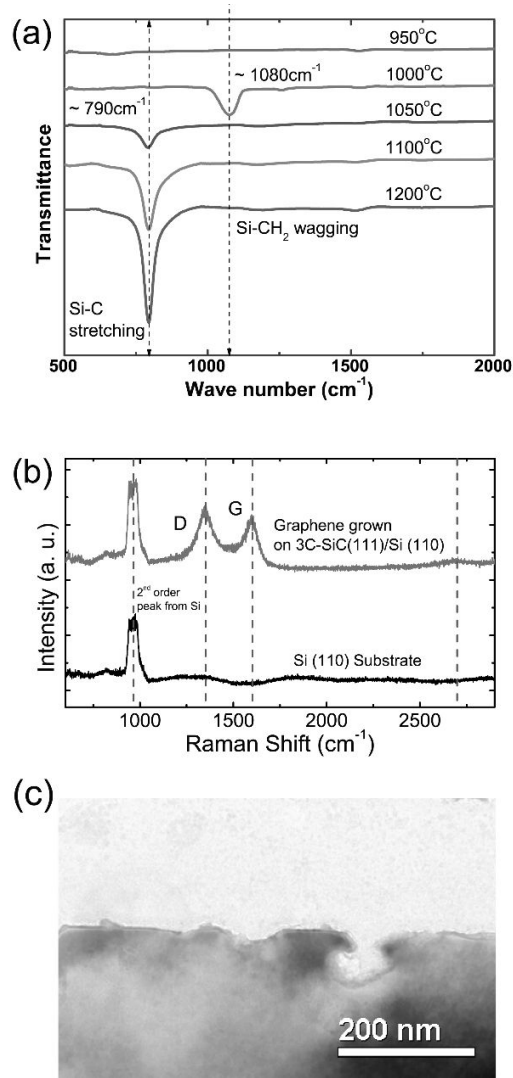


**Figure 4-2.** (a) FT-IR spectra of the carburized (110) Si substrate as a function of annealing temperature, and (b) Raman spectra of the as-prepared Si substrate and graphene/3C-SiC(111)/Si(110) after 1,100 °C annealing for 1minute. Incident wavelength of laser was 532nm. Spectral resolution was 1.47  $\text{cm}^{-1}$  and (c) Low magnification cross-sectional TEM image of graphene / 3C-SiC (111) / Si (110) structure.

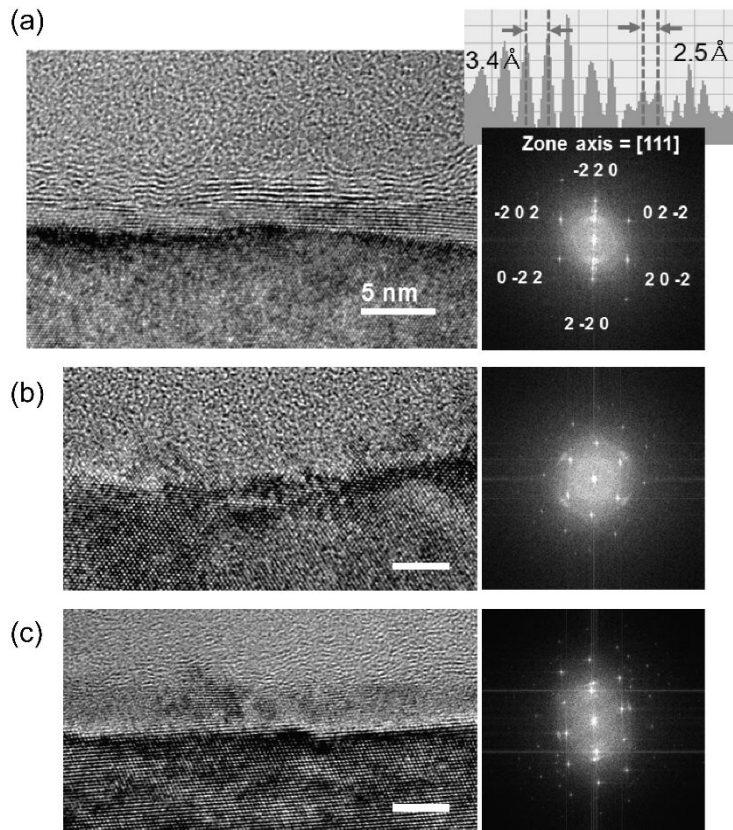


**Figure 4-3.** (a) High resolution TEM image of graphene / 3C-SiC (111) / Si (110) structure, line profile indicating inter-layer distance, and FFT image from Si [111] zone axis, (b) high resolution TEM image of 3C-SiC (100) / Si (100) structure after carbon feeding, and FFT image (zone axis of Si is [110]), and (c) high resolution TEM image of 3C-SiC (111) / Si (111) structure after carbon feeding ,and FFT image (zone axis of Si is [110]). All the scale bars indicate 5 nm.

Si Substrate	(100)	(110)	(111)
3C-SiC	(100)	(111)	(111)
Lattice misfit	20%	2%	20%

**Table 4-2.** Relative orientation of Si surface and 3C-SiC planes formed by carburization process

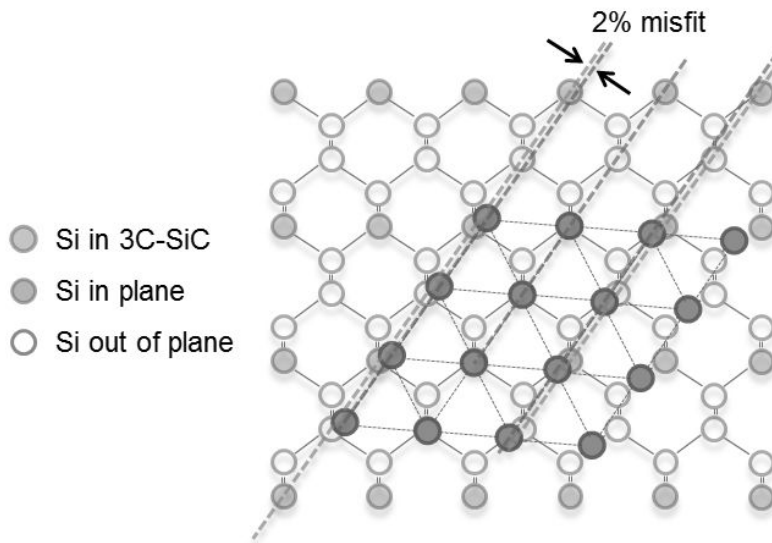


**Figure 4-4.** Expected interface crystallographic orientations of 3C-SiC(111) / Si(110), which causes only a 2% lattice misfit by finding well-matching epitaxial plane. Carbon atoms in 3C-SiC is omitted for simple visualization.

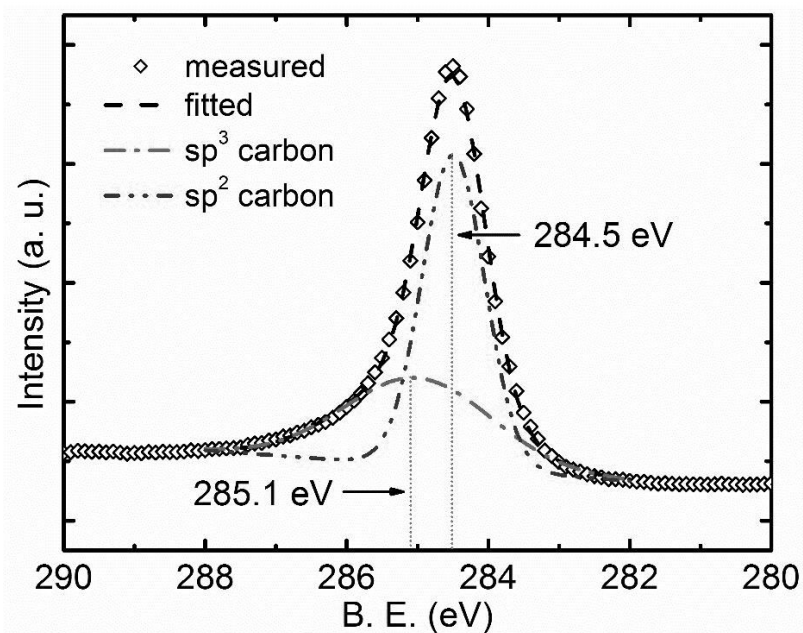


**Figure 4-5.** XPS C 1s signal from graphene layers formed by carburization of (110) Si substrate at 1,100 °C. X-ray source is from Mg  $K_{\alpha}$ .

#### **4.4. Summary and Conclusions**

In conclusion, direct graphene deposition was demonstrated on 3C-SiC/Si using carburization of Si. We found that graphene/3C-SiC was formed in-situ by direct carbon source deposition. Neither high vacuum nor high temperature is needed. High cost SiC substrate is replaced by Si, and no hazardous Si gas source is required for forming SiC layer. This method can be used for forming graphene on insulator structure with SOI (silicon on insulator) wafer. The process needs to be optimized for better quality since out-diffusion of Si atoms makes SiC defective, subsequently degrading graphene's quality. In this study, the desirable surface was found to be Si (110), which leads to the formation of 3C-SiC (111) that can act as a hexagonal template for graphene growth. The lattice mismatch between 3C-SiC (111) and Si (110) is less than 2%.

## References

1. K. S. Novoselov, A. K. Geim, S. V. Morozov, D. Jiang, Y. Zhang, S. V. Dubonos, I. V. Grigorieva and A. A. Firsov, *Science* **306**, 666 (2004)
2. K. S. Novoselov, A. K. Geim, S. V. Morozov, D. Jiang, M. I. Katsnelson, I. V. Grigorieva, S. V. Dubonos and A. A. Firsov, *Nature* **438**, 197 (2005)
3. K. I. Bolotin, K. J. Sikes, J. Hone, H. L. Stormer and P. Kim, *Phys. Rev. Lett.*, **101**, 096802 (2008)
4. R. R. Nair, P. Blake, A. N. Grigorenko, K. S. Novoselov, T. J. Booth, T. Stauber, N. M. R. Peres and A. K. Geim, *Science* **320**, 1308 (2008)
5. A. A. Balandin, S. Ghosh, W. Bao, I. Calizo, D. Teweldebrhan, F. Miao and C. N. Lau, *Nano Letters* **8**, 902 (2008)
6. C. Lee, X. Wei, J. W. Kysar and J. Hone, *Science* **321** (2008) 385.
7. S. Park and R. S. Ruoff, *Nat Nanotech.* **4**, 217 (2009)
8. K. S. Kim, Y. Zhao, H. Jang, S. Y. Lee, J. M. Kim, K. S. Kim, J.-H. Ahn, P. Kim, J.-Y. Choi and B. H. Hong, *Nature* **457**, 706 (2009)
9. X. S. Li, W. W. Cai, J. H. An, S. Kim, J. Nah, D. X. Yang, R. Piner, A. Velamakanni, I. Jung, E. Tutuc, S. K. Banerjee, L. Colombo and R. S. Ruoff, *Science* **324**, 1312 (2009)
10. W. A. de Heer, C. Berger, X. S. Wu, P. N. First, E. H. Conrad, X. B. Li, T. B. Li, M. Sprinkle, J. Hass, M. L. Sadowski, M. Potemski and G. Martinez, *Solid State Commun.* **143**, 92 (2007)
11. SprinkleM, RuanM, HuY, HankinsonJ, M. Rubio Roy, ZhangB, WuX, BergerC and W. A. de Heer, *Nat Nanotech.* **5**, 727 (2010)
12. K. V. Emtsev, A. Bostwick, K. Horn, J. Jobst, G. L. Kellogg, L. Ley, J. L.

- McChesney, T. Ohta, S. A. Reshanov, J. Rohrl, E. Rotenberg, A. K. Schmid, D. Waldmann, H. B. Weber and T. Seyller, *Nat Mater.* **8**, 203 (2009)
13. C. Berger, Z. M. Song, X. B. Li, X. S. Wu, N. Brown, C. Naud, D. Mayo, T. B. Li, J. Hass, A. N. Marchenkov, E. H. Conrad, P. N. First and W. A. de Heer, *Science* **312**, 1191 (2006)
14. V. Y. Aristov, G. Urbanik, K. Kummer, D. V. Vyalikh, O. V. Molodtsova, A. B. Preobrajenski, A. A. Zakharov, C. Hess, T. Hänke, B. Büchner, I. Vobornik, J. Fujii, 15. G. Panaccione, Y. A. Ossipyan and M. Knupfer, *Nano Letters* **10**, 992 (2010)
16. K. Kuroiwa and T. Sugano, *J. Electrochem. Soc.* **120**, 138 (1973)
17. A. J. Steckl and J. P. Li, *Electron Devices, IEEE Transactions on* **39**, 64 (1992)
- A. Michon, S. Vezian, A. Ouerghi, M. Zielinski, T. Chassagne and M. Portail, *Appl. Phys. Lett.* **97**, 171909 (2010)
18. A. Addamiano and J. A. Sprague, *Appl. Phys. Lett.* **44**, 525 (1984)
19. V. N. Khabashesku, K. N. Kudin and J. L. Margrave, *J. Mol. Struct.* **443**, 175 (1998)
20. H. Hobert, H. H. Dunken, J. Meinschien and H. Stafast, *Vibrational Spectroscopy* **19**, 205 (1999)
21. A. C. Ferrari, J. C. Meyer, V. Scardaci, C. Casiraghi, M. Lazzeri, F. Mauri, S. Piscanec, D. Jiang, K. S. Novoselov, S. Roth and A. K. Geim, *Phys. Rev. Lett.* **97**, 187401 (2006)
22. M. Suemitsu, Y. Miyamoto, H. Handa and A. Konno, *e-Journal of Surface Science and Nanotechnology* **7**, 311 (2009)
23. E. Rollings, G.-H. Gweon, S. Y. Zhou, B. S. Mun, J. L. McChesney, B. S. Hussain, A. V. Fedorov, p. N. First, W. A. de Heer, and A. Lanzara, *J. Phys. Chem.*

Solids **67**, 2172 (2006)

24. J. Zemek, J. Houdkova, B. Lesiak, A. Jablonski, J. Potmesil and M. Vanecek, J.

Optoelectron Adv. M. 8 2133 (2006)

## CHAPTER 5.

### **Gas transport control in graphene growth: Micro-meter scale gap jig effect**

This chapter is based on the article published in  
*RSC Advances* **3**, 26376 (2013).



## 5.1. Introduction

The introduction of graphene as a novel two-dimensional material with unique electrical,<sup>1-3</sup> optical,<sup>4</sup> and mechanical<sup>5</sup> properties and, moreover, the introduction of successful growth method for predominantly single-layer and bilayer graphene using Cu as a catalytic metal<sup>6-8</sup> have attracted great interest worldwide. The growth mechanism of graphene on a Cu substrate seems relatively simple, being based on the catalytic effect of Cu in dissociating the hydrocarbon source molecules; the limited solubility of carbon in Cu, which makes the overall reaction only bounded by the Cu surface; and the rapid migration of carbon adatoms on the Cu substrate, which eventually leads to the formation of two-dimensional nuclei and the growth of a single layer of graphene.<sup>6</sup> Owing to the simplicity of this process, the growth of graphene has become a routine procedure, although the transfer of the graphene layer can be somewhat complicated.<sup>9, 10</sup>

Although the overall process for creating graphene is relatively simple, obtaining high-quality graphene is another issue. It has been well documented that the quality of chemical vapour deposition (CVD)-derived graphene layers is inferior to that of graphene layers exfoliated from pyrolytic graphite.<sup>11-13</sup> These results indicate that CVD-grown graphene layers contain a high density of defect sites, most notably, a high density of grain (or domain) boundaries. To obtain high-quality graphene layers, the grain size should be as large as possible and the grain should be grown with a well-bounded morphology (hexagonal edge shape) instead of a flower-like dendritic morphology. To achieve these goals, the nucleation and growth kinetics should be well understood and controlled.

Many studies have attempted to grow high-quality graphene layer using CVD, which including studies on the role of CH<sub>4</sub> flow rate,<sup>7</sup> hydrogen flow,<sup>14,15</sup> temperature,<sup>16</sup> and Cu surface treatment.<sup>17-19</sup> However, our understanding of graphene growth remains quite limited. Most of these limitations are due to not only the limited understanding of the thermodynamic and kinetic parameters of graphene growth<sup>20,21</sup> but also the interrelated nature of these parameters. Recently, large graphene domains have been grown using low-pressure CVD with a piece of folded Cu foil used to reduce the CH<sub>4</sub> flow.<sup>8,22</sup> This result indicates that the flow of the source gas is an important parameter in the growth of high-quality graphene. However, the mechanism of graphene growth is not well understood.

In this chapter, we systematically investigate the effect of gas transport on graphene growth. To control the gas transport, we employed a specially designed jig with a gap, in which the gap spacing between the upper lid and lower plate can be adjusted between 100 μm and several mm. Because of friction force near the jig wall, the boundary layer is believed to fully develop throughout the interior of the jig. Thus, when the gas stream flows through the gap, molecular diffusion through the boundary layer determines the total gas flux, namely, the conductance. Because the conductance can be tuned by changing the gap spacing, we expect to be able to study the growth behaviour inside the jig as a function of lateral distance at various conductance levels.

## 5.2. Experimental details

Graphene was grown by low-pressure chemical vapor deposition (LPCVD) using a micrometer-gap spacing jig inside the quartz tube furnace (Figure 5-1 (a)). The micrometer-gap jig was specially made of alumina powder sintered ceramic, including all nails shown in Figure 5-1 (b) and (c). The jig gap spacing ( $D_j$ ) was measured by Vernier calipers before loading the Cu foil and confirmed by a thickness gauge (the target thickness plate was inserted prior to loading the sample). As shown in Figure 5-1 (b), the upper lid of the jig was deliberately made smaller than that of the lower plate to compare the growth behavior from the jig exterior to the jig interior. The  $\text{CH}_4$  flux was varied from 0.5 to 4 sccm, and the  $\text{H}_2$  flux was 12 sccm. For the diluted source gas supply, Ar was used as a carrier gas for certain experiments. Unless otherwise noted, the  $\text{CH}_4$  and  $\text{H}_2$  fluxes were 0.5 and 12 sccm, respectively, and the growth temperature was  $1035^\circ\text{C}$  at a 200-mTorr working pressure. Before the graphene growth, the Cu was pre-annealed for 1 h at the same temperature as the growth to remove native oxide and enhance the Cu grain growth. After the growth, the Cu foil was cooled under the same gas environment. The graphene layer was transferred to a 285-nm- $\text{SiO}_2/\text{Si}$  substrate by a polymer coating technique.<sup>7</sup> The graphene on the Cu foil was observed by scanning electron microscopy (SU-70, Hitachi) with an acceleration voltage of 5 kV. Raman spectra and mapping (see Fig. S1 in the supporting information) were carried out after the transfer by a UniRam system with a Princeton CCD (charge-coupled device) detector (PIXISL: 100B). A DPSS (diode-pumped solid state) laser (100 mW, 532 nm) was used for input for the X100 objective lens. The step resolution for the

Raman spectroscopy was 1  $\mu\text{m}$ . Image analysis was carried out using Image Pro 4.5 software on  $1280 \times 896$  pixel SEM images.

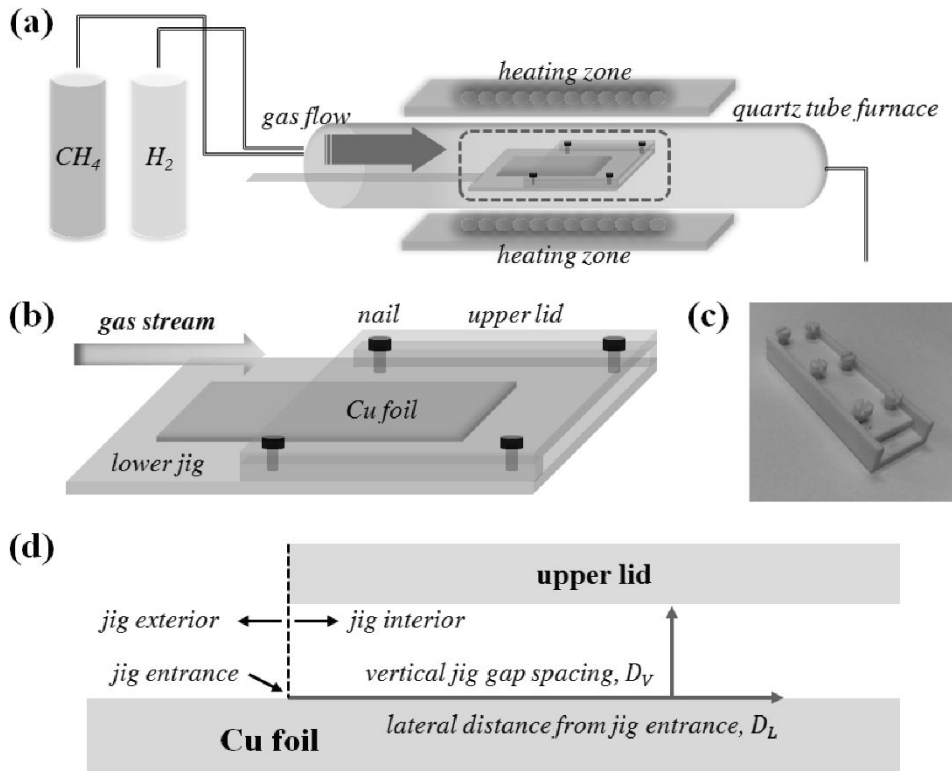


**Figure 5-1.** Vacuum-tube based CVD system using a micrometer-gap jig: (a) overall depiction of the furnace system; (b) illustration of the micrometer-gap jig, nails, and Cu foils; (c) photograph of the jig, which is made of sintered alumina, including all nails; and (d) illustration of the horizontal and vertical axis system in the jig gap discussed in this experiment.

### 5.3. Results and Discussion

The purpose of using a micrometer-scale gap jig in this experiment is to control the gas transport inside the jig by forming a fully developed boundary layer. Because the gas velocity at the wall surface is considered to be zero due to friction, the boundary layer begins to develop at the jig entrance, and gas molecules can only travel to the Cu surface by molecular diffusion. The boundary layer thickness ( $\delta(x)$ ) increases parabolically as a function of lateral distance  $x$ , as described below.<sup>23,24</sup>

$$\delta(x) = \left( \frac{\nu x}{U} \right)^{\frac{1}{2}} \quad \dots 5-(1)$$

Here,  $\nu$  is the kinematic viscosity of the gas stream,  $U$  is the gas flow velocity, and  $x$  is the lateral distance. When the gas flow rate of CH<sub>4</sub> is 10 sccm at constant pressure, the stream velocity of CH<sub>4</sub> in a 6-cm-diameter tube furnace is  $5.9 \times 10^{-5}$  m/s (lowest speed under the no-leak assumption). Because the kinematic viscosity of CH<sub>4</sub> is known to be  $1.7 \times 10^{-5}$  m<sup>2</sup>/s,<sup>25</sup> the boundary layer thickness can be expressed as

$$\delta(x) = \sqrt{0.28x} \quad \dots 5-(2)$$

Thus, according to equation 5-(2), stagnant boundary layer thickness corresponds to 16.7 mm ( $\delta$ ) when the gas penetrates 1 mm ( $x = 1$  mm) inside the jig. Although this calculation provides a crude approximation, we believe that the full development of the boundary layer at the jig entrance does occur, as  $D_V$  is less than 1 mm.

### 5.3.1. Jig effect on pre-annealing

The effect of the jig is first observed during pre-annealing, before graphene growth. A photograph of the Cu surface immediately after pre-annealing is shown in Figure 5-2. The image clearly shows that the Cu surface located in the jig interior (i.e., the jig-protected region) becomes optically distinguishable from the jig exterior (the region exposed to the gas stream). The effect of the jig is more clearly shown in Figure 5-2 (b), which shows an optical microscopy image of the interface between the jig exterior and jig interior. The Cu surface was heavily damaged during the pre-annealing at the jig exterior. However, the jig interior image on the right side of Figure 5-2 (b) shows a much smoother Cu surface. The magnified images presented in Figure 5-2 (c) (jig exterior) and (d) (jig interior) clearly depict this difference.

Pre-annealing is necessary for removing organic particles and native oxide and smoothing the Cu surface for graphene growth.<sup>17,26</sup> According to previous reports,<sup>27</sup> Cu sublimates during pre-annealing in the LPCVD growth of graphene, resulting in the evolution of a rough surface. It is known that the equilibrium vapor pressure of Cu is approximately  $10^{-4}$  Torr at 1050 °C.<sup>28</sup> Thus, the sublimation and re-deposition of Cu cannot be ignored in LPCVD due to the continuous sublimation and evacuation of Cu vapor. Apparently, inside of the jig, sublimed Cu vapor experiences longer residence times due to the relatively static gas flow. Thus, the overall sublimation rate of Cu appears to be retarded. This result is not expected but certainly proves that the jig is effective in reducing the damage of the Cu surface during pre-annealing. A similar result has been reported recently by L. Tao *et al.*, who placed a quartz plate above a Cu foil to reduce the sublimation of Cu during pre-annealing.<sup>29</sup>



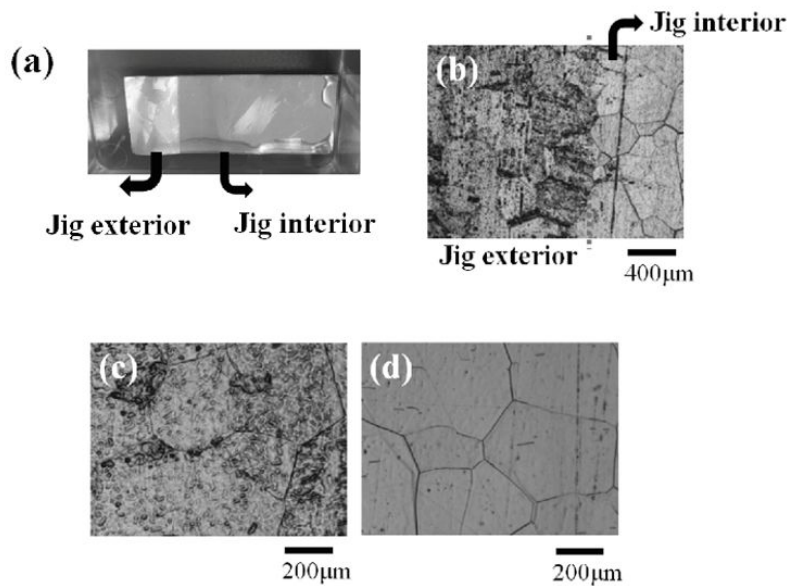


**Figure 5-2.** (a) Photograph of Cu foil after pre-annealing using the micrometer-gap jig, showing clear evidence of the surface protection effect; (b) optical microscopy (OM) image of the Cu foil near the jig entrance; (c) magnified OM image of the jig exterior region (left section of (b)); and (d) magnified OM image of the jig interior region (right section of (b)). Pre-annealing: 1035 °C for 1 h.

### 5.3.2. Gas transport effect on graphene growth

To study the effect of gas conductance on graphene growth, we systematically varied  $D_V$  (gap spacing) from 1 mm to 100  $\mu\text{m}$  under  $\text{CH}_4$  and  $\text{H}_2$  flow rates of 0.5 and 12 sccm, respectively, at 1035  $^\circ\text{C}$ . The overall growth behavior is shown as a function of lateral distance ( $D_L$ ) and gap spacing ( $D_V$ ) in Figure 5-3. The areal coverage of the graphene clearly decreases as  $D_V$  decreases and  $D_L$  increases. Irrespective of coverage, the quality of the graphene is quite good, as determined by Raman spectroscopy (Figure 5-4). The effect of  $D_L$  clearly demonstrates that the source gas transport interior of the jig is limited by the decreasing gap spacing, which decreases the overall conductance of gas molecules. Moreover, the effect of  $D_V$  indicates that the source gas is heavily depleted by the reaction as the gas molecules are transported inside the gap. This trend becomes clearer as we decrease  $D_V$  to 100  $\mu\text{m}$ . At this gap spacing, an abrupt decrease of coverage occurs, even at the jig entrance. We have plotted the coverage of graphene as a function of  $D_L$  at each  $D_V$  in Figure 5-5 after image analysis (Figure 5-3). Again, the result shows that the coverage is gradually reduced from 100 % of coverage at the jig gap entrance to 30 % as  $D_L$  is increased to 20 mm. The reduction of coverage is more dramatic as  $D_V$  is decreased. For instance, 30 % graphene coverage occurs at  $D_L$  of 16, 8, 6, and 3 mm at each  $D_V$ . Thus, a wider jig gap provides a larger penetration depth for the source gas flow, and a narrower  $D_V$  leads to an abrupt change in coverage.

The graphene coverage in Fig. 5-5 (a) is directly related to the amount of carbon monomers decomposed on the Cu surface. In our experiment, we observed the graphene growth as a function of two dimensional parameters,  $D_V$  and  $D_L$ ,

which affect the source gas flux ( $\text{CH}_4$ ). We can consider the gas conductance to be proportional to the cross-sectional area of the gap and inversely proportional to the length of gap, which can be expressed as

$$C_{gas} = k \frac{A}{L} \quad \dots 5-(3)$$

where  $C_{gas}$  is the gas conductance through the gap structure,  $k$  is a constant,  $A$  is the cross-sectional area of the gap, and  $L$  is the length of the gap. In our structure, the cross-sectional area  $A$  is directly related to the height of the gap ( $D_V$ ), and the horizontal length of the jig ( $L$ ) is fixed. Thus, the overall gas conductance through the gap is directly proportional to  $D_V$ . However, to consider the surface coverage evolution, we also must consider the effect of source gas depletion by reaction. As is noted, the source gas is depleted by the reaction as the gas molecules are transported inside the gap. Because the graphene layer formation reaction can be considered proportional to the source gas concentration and source gas depletion occurs as the gas molecules are transported inside the gap spacing, we can consider the effective source gas conductance through the gap as follows:

$$C_{CH_4} = k' \frac{D_v}{D_L} \quad \dots 5-(4)$$

In this case, the carbon source flux expected at a given  $D_V$  and  $D_L$  is proportional to the effective source gas conductance at a given reaction time. Therefore,  $D_L/D_V$  directly represents the suppression of carbon source conductance. Consequently, we can plot the graphene coverage as a function of the inverse of the carbon source gas conductance, i.e.,  $D_L/D_V$ , as shown in Figure 5-5 (b). It is interesting to note that the graphene coverage lies on the same curve as  $D_L/D_V$  regardless of the gap spacing ( $D_V$ ). This result again confirms that  $D_L/D_V$  is a good parameter for

controlling the source gas flux to the Cu substrate as well as the overall graphene growth.

The coverage of graphene is the sum of nucleation and growth behavior. In this respect, we would like to determine how the gas transport affects the nucleation and growth behavior. Figure 5-6 shows the detailed analysis of the gap spacing effect for an average graphene grain size (Figure 5-6 (a)) and the density of nuclei (Figure 5-6 (b)) as a function of lateral distance ( $D_L$ ). The average grain size (total area/number of nuclei) of the graphene islands follows the same trend as the graphene coverage; namely, the average grain size is drastically decreased as  $D_V$  decreases and  $D_L$  increases. However, considering the decrease in the total coverage, the nucleation density of the islands (determined by the number of graphene grains) in Figure 5-6 (b) did not show any noticeable dependence on either  $D_L$  or  $D_V$ . These results indicate that the conductance of gas molecules or the flow rate of the source gas does not affect the nucleation behavior and that the decrease in the coverage results purely from the reduction of the average grain size of graphene. This finding also indicates that the nucleation rate is not directly related to the degree of supersaturation. As known from capillary theory, the nucleation rate is essentially proportional to the product of three terms, namely,

$$\dot{N} = N^* A^* w \quad \dots 5-(5)$$

where  $N^*$  is the equilibrium concentration of the critical nuclei and  $w$  is the rate at which adatoms impinge onto the nuclei of the critical area  $A^*$ . In this equation,  $N^*$  is expressed as<sup>30</sup>

$$N^* = n_s \exp\left(-\frac{\Delta G^*}{kT}\right) \quad \dots 5-(6)$$

where  $N^*$  represents an energy barrier to the nucleation process,  $n_s$  is the density of nucleation sites, and  $k$  is the Boltzmann constant. Here,  $\Delta G^*$  is a function of the degree of supersaturation, which should also be a function of the source gas supply. Our experimental results, however, show that the nuclei density is not a strong function of supersaturation, implying that  $n_s$  is more important for the nucleation of graphene.

Indeed, the graphene growth on Cu foil should be considered a case of heterogeneous nucleation. The equation mentioned above, although generally true, cannot be applied to the growth of graphene directly because the surface of Cu foil contains many heterogeneous nucleation sites. Depending on the detailed nature of these sites, both  $\Delta G^*$  and  $n_s$  should vary. Many reports have suggested the heterogeneous nucleation of graphene, such as on the edges of a scratch or other topological defects.<sup>18,19</sup> If heterogeneous nucleation is the dominant mechanism of graphene growth, the pre-treatment of Cu surface should be more important than the degree of supersaturation in controlling the nucleation rate. Recent work published by Z. Yan *et al.*<sup>17</sup> supports this argument, finding that careful surface pre-annealing to improve the Cu surface condition is critical to the growth of graphene with large grains.

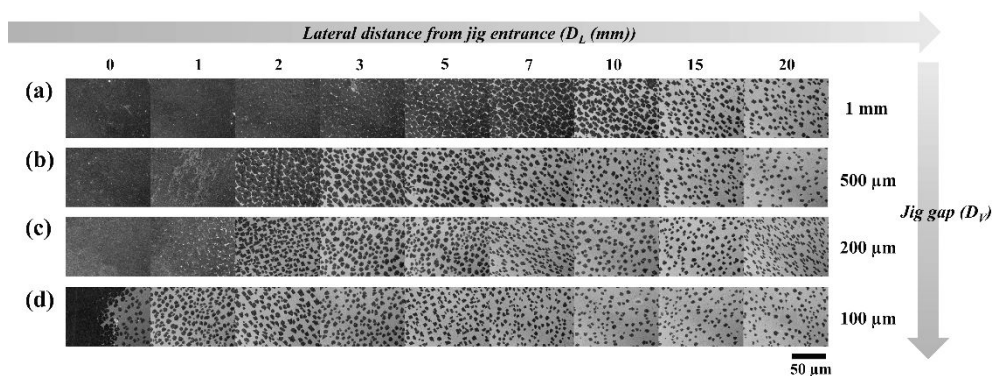


**Figure 5-3.** SEM images of graphene grown on Cu foil with varied micrometer-gap jigs. (a) SEM images of the Cu foil when the jig gap is 1 mm taken at different positions with respect to the jig entrance and at the lateral positions marked above. SEM images of the Cu foil when the jig gap is (b) 500  $\mu\text{m}$ , (c) 200  $\mu\text{m}$ , and (d) 100  $\mu\text{m}$ . Scale bar indicates 50  $\mu\text{m}$ .

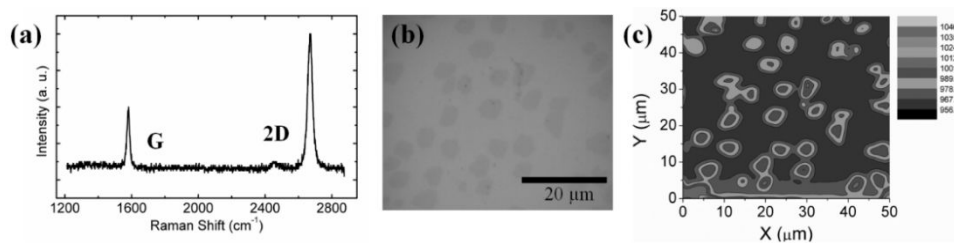


**Figure 5-4.** (a) Typical Raman spectrum of graphene fully grown on Cu foil after the transfer to a SiO<sub>2</sub> (285 nm)/Si substrate when the jig is applied after an extended growth time of 30 min. (b) Optical microscope image of graphene islands after transfer. (c) G-band micro-Raman mapping analysis over a 50 × 50 μm area with a step size of 1 μm for the area depicted in (b). A 532-nm DSSP laser and X100 objective lens were used.

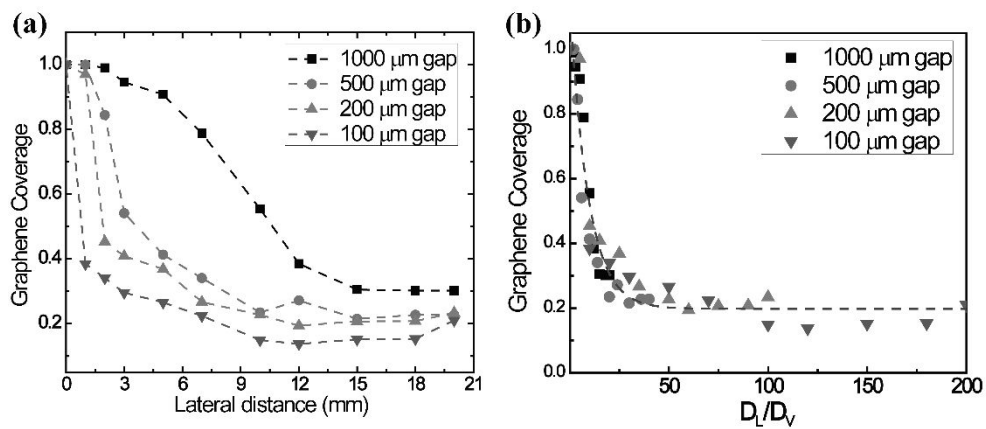


**Figure 5-5.** (a) Fraction of graphene-covered area in SEM images in Figure 5-3 as a function of lateral distance ( $D_L$ ) from the jig entrance when the jig gap ( $D_V$ ) varies from 1 mm to 100  $\mu\text{m}$  and (b) fraction of graphene covered area in the SEM images as a function of  $D_L/D_V$ .

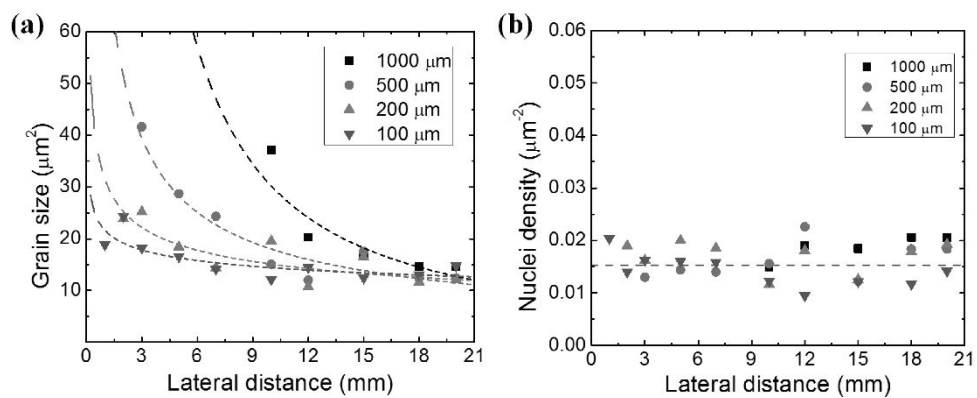


**Figure 5-6.** Average grain size of graphene islands as a function of lateral distance at each jig gap spacing and (b) nuclei density as a function of lateral distance ( $D_L$ ) at each jig gap spacing ( $D_j$ ).

### 5.3.3. Morphology evolution of graphene grains

Finally, the grain morphology varies strikingly depending on the position of the Cu foil, i.e., whether it is located inside or outside the jig. For instance, Figure 5-7 shows the results for a case in which the gas flows of CH<sub>4</sub>, H<sub>2</sub>, and Ar were 1, 5, and 16 sccm, respectively, and the jig gap was 300 μm. Interestingly, the grain morphology of the graphene grown outside the jig exhibits a large grain size with a dendritic morphology, whereas that inside the jig exhibits small grains with a well-bounded edge morphology (Figure 5-3). The change in the grain morphology in this case is quite drastic because of the low gas feeding rate. For a higher gas feeding rate, the evolution of the graphene morphology is gradual, as shown in Figure 5-8. It is generally known that dendritic shape growth occurs when the monomer supply rate to the growing graphene edge is faster than the edge-migration of monomers to lower the overall edge energy of graphene. During LPCVD growth, the supply rate of carbon monomers to the growing graphene edge by surface diffusion on Cu is faster (characterized by the fast growth rate) than the rate of edge migration. For instance, the activation energy of the surface diffusion of carbon monomers on the Cu substrate is approximately 0.7 to 0.06 eV, whereas that of the attachment of carbon monomers to the graphene edge is approximately 2 eV.<sup>21</sup> Therefore, to form a well-bounded edge morphology, the supply of carbon monomers to the growing graphene grains should be as low as possible. Our result clearly shows that this condition can be achieved by controlling the source gas flow using a micrometer-scale gap spacing. In addition, the grain morphology can also be controlled by the etching effect of H<sub>2</sub>. As is well known, the overall graphene growth process can be considered a combination of growth by the hydrocarbon

source gas ( $\text{CH}_4$ ) and graphene etching by hydrogen molecules ( $\text{H}_2$ ).<sup>14,15</sup> When the gas molecules flow inside the jig, the  $\text{CH}_4$  molecules are rapidly consumed by the reaction, while the  $\text{H}_2$  gas molecules are inert. Moreover, the dissociation of  $\text{CH}_4$  by the reaction also generates extra  $\text{H}_2$  gas molecules. Thus, the etch rate rapidly increases relative to the growth rate as we move inside the jig. Both of these phenomena act to form a grain morphology with a well-defined edge shape.

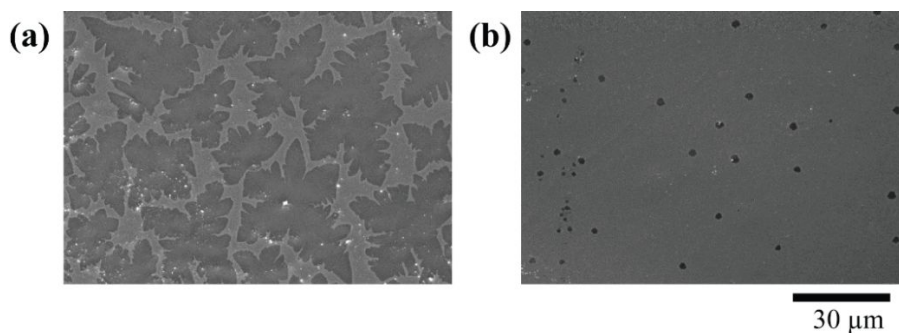


**Figure 5-7.** SEM images showing the gas source suppression effect when the jig is used for graphene growth. (a) SEM image of typical graphene islands grown outside the jig. (b) SEM image of graphene seeds grown inside the jig. The graphene islands and seeds in (a) and (b) were from the same foil and were subjected to the same growth conditions. (Graphene growth was carried out at 1035 °C for 3 min; CH<sub>4</sub>, H<sub>2</sub>, and Ar fluxes were 1, 5, and 16 sccm, respectively). The inset depicts the well-defined grain morphology of graphene grown in the jig interior under the same conditions as (b) with extended growth time.

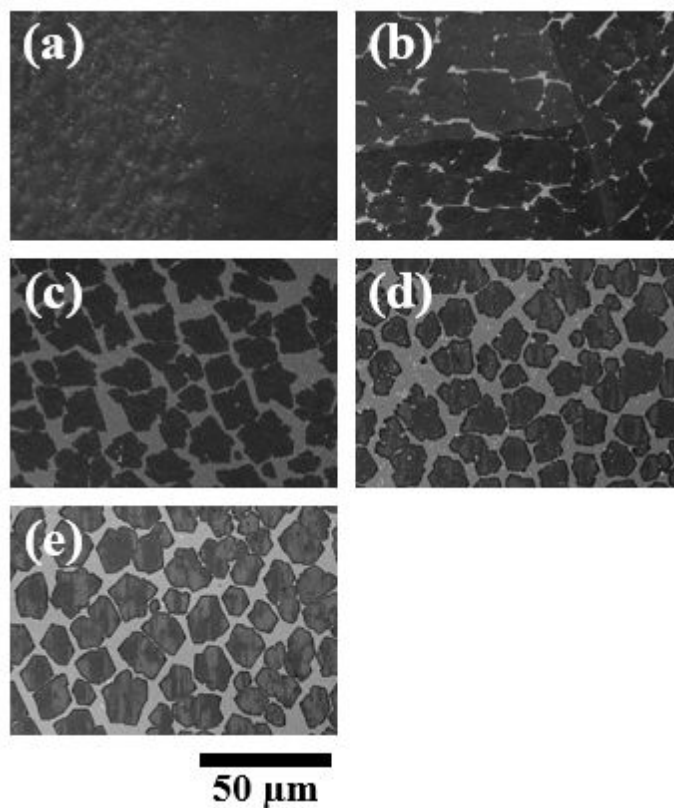


**Figure 5-8.** SEM images of graphene grown on Cu foil when a micrometer-gap jig is applied for gas transport control. SEM images of (a) the fully grown graphene film on the jig exterior, (b) 5 mm from the jig entrance, (c) 10 mm from the jig entrance, (d) 15 mm from the jig entrance, and (e) 20 mm from the jig entrance. CH<sub>4</sub> and H<sub>2</sub> flux: 2 sccm and 6 sccm, respectively. Scale bar indicates 50 μm.

## 5.4. Summary and Conclusions

A micrometer-gap jig was applied to graphene growth to manipulate gas transport and thus separately control the nucleation and growth rate. The Cu surface is protected from sublimation, even at high temperature and low pressure, due to the limited gas molecule transport inside the gap. A boundary layer develops along the gas flow from the jig entrance; thus, molecular transport dominates graphene growth. The suppression of the source gas transport and possible hydrogen etching lead to well-aligned polygonal graphene growth inside the jig. Gas transport was successfully controlled by the studied parameters, namely, lateral distance and vertical jig gap. Control over the source gas feeding rate by the application of the jig concept decreases the source gas decomposition followed by reduced graphene coverage, which is a consequence of the reduction in grain size, rather than nucleation density. This result indicates that inherent heterogeneous nucleation sites are more important in controlling the nucleation rate than the degree of supersaturation.

## References

1. K. S. Novoselov, D. Jiang, F. Schedin, T. J. Booth, V. V. Khotkevich, S. V. Morozov and A. K. Geim, Proc. Nat. Acad. Sci. **102**, 10451 (2005)
2. K. S. Novoselov, A. K. Geim, S. V. Morozov, D. Jiang, M. I. Katsnelson, I. V. Grigorieva, S. V. Dubonos and A. A. Firsov, Nature **438**, 197 (2005)
3. K. S. Novoselov, A. K. Geim, S. V. Morozov, D. Jiang, Y. Zhang, S. V. Dubonos, I. V. Grigorieva and A. A. Firsov, Science **306**, 666. (2004)
4. R. R. Nair, P. Blake, A. N. Grigorenko, K. S. Novoselov, T. J. Booth, T. Stauber, N. M. R. Peres and A. K. Geim, Science **320**, 1308 (2008)
5. X. Liu, T. H. Metcalf, J. T. Robinson, B. H. Houston and F. Scarpa, Nano Lett., **12**, 1013 (2012)
6. X. S. Li, W. W. Cai, J. H. An, S. Kim, J. Nah, D. X. Yang, R. Piner, A. Velamakanni, I. Jung, E. Tutuc, S. K. Banerjee, L. Colombo and R. S. Ruoff, Science **324**, 1312 (2009)
7. X. Li, C. W. Magnuson, A. Venugopal, J. An, J. W. Suk, B. Han, M. Borysiak, W. Cai, A. Velamakanni, Y. Zhu, L. Fu, E. M. Vogel, E. Voelkl, L. Colombo and R. S. Ruoff, Nano Lett. **10**, 4328 (2010)
8. X. Li, C. W. Magnuson, A. Venugopal, R. M. Tromp, J. B. Hannon, E. M. Vogel, L. Colombo and R. S. Ruoff, J. Am. Chem. Soc. **133**, 2816 (2011)
9. A. Reina, X. Jia, J. Ho, D. Nezich, H. Son, V. Bulovic, M. S. Dresselhaus and J. Kong, Nano Lett. **9**, 30 (2008)
10. S. Bae, H. Kim, Y. Lee, X. Xu, J.-S. Park, Y. Zheng, J. Balakrishnan, T. Lei, H. Ri Kim, Y. I. Song, Y.-J. Kim, K. S. Kim, B. Ozyilmaz, J.-H. Ahn, B. H. Hong and S. Iijima, Nat. Nanotechnol. **5**, 574 (2010)

- 11 Q. Yu, L. A. Jauregui, W. Wu, R. Colby, J. Tian, Z. Su, H. Cao, Z. Liu, D. Pandey, D. Wei, T. F. Chung, P. Peng, N. P. Guisinger, E. A. Stach, J. Bao, S.-S. Pei and Y. P. Chen, *Nat Mater.* **10**, 443 (2011)
- 12 A. W. Tsen, L. Brown, M. P. Levendorf, F. Ghahari, P. Y. Huang, R. W. Havener, C. S. Ruiz-Vargas, D. A. Muller, P. Kim and J. Park, *Science* **336**, 1143 (2012)
- 13 P. Y. Huang, C. S. Ruiz-Vargas, A. M. van der Zande, W. S. Whitney, M. P. Levendorf, J. W. Kevek, S. Garg, J. S. Alden, C. J. Hustedt, Y. Zhu, J. Park, P. L. McEuen and D. A. Muller, *Nature* **469**, 389 (2011)
- 14 I. Vlassiuk, M. Regmi, P. Fulvio, S. Dai, P. Datskos, G. Eres and S. Smirnov, *ACS Nano* **5**, 6069 (2011)
- 15 Y. Zhang, Z. Li, P. Kim, L. Zhang and C. Zhou, *ACS Nano* **6**, 126 (2011)
- 16 C. Hwang, K. Yoo, S. J. Kim, E. K. Seo, H. Yu and L. P. Biró, *J. Phys. Chem. C* **115**, 22369 (2011)
- 17 Z. Yan, J. Lin, Z. Peng, Z. Sun, Y. Zhu, L. Li, C. Xiang, E. L. Samuel, C. Kittrell and J. M. Tour, *ACS Nano* **6**, 9110 (2012)
- 18 G. H. Han, F. Güneş, J. J. Bae, E. S. Kim, S. J. Chae, H.-J. Shin, J.-Y. Choi, D. Pribat and Y. H. Lee, *Nano Lett.* **11**, 4144 (2011)
- 19 Z. Luo, Y. Lu, D. W. Singer, M. E. Berck, L. A. Somers, B. R. Goldsmith and A. T. C. Johnson, *Chem. Mater.* **23**, 1441 (2011)
- 20 H. Kim, C. Mattevi, M. R. Calvo, J. C. Oberg, L. Artiglia, S. Agnoli, C. F. Hirjibehedin, M. Chhowalla and E. Saiz, *ACS Nano* **6**, 3614 (2012)
21. W. Zhang, P. Wu, Z. Li and J. Yang, *J. Phys. Chem. C* **115**, 17782 (2011)
- 22 Y. Zhang, L. Zhang, P. Kim, M. Ge, Z. Li and C. Zhou, *Nano Lett.* **12**, 2810 (2012)
- 23 D. M. Dobkin and M. K. Zuraw, *Principles of Chemical Vapor Deposition*,

Springer, (2003)

24 J. D. Anderson and Jr, *Physics Today* **58**, 42 (2005)

25 E. May, R. Berg and M. Moldover, *Int. J. Thermophys.* **28**, 1085 (2007)

26 H. Wang, G. Wang, P. Bao, S. Yang, W. Zhu, X. Xie and W.-J. Zhang, *J. Am. Chem. Soc.* **134**, 3627 (2012)

27 P.-Y. Teng, C.-C. Lu, K. Akiyama-Hasegawa, Y.-C. Lin, C.-H. Yeh, K. Suenaga and P.-W. Chiu, *Nano Lett.* **12**, 1379 (2012)

28 H. N. Hersh, *J. Am. Chem. Soc.* **75**, 1529 (1953)

29 L. Tao, J. Lee, M. Holt, H. Chou, S. J. McDonnell, D. A. Ferrer, M. G. Babenco, R. M. Wallace, S. K. Banerjee, R. S. Ruoff and D. Akinwande, *J. Phys. Chem. C* **116**, 24068 (2012)

30 D. A. Porter, K. K. Easterling, *Phase transformations in metals and alloys*: Chapman & Hall; (1992)

## CHAPTER 6.

### **Mesoepitaxy: Graphene growth on liquid Cu**



## 6.1. Introduction

Two dimensional  $sp^2$ -honeycomb carbon lattice, which is called graphene, has attracted a great attention due to its superior electrical,<sup>1-3</sup> optical<sup>4</sup> and mechanical<sup>5</sup> properties. Among many graphene synthesis methods,<sup>6-11</sup> graphene growth on Cu surface has been actively studied due to its large scale synthesis with monolayer dominant growth mechanism.<sup>12-14</sup> Surface diffusion based chemical vapor deposition (CVD) growth due to negligible carbon solubility enabled large sized graphene single crystal which was possible by suppressing nuclei density at the initial stage of graphene growth.<sup>14</sup> Recently, hundreds of micrometer sized or even mm sized graphene single crystal was obtained by decreasing carbon monomer flux extremely.<sup>15-18</sup> Most of the works have focused on the surface of Cu, especially suppressing heteronuclei effect in graphene growth on Cu catalyst. The Cu substrate is not ideally flat and clean surface, rather it contains considerably many defects such as impurities, scratches formed during foil manufacturing process, and other topological defects. For an example of surface treatment, chemical mechanical planarization (CMP)<sup>19</sup> and electropolishing (EP)<sup>20</sup> were applied for smoothing Cu surfaces. Also, high temperature annealing at atmospheric and high pressure suppressed heteronucleation events and gave large single crystal up to few mm scale.<sup>18,21</sup> However, enlarging crystal size by suppressing nuclei density inevitably limits overall graphene growth rate due to small carbon feeding rate. Continuous graphene can be achieved with extended growth time such as 12 hours or even a couple of days which is not desirable for industrial application.<sup>18</sup>

Geng *et al.*, reported CVD graphene growth on liquid Cu surface. Graphene

synthesis on liquid Cu has unique aspects compared to graphene grown on solid Cu.<sup>22</sup> Control experiments give uniform and self-assembled orientation of each graphene grain. The mechanism of self-assembly is still unclear despite of following studies on graphene/liquid Cu.<sup>23-25</sup> Our group demonstrated the role of liquid Cu catalyst by converting solid Cu to liquid form and observing growth morphologies of graphene on Cu and studying growth kinetics, which will be published soon. In the optimized growth condition, graphene on liquid Cu shows the same orientations with each grains which we expect that would have lower grain boundary areas. Graphene on liquid Cu has some drawbacks such as solidification induced roughness and uneasy transfer due to underlying refractory metals such as W and Mo. Despite of some considerations, graphene growth on liquid Cu needs to be studied since it forms self-assembled hexagon shape graphene easily. In this manuscript, we grew graphene on liquid Cu substrate similar to previous reports,<sup>22-24</sup> and confirmed its grain boundaries after stitching each grain. TEM studies were also investigated to confirm the crystallinity of each grain, and all of the islands were single crystal according to TEM diffraction pattern studies.

In order to prove the grain boundaries of graphene grown on liquid Cu, we prepared continuous graphene layer by two-step growth method. We verified that graphene grown on liquid Cu shows still narrow gap and voids after few hours of growth time due to low supersaturation ratio. Hydrogen etching and NaCl-assisted oxidation was applied in order to reveal grain boundaries of graphene before stitching. Two-step growth enabled continuous graphene with full coverage by increasing methane flux and two step grown samples were not etched by hydrogen. The electrical resistance of graphene on liquid Cu shows lower value compared to

graphene grown on solid Cu if no cracks are observed. Also, simple electrode patterning was enough to prove the resistance of grain boundaries of graphene grown on liquid Cu which shows the same orientation with respect to each other. Resistance of grain boundary of graphene on liquid Cu was not deteriorative compared to grain boundary of graphene on solid Cu.

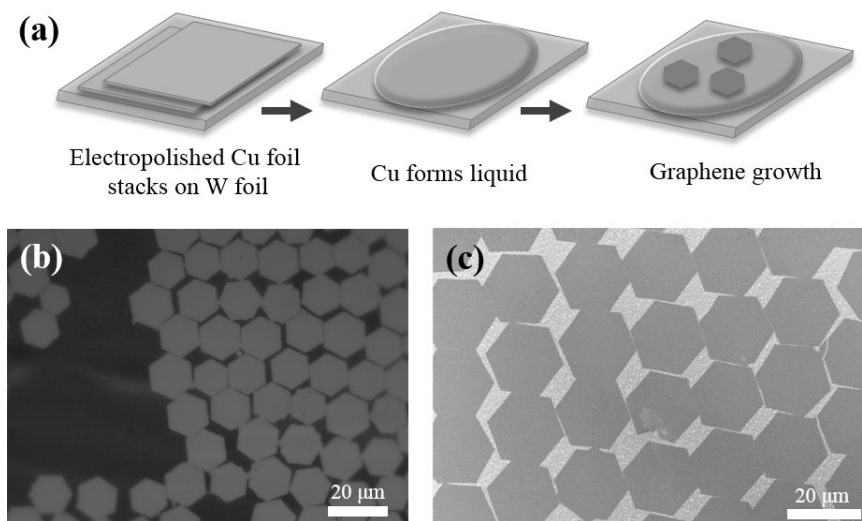


**Figure 6-1.** Schematic illustration of graphene growth on liquid Cu and characterization of graphene growth (a) Schematic illustration of graphene growth on liquid Cu, (b) optical microscope image of as-grown graphene islands on liquid Cu/W support for 30 minutes of growth time showing self-assembled growth behavior, (after oxidizing Cu foil for observation of graphene islands due to selective oxidation) (c) SEM image of graphene grown on liquid Cu. Scale bar indicates 20  $\mu\text{m}$ .

## 6.2. Experimental details

### 6.2.1. Graphene growth on liquid Cu and two-step growth

A couple of electropolished Cu foils (Alfa Aesar 13382) were lied on top of W foil (also, Alfa Aesar). Cu/W samples were loaded into quartz tube type furnace. (Lindberg, blue) Hydrogen was flown at 500 sccm. After reaching target temperature, (1100 °C) Cu melt was formed, and CH<sub>4</sub> was introduced at 3.5 sccm. Growth time was from 30 minutes for partial coverage and longer than 2 hours for full coverage. Hydrogen etching was applied for revealing grain boundaries, which was shutting off CH<sub>4</sub> flux and flowing only H<sub>2</sub>. Hydrogen etching was carried out after cooling to 1050 °C on solid Cu in order to avoid liquid Cu induced effect. For two-step growth, CH<sub>4</sub> flux was increased up to 9 sccm or 12 sccm on liquid (path (i) in Figure 6-2) and on solid (path (ii) in Figure 6-2) Cu.

### 6.2.2. Transfer and VDP (Van der Pauw) pattern fabrication

In order to remove underlying W substrate, anodic etching was used similar to Y. Fan *et al.*'s method. After spin coating PMMA on graphene/Cu/W, sample was connected to anode and bare Cu foil was connected to cathode and constant bias was applied. 30 minutes to 1 hour was enough to remove all the remaining W foil, and PMMA/graphene/Cu was floated on APS solution (0.1 M) for overnight. Floating PMMA/graphene layer was scooped by TEM grid (Quantifoil, Ted Pella) or Si/SiO<sub>2</sub> substrate. For VDP pattern, pre-cut wafer (half of the wafer thickness) was prepared as shown in supporting information. PMMA residue was removed by

direct heating at 350 °C in tube furnace flowing Ar and H<sub>2</sub>. Ti/Au metal was deposition by e-beam evaporation using metal shadow mask, and finally wafer was cut fully. Sheet resistance of 8mm by 8mm sample was measured by Van der Pauw method and Hall mobility was also measured using the same pattern under 0.6 T magnetic field. (HL 5500PC, BIO-RAD)

### **6.2.3. Liftoff and transmission line measurement (TLM) patterning**

After graphene transfer to 285-nm-thick SiO<sub>2</sub>/Si wafer, photoresist coating was carried out by spin-coater. Photoresist (AZ 5214) pattern was formed by typical negative resist recipe and exposure of UV by MA 6-2 aligner. Then, Ti/Au (5 nm / 80 nm) was evaporated on top of photoresist. Liftoff process was done and 2point current/voltage measurement was carried out by Agilent 4156C system.

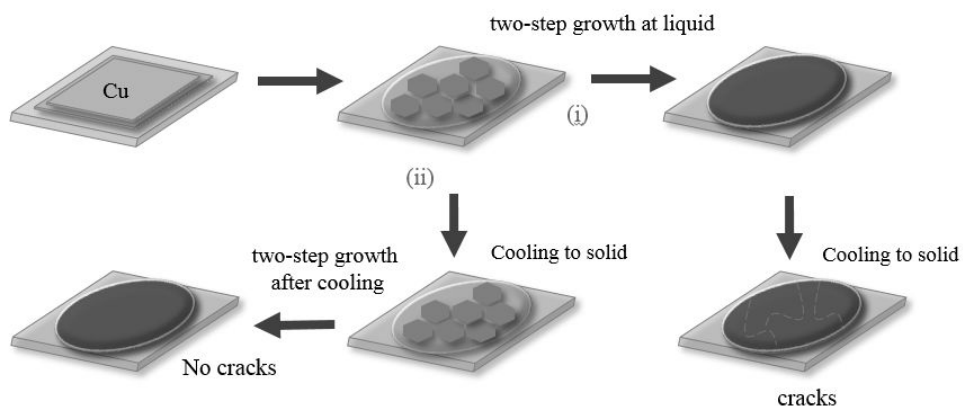


**Figure 6-2.** Schematic illustration of two-step graphene growth on liquid Cu. Process (1) describes continuous graphene layer formation on liquid Cu and followed cooling forms crack due to thermal stress induced by solidification of underlying Cu, and process (2) describes two-step growth after cooling Cu catalyst and no observable cracks formation.

## 6.3. Results and Discussion

### 6.3.1. Structural study of graphene grown on liquid Cu

Graphene was grown on liquid Cu as shown in Figure 6-1(a) and observed by optical microscope and SEM as shown in Figure 6-1 (b) and (c). A couple of pieces of electropolished Cu foils were loaded on top of W support and annealed. Cu was melt to liquid and wets on W substrate as shown in the middle image of Figure 6-1 (a). At optimized growth condition for self-assembled graphene islands, H<sub>2</sub> and CH<sub>4</sub> were flown 500 and 3.5 sccm each in our experiment. After reaching target temperature (1100 °C) which is higher than melting point of Cu (1084 °C) in H<sub>2</sub> atmosphere (500 sccm), CH<sub>4</sub> gas was introduced for graphene growth on liquid Cu. Self-assembled graphene islands were obtained when growth time was 30 minutes as shown in Figure 6-1 (b) and (c), but size discrepancy existed if growth condition was not optimized. (Figure 6-3) Graphene islands tend to aligned well (Figure 6-4) when approaching each other rather than when islands are isolated.

For structural study of graphene grown on liquid Cu, we transferred graphene grown on liquid Cu to Quantifoil TEM grid for observation of diffraction pattern. Figure 6-5 (a) shows SEM image carbon square mesh area of Quantifoil grid where graphene islands are visible by secondary electron contrast. The same area was found in TEM since graphene islands are not easy to observe in TEM bright field mode. Two grains are aligned in the same direction which are indicated by alphabetic letters A, B, C and D, and Arabic number 1, 2, and to 6. With respect to two grains, grain located upper area of TEM image is rotated 11 ° degree. Selected area diffraction patterns were achieved at each position and all the grains were

single crystal. Two neighboring grains show the same orientations of diffraction patterns at all the position, but other grain shows  $11^\circ$  rotated diffraction patterns as shown in Figure 6-5 (c). In the case of Figure 6-6 (a), all the grains are touched each other and aligned in the same axis according to bright field TEM image (and in the SEM), and diffraction patterns were all the same direction regardless of positions.

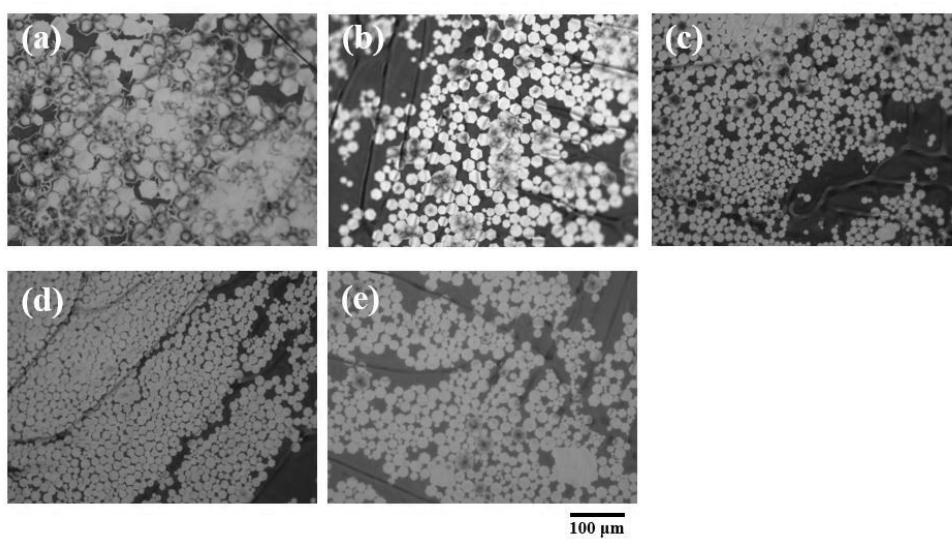


**Figure 6-3.** Optical microscope images of graphene grown on liquid Cu varying  $\text{CH}_4$  flux. (a)  $\text{CH}_4$  flux is 4 sccm, (b) 3.8 sccm, (c) 3.6 sccm, (d) 3.5 sccm, (e) 3.3 sccm, respectively.

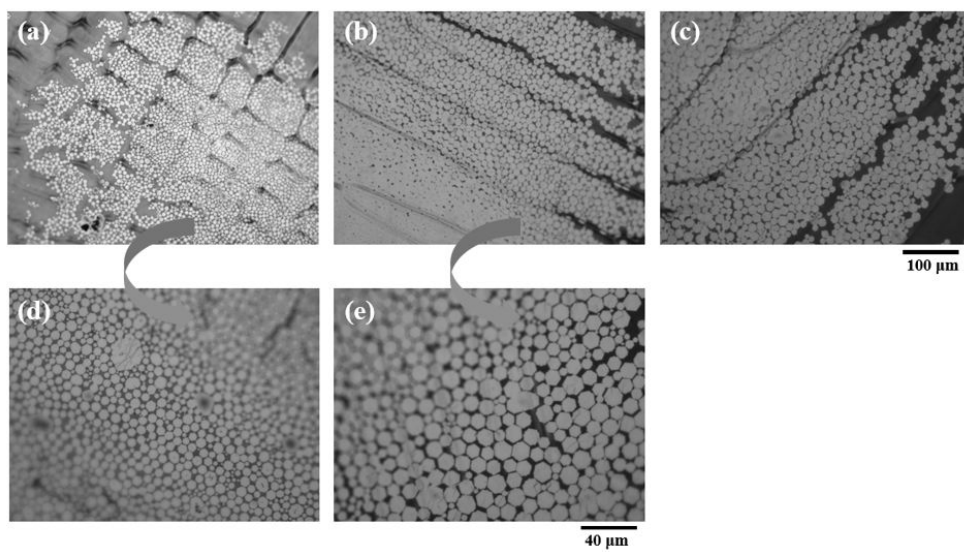


**Figure 6-4.** Optical microscope images of graphene grown on liquid Cu at 5 minutes (a), 10 minutes (b) and 30 minutes (c), and (d) and (e) are magnified image of (a) and (b), respectively.

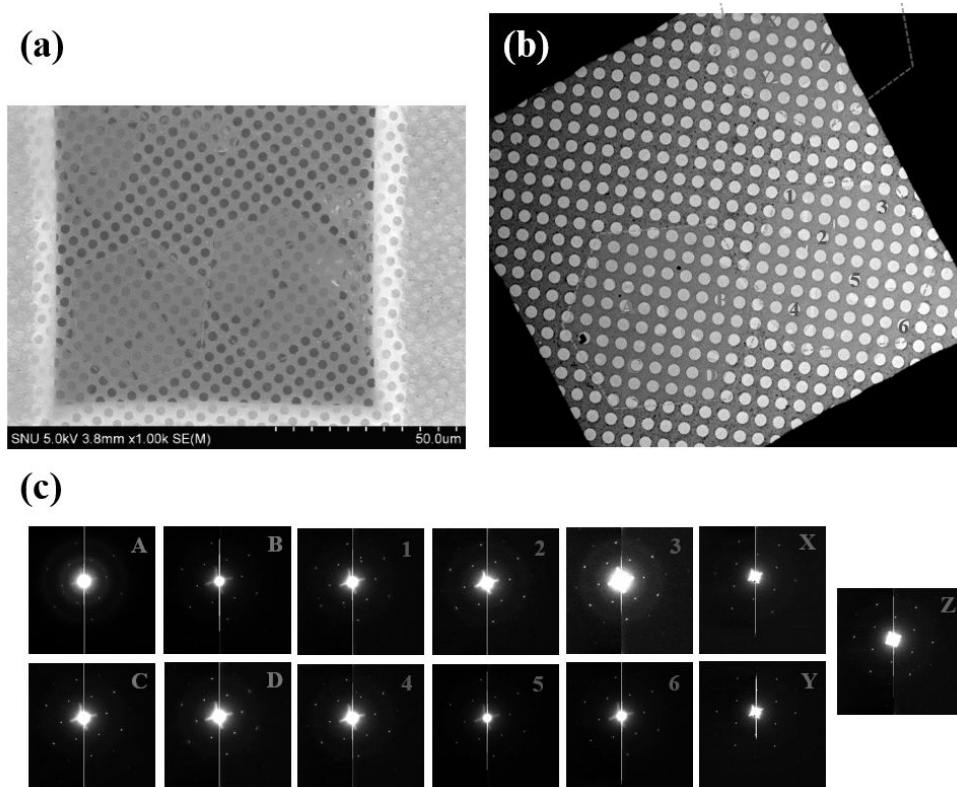


**Figure 6-5.** TEM studies of graphene grown on liquid Cu. (a) SEM image of graphene transferred to Quantifoil TEM grid, (b) TEM bright field image of (a) (images are inverted with respect to vertical axis due to TEM sample loading), and (c) diffraction patterns obtained from various positions marked in (b).

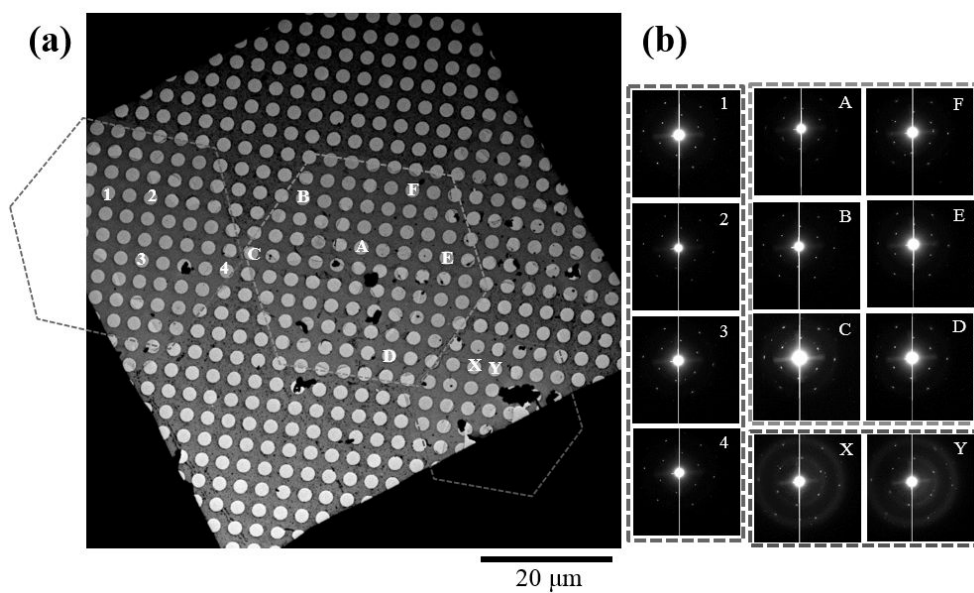


**Figure 6-6.** TEM analysis of three adjacent graphene grains on liquid Cu after transfer to TEM grid, (a) bright field image of grains, and (b) diffraction patterns of each position marked in (a).

### 6.3.2. Revealing grain boundaries of graphene on liquid Cu

Our interest is grain boundaries of two adjacent graphene grains in Figure 6-6 (a) which are aligned in the same direction due to liquid Cu nature. Typical grain boundary is formed by merging of grains having different orientation of atomic arrangement. In order to maintain atomic patchwork quilt, non-hexagon carbon lattices can be formed in the grain boundaries such as heptagon and pentagon.<sup>26-28</sup> The grains in Figure 6-6 look like perfectly aligned in TEM diffraction patterns, but we need to know exact atomic orientations of grain boundaries. For instance, Lee et al., grew graphene on single crystal Ge wafer, which shows epitaxial relationship between graphene and Ge.<sup>29</sup> In order to show grain boundary free graphene, they traced possible grain boundary area and reported that they could not observe any defects on possible grain boundaries. However, exploring all the potential grain boundary regions in TEM is not clever method, thus, we investigated proving transport property of grain boundaries of graphene grown on liquid Cu.

The first method is measuring overall sheet resistance of the continuous graphene layer after forming full coverage film. We continued growth time 2, 3, and even 4 hours as shown in Figure 6-7 (a), but frequently observed narrow gaps and voids as shown in Figure 6-7 (b) and (c) which does not correspond to previous report on graphene growth on liquid Cu.<sup>22</sup> Based on the growth rate of Figure 6-1 (b) and (c), it is suspected that 1 hour of growth time was enough for achieving continuous graphene. Although the growth time was extended up to 4 hours, gaps were observed. Some of the area was fully covered as confirmed in Figure 6-7 (a), but some voids were observed. Also, narrow gaps were identified as shown in

Figure 6-7 (c) and magnified image of Figure 6-7 (d) clearly shows that the narrow gaps are original grain boundaries before merge. We usually have observed graphene growth rate is continuously decreased as growth time goes by. This Johnson-Mehl-Avrami (JMA) type growth<sup>30,31</sup> occurs since exposed Cu areas diminishes as graphene growth goes on. The possible mechanism for voids formation is already reported by few researchers. Li *et al.*, already suggested that carbon flux should be supersaturated for obtaining continuous graphene layer. Small amount of carbon monomer is insufficient to continue driving the C attachment to the island edges and the Cu surface is only partially covered with graphene islands. The vapor phase carbon and carbon on Cu surface are in equilibrium and there is no further driving force for growth to occur. Kim *et al.*, also suggested graphene growth kinetics model and coverage as a function of growth time, which they described final coverage can be expressed as a function of supersaturation ratio. Also, experimental studies of the literature support the statement.<sup>30</sup>

We applied hydrogen induced etching for visualization of grain boundaries of graphene grown on liquid Cu. Effects of hydrogen and hydrogen induced etching have already been studied by several groups.<sup>32,33</sup> For the H<sub>2</sub> etching experiment, CH<sub>4</sub> flow was shut off and only H<sub>2</sub> was flown to chamber for 5 to 10 minutes for clear observation of boundaries. Figure 6-8 (a) shows well-aligned graphene flakes on liquid Cu after 30 minutes of growth, and continuous CH<sub>4</sub> flux for longer than 2 hours gives full coverage (but, still empty area can be observed) graphene as shown in Figure 6-7 (b) and (c). H<sub>2</sub> etching was carried out after solidifying liquid Cu at 1000 °C to avoid liquid Cu induced effect since carbon atom movement is believed to be free on liquid Cu. Figure 6-8 (c) shows typical graphene grain boundaries

revealed by H<sub>2</sub> etching after fully cover (Figure 6-8 (b)). Regardless of growth time, (2 hours of growth time (Figure 6-8 (c)) and 3 hours of growth time (Figure 6-8 (d)) etching effect was clearly visible. It is surprising that original grain boundaries are evidently observable even after forming continuous film as shown in Figure 6-8 (b). It perfectly matches the original graphene islands before stitching to the film. (Figure 6-8 (a), (c) and (d)) The area which etched by H<sub>2</sub> indicate chemically unstable defects compared to perfect hexagonal lattices.

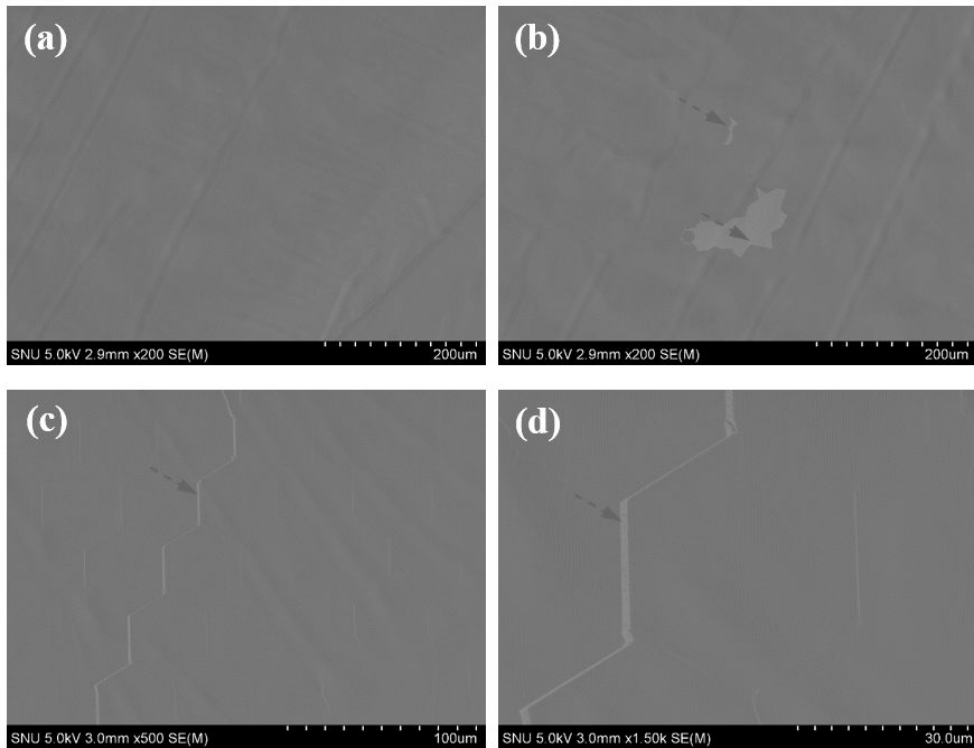


**Figure 6-7.** SEM image of graphene on liquid Cu for 4 hours under optimized condition. (a) Typical graphene film on liquid Cu, (b) visible voids and revealed grain boundaries (indicated by arrows), (c) SEM image of grain boundaries clearly revealed by stopping growth and relatively wide gaps are indicated by arrows and (d) magnified image of (c).

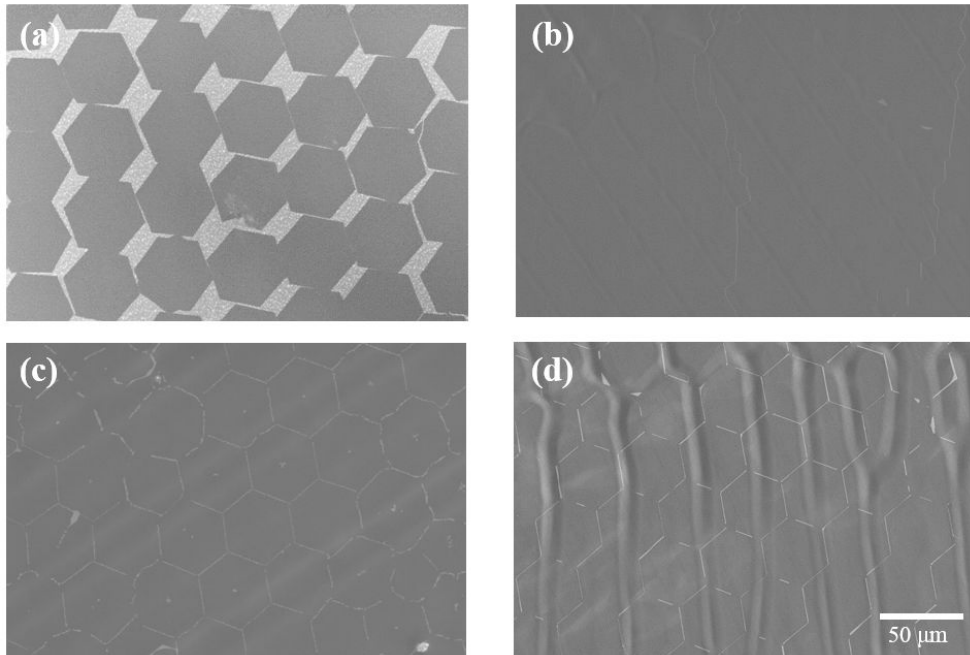


**Figure 6-8.** (a) SEM image of graphene islands after 30 minutes of growth time, (b) SEM image of graphene after 2 hours of growth, (c) SEM image of graphene after H<sub>2</sub> etching for 5 minutes of (b), and (d) SEM image of graphene after 5 minutes H<sub>2</sub> etching

### 6.3.3. Two-step growth for continuous graphene

Our assumption is that narrow gaps still exist between graphene islands due to the reason already mentioned, rather than etching of defect site. In this aspect, we propose two-step growth for continuous graphene formation as illustrated in Figure 6-2. Increasing CH<sub>4</sub> flux at the initial stage of graphene growth is also possible, but the over-flux condition results in multilayer formation (Figure 6-3) and discrepancy of graphene islands which produces less self-assembly of islands. Path (i) depicts two-step growth which increases CH<sub>4</sub> flux in the middle of the synthesizing step, (9 sccm) and continuous graphene was believed to form. However, cracks were observed after cooling to solid and transfer. (Figure 6-9 and 6-10) It is natural that cracks are made due to thermal stress induced by solidification of Cu, because graphene islands were grown on liquid Cu and solidification inevitably results in volume expansion<sup>34</sup> and dendritic shape evolution. (Figure 6-9)<sup>35</sup> Recent study also emphasized crack formation of graphene grown on liquid Cu.<sup>36</sup> On the other hands, path (ii) in Figure 6-2 depicts modified two-step growth, which are increasing CH<sub>4</sub> flux after cooling to solid Cu. Cracks were significantly reduced by two-step growth at solid Cu, the possible reason is that graphene islands are relatively stress-free before coalescence compared to continuous graphene layer since it can release the thermal stress due to spacing between islands. Separate graphene islands are relatively stable after cooling based on supporting information, but continuous film shows cracks. This idea comes from thermal fatigue of steel railway experiencing repeated summer and winter. By making joint and small spacing between steel railway, crack or bending of steel can be avoided. In the same way, graphene islands were cooled down to solid, which release thermal

stress resulted by solidification of Cu, and final gap-fill process can be carried out on solid Cu.

Hydrogen etching was applied to two-step grown graphene and there was no observable grain boundaries revealed by etching as shown in Figure 6-11 (a) and (b). Figure 6-11 (a) shows continuous graphene layer which was formed by two-step growth (ii) in Figure 6-2, and Figure 6-11 (b) shows no etching of graphene. This is significantly different behavior compared to hydrogen etching of graphene grown on liquid Cu as shown in Figure 6-8 which were grown by single step at fixed carbon flux. In order to prove the continuity of the graphene layer, we also used NaCl-assisted oxidation.<sup>37</sup> graphene/Cu/W samples were dipped into in NaCl (6 wt.%) solution and maintained for 24 hours. Grain boundaries revealed by NaCl assisted oxidation are shown in Figure 6-11 (c) for single step growth sample. Compared to Figure 6-11 (c), two-step grown sample in Figure 6-11 (d) did not show considerable oxidation due to gap-fill between graphene islands despite of 1 day of oxidation.

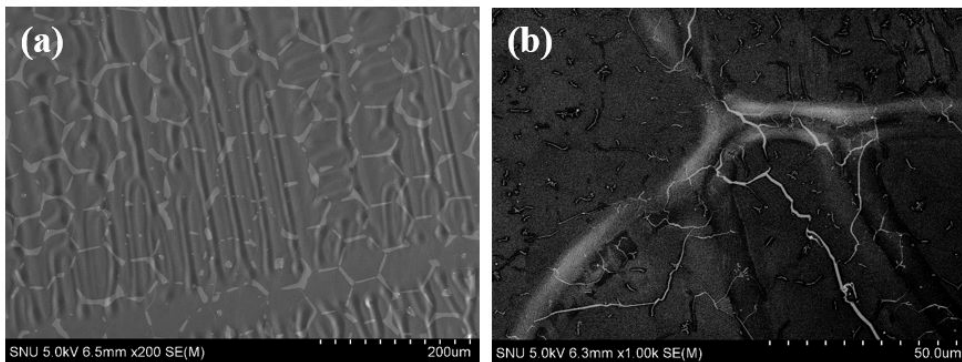


**Figure 6-9.** (a) SEM image of semi-continuous graphene layer (just before stitching) and tearing of graphene islands can be clearly observed by solidification of underlying Cu, (b) SEM image of crack formation on continuous graphene layer which cannot release thermal stress induced solidification of Cu.

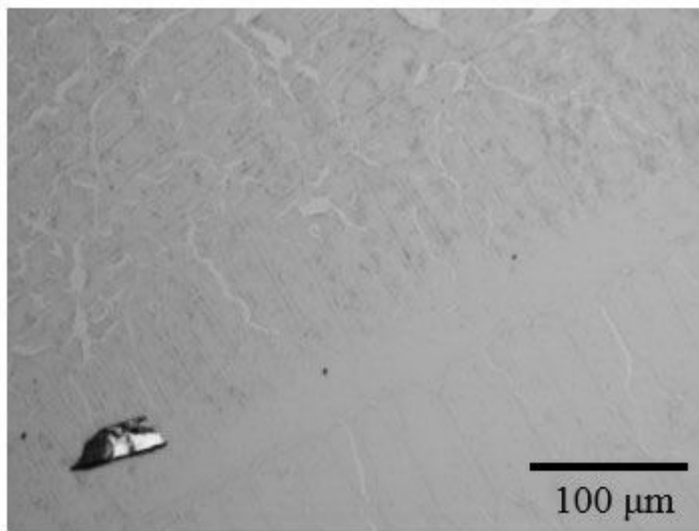


**Figure 6-10.** Optical microscope image of graphene layer transferred to SiO<sub>2</sub>/Si substrate showing crack and tearing due to thermal stress and transfer damage

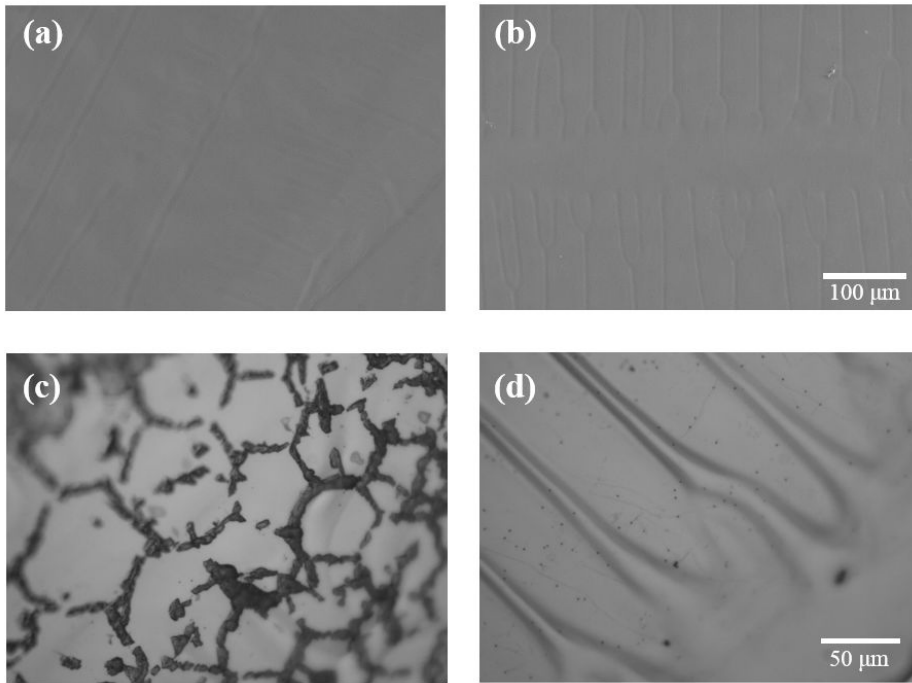


**Figure 6-11.** SEM and optical characterization of continuous graphene layer formation by two-step growth. (a) SEM image of continuous graphene layer grown by two-step method, (b) graphene layer of (a) after experiencing hydrogen etching process, (c) optical microscope image of graphene layer (single step) on Cu after NaCl-assisted oxidation process, (d) optical microscope image of graphene layer on liquid Cu by two-step growth and no damages were observed.

#### 6.3.4. Electrical transport study

Graphene grown on solid Cu can be transferred to Si substrate using typical polymer coating and wet-etching technique. In the case of graphene grown on liquid Cu, underlying W/Mo substrate makes it hard to transfer. Geng *et al.*,<sup>22</sup> used electrochemical bubbling technique,<sup>38,39</sup> but in our experiment, bubbling induced tearing of graphene/PMMA layer and increased overall electrical resistance of the graphene. Also, wet-etching of W used by Mohsin *et al.*,<sup>40</sup> takes few days for removal of whole W underlying substrate. The fastest and damage-free method in our study was anodic etching of W suggested by Fan *et al.*<sup>36</sup> After removing W by anodic etching, remaining PMMA/graphene/Cu was floated on ammonium persulfate (APS) 0.1M solution. After transferring to target substrate, Ti/Au electrode was deposited for making Van der Pauw (VDP) geometry. The results are shown in Figure 6-12 (a) and (b). Crack samples include all the graphene layer containing observable cracks which are coming from transfer damage, solidification induced thermal stress at two-step growth on liquid phase, and even voids for single step growth. No crack samples indicate our two-step growth samples from optimized growth and transfer process. As shown in electrical resistance by VDP method of Figure 6-12 (a), graphene grown on liquid Cu ( $298.1 \pm 93.6 \Omega/\square$ ) shows lower resistance compared to graphene on solid Cu ( $700.7 \pm 472.2 \Omega/\square$ ) if there is no crack and voids. Graphene samples containing cracks show high resistance with larger error bars. ( $1787.5 \pm 1301.8 \Omega/\square$ ) High resistance is natural if cracks exist because conduction path is totally lost. Carrier mobility was also extracted from Hall measurement, which are shown in Figure 6-12 (b). The Hall mobility of graphene grown on solid Cu was  $504.9 \pm 304.2 \text{ cm}^2/\text{V}\cdot\text{sec}$ ,

but graphene grown on liquid Cu gives higher Hall mobility of  $1063.4 \pm 259.7$   $\text{cm}^2/\text{V}\cdot\text{sec}$ . This fact means that when self-assembly occurs on liquid Cu, merge graphene can have better electrical transport behavior due to lower resistance term from aligned grain boundaries.

Direct comparison of Hall mobility of data in Figure 6-12 to previous work is not reasonable since most of the FET and Hall bar mobility are extracted from micrometer scale with patterning process.<sup>12</sup> However, in case of our VDP sample, centimeter scale resistance was measured across the whole area and mobility value can be degraded due to numerous grain boundaries. (Although it is well aligned) In order to prove the grain boundaries effect of graphene on liquid Cu, Ti/Au electrode pattern was deposited on top of two adjacent graphene grains as shown in Figure 6-13 (a). The single crystal graphene size was up to 100  $\mu\text{m}$  scale, thus, e-beam lithography was not needed like previous work.<sup>41</sup> Simple photolithography and lift-off process was enough to form transmission line measurement (TLM, or transfer line method) pattern. Typical current-voltage curve is shown in Figure 6-13 (b) with various length of current paths. There was no observable grain boundaries effect, (around electrode #4 in Figure 6-13 (b)) rather, only length of current path determines the resistance. The resistance of the pattern from position a to c can be calculated from the equation (1) as Q. Yu *et al.*, already discussed,<sup>41</sup>

$$R_{a-c} = \rho_{a-b} \int_a^b \frac{dx}{W(x)} + \rho_{b-c} \int_b^c \frac{dx}{W(x)} \quad \dots 6-(1)$$

Here,  $R_{a-c}$  refers resistance between position a and c,  $\rho$  means resistivity ( $\Omega/\square$  for graphene),  $W$  is width of graphene, and integration of the length between positions make total resistance. Based on the equation 6-(1), the resistivity of left and right grain was 736  $\Omega/\square$  and 1664  $\Omega/\square$ , respectively. The resistivity between electrode 3

and 5 was  $1260 \Omega/\square$  for our measurement, which is not higher than intra-grain resistance. Contrary to typical grain boundaries and abrupt increase of resistance due to degraded transport property, aligned two grains did not show significant resistance increase in I-V curve and value. The Resistance between electrode 3 and 5 ( $R_{3-5}$ ) is  $840 \Omega$ , which is similar to summation of  $R_{3-4}$  and  $R_{4-5}$  ( $800 \Omega$ ) which calculated from two grain resistivity. This fact clearly proves that aligned graphene grains show lower degradation of transport properties despite of grain boundaries formation. Q. Yu *et al.*, made 6 samples for measuring inter-grain resistance, and all of the results show higher resistance when crossing grain boundaries on solid Cu due to random orientation.

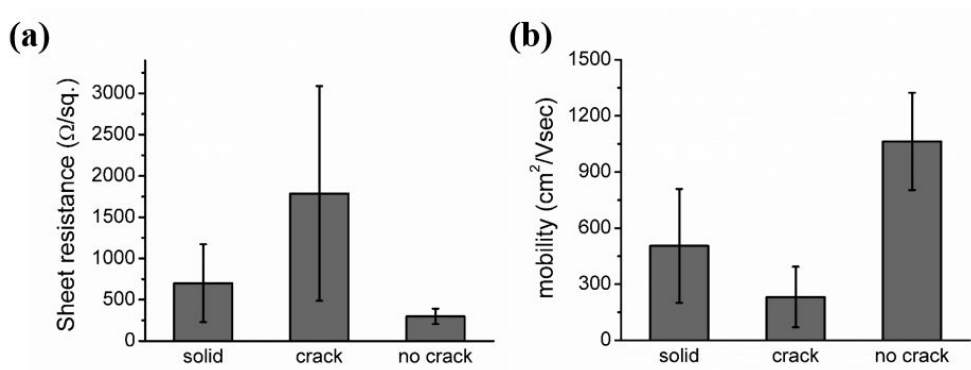


**Figure 6-12.** Comparison of electrical transport properties of graphene grown on solid and liquid Cu. (a) Sheet resistance of graphene grown on typical solid and liquid Cu catalyst, (b) Hall mobility of graphene grown on solid and liquid Cu catalyst.

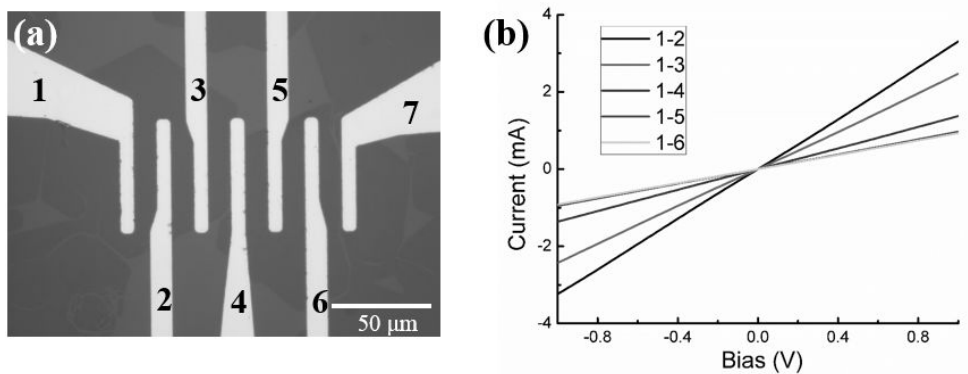


**Figure 6-13.** (a) Optical microscope image of two adjacent graphene islands which aligns in the same orientation and Ti/Au electrodes were deposited by lift-off process, (b) current vs. applied bias curve from electrode #1 to various one including intra- and inter-grain.

## 6.4. Summary and conclusions

As a conclusion, graphene growth on liquid Cu shows self-assembly behavior under well controlled experiment condition. Self-assembly was emphasized via TEM observation and diffraction pattern study. Aligned grains show the same orientation based on diffraction pattern. Even though few hours of growth time, self-assembly graphene did not cover whole area of Cu, which are resulted from low supersaturation ratio which is needed for self-assembly itself for monodisperse size distribution. In order to fully fill the voids between graphene islands on liquid Cu, we introduced two-step graphene growth by increasing carbon flux at the final step of graphene growth. H<sub>2</sub> etching reveals grain boundaries of single step graphene growth samples, but two-step growth samples are not etched by H<sub>2</sub> etching. Also, electrical transport measurement prove high quality of graphene on liquid Cu.

## References

1. K. S. Novoselov, D. Jiang, F. Schedin, T. J. Booth, V. V. Khotkevich, S. V. Morozov and A. K. Geim, Proceedings of the National Academy of Sciences of the United States of America **102** (30), 10451-10453 (2005).
2. K. S. Novoselov, A. K. Geim, S. V. Morozov, D. Jiang, Y. Zhang, S. V. Dubonos, I. V. Grigorieva and A. A. Firsov, Science **306** (5696), 666-669 (2004).
3. A. K. Geim and K. S. Novoselov, Nat. Mater. **6** (3), 183-191 (2007).
4. R. R. Nair, P. Blake, A. N. Grigorenko, K. S. Novoselov, T. J. Booth, T. Stauber, N. M. Peres and A. K. Geim, Science **320** (5881), 1308 (2008).
5. C. Lee, X. Wei, J. W. Kysar and J. Hone, Science **321** (5887), 385-388 (2008).
6. C. Berger, Z. M. Song, X. B. Li, X. S. Wu, N. Brown, C. Naud, D. Mayo, T. B. Li, J. Hass, A. N. Marchenkov, E. H. Conrad, P. N. First and W. A. de Heer, Science **312** (5777), 1191-1196 (2006).
7. W. A. de Heer, C. Berger, X. S. Wu, P. N. First, E. H. Conrad, X. B. Li, T. B. Li, M. Sprinkle, J. Hass, M. L. Sadowski, M. Potemski and G. Martinez, Solid State Commun. **143** (1-2), 92-100 (2007).
8. J. N. Coleman, M. Lotya, A. O'Neill, S. D. Bergin, P. J. King, U. Khan, K. Young, A. Gaucher, S. De, R. J. Smith, I. V. Shvets, S. K. Arora, G. Stanton, H.-Y. Kim, K. Lee, G. T. Kim, G. S. Duesberg, T. Hallam, J. J. Boland, J. J. Wang, J. F. Donegan, J. C. Grunlan, G. Moriarty, A. Shmeliov, R. J. Nicholls, J. M. Perkins, E. M. Grievson, K. Theuwissen, D. W. McComb, P. D. Nellist and V. Nicolosi, Science **331** (6017), 568-571 (2011).
9. Y. Hernandez, V. Nicolosi, M. Lotya, F. M. Blighe, Z. Sun, S. De, I. T. McGovern, B. Holland, M. Byrne, Y. K. Gun'Ko, J. J. Boland, P. Niraj, G.

- Duesberg, S. Krishnamurthy, R. Goodhue, J. Hutchison, V. Scardaci, A. C. Ferrari and J. N. Coleman, *Nat Nano* **3** (9), 563-568 (2008).
10. K. S. Kim, Y. Zhao, H. Jang, S. Y. Lee, J. M. Kim, K. S. Kim, J. H. Ahn, P. Kim, J. Y. Choi and B. H. Hong, *Nature* **457** (7230), 706-710 (2009).
11. Y. Lee, S. Bae, H. Jang, S. Jang, S. E. Zhu, S. H. Sim, Y. I. Song, B. H. Hong and J. H. Ahn, *Nano Lett* **10** (2), 490-493 (2010).
12. X. Li, C. W. Magnuson, A. Venugopal, R. M. Tromp, J. B. Hannon, E. M. Vogel, L. Colombo and R. S. Ruoff, *J. Am. Chem. Soc.* **133** (9), 2816-2819 (2011).
13. X. S. Li, W. W. Cai, J. H. An, S. Kim, J. Nah, D. X. Yang, R. Piner, A. Velamakanni, I. Jung, E. Tutuc, S. K. Banerjee, L. Colombo and R. S. Ruoff, *Science* **324** (5932), 1312-1314 (2009).
14. X. Li, W. Cai, L. Colombo and R. S. Ruoff, *Nano Letters* **9** (12), 4268-4272 (2009).
15. H. Zhou, W. J. Yu, L. Liu, R. Cheng, Y. Chen, X. Huang, Y. Liu, Y. Wang, Y. Huang and X. Duan, *Nat Commun* **4**, 2096 (2013).
16. Y. Hao, M. S. Bharathi, L. Wang, Y. Liu, H. Chen, S. Nie, X. Wang, H. Chou, C. Tan, B. Fallahazad, H. Ramanarayan, C. W. Magnuson, E. Tutuc, B. I. Yakobson, K. F. McCarty, Y. W. Zhang, P. Kim, J. Hone, L. Colombo and R. S. Ruoff, *Science* **342** (6159), 720-723 (2013).
17. L. Gan and Z. Luo, *ACS Nano* **7** (10), 9480-9488 (2013).
18. Z. Yan, J. Lin, Z. Peng, Z. Sun, Y. Zhu, L. Li, C. Xiang, E. L. Samuel, C. Kittrell and J. M. Tour, *ACS Nano* **6** (10), 9110-9117 (2012).
19. G. H. Han, F. Güneş, J. J. Bae, E. S. Kim, S. J. Chae, H.-J. Shin, J.-Y. Choi, D. Pribat and Y. H. Lee, *Nano Letters* **11** (10), 4144-4148 (2011).
20. Z. Luo, Y. Lu, D. W. Singer, M. E. Berck, L. A. Somers, B. R. Goldsmith and A.

- T. C. Johnson, Chem. Mater. **23** (6), 1441-1447 (2011).
21. H. Wang, G. Wang, P. Bao, S. Yang, W. Zhu, X. Xie and W.-J. Zhang, J. Am. Chem. Soc. **134** (8), 3627-3630 (2012).
22. D. Geng, B. Wu, Y. Guo, L. Huang, Y. Xue, J. Chen, G. Yu, L. Jiang, W. Hu and Y. Liu, Proceedings of the National Academy of Sciences of the United States of America **109** (21), 7992-7996 (2012).
23. D. Geng, B. Luo, J. Xu, Y. Guo, B. Wu, W. Hu, Y. Liu and G. Yu, Adv. Funct. Mater. **24** (12), 1664-1670 (2014).
24. B. Wu, D. Geng, Z. Xu, Y. Guo, L. Huang, Y. Xue, J. Chen, G. Yu and Y. Liu, NPG Asia Mater **5**, e36 (2013).
25. D. Geng, L. Meng, B. Chen, E. Gao, W. Yan, H. Yan, B. Luo, J. Xu, H. Wang, Z. Mao, Z. Xu, L. He, Z. Zhang, L. Peng and G. Yu, Adv. Mater., n/a-n/a (2014).
26. P. Y. Huang, C. S. Ruiz-Vargas, A. M. van der Zande, W. S. Whitney, M. P. Levendorf, J. W. Kevek, S. Garg, J. S. Alden, C. J. Hustedt, Y. Zhu, J. Park, P. L. McEuen and D. A. Muller, Nature **469** (7330), 389-392 (2011).
27. K. Kim, Z. Lee, W. Regan, C. Kisielowski, M. F. Crommie and A. Zettl, ACS Nano **5** (3), 2142-2146 (2011).
28. P. Nemes-Incze, K. J. Yoo, L. Tapasztó, G. Dobrik, J. Lábár, Z. E. Horváth, C. Hwang and L. P. Biró, *Revealing the grain structure of graphene grown by chemical vapor deposition*. (AIP, 2011).
29. J. H. Lee, E. K. Lee, W. J. Joo, Y. Jang, B. S. Kim, J. Y. Lim, S. H. Choi, S. J. Ahn, J. R. Ahn, M. H. Park, C. W. Yang, B. L. Choi, S. W. Hwang and D. Whang, Science **344** (6181), 286-289 (2014).
30. H. Kim, C. Mattevi, M. R. Calvo, J. C. Oberg, L. Artiglia, S. Agnoli, C. F. Hirjibehedin, M. Chhowalla and E. Saiz, ACS Nano **6** (4), 3614-3623 (2012).

31. G. Eres, M. Regmi, C. M. Rouleau, J. Chen, I. N. Ivanov, A. A. Puzetzkyy and D. B. Geohegan, *ACS Nano* **8** (6), 5657-5669 (2014).
32. I. Vlassioul, M. Regmi, P. Fulvio, S. Dai, P. Datskos, G. Eres and S. Smirnov, *ACS Nano* **5** (7), 6069-6076 (2011).
33. Y. Zhang, Z. Li, P. Kim, L. Zhang and C. Zhou, *ACS Nano* **6** (1), 126-132 (2011).
34. J. A. Cahill and A. D. Kirshenbaum, *The Journal of Physical Chemistry* **66** (6), 1080-1082 (1962).
35. J. J. Hoyt, M. Asta and A. Karma, *Materials Science and Engineering: R: Reports* **41** (6), 121-163 (2003).
36. Y. Fan, K. He, H. Tan, S. Speller and J. H. Warner, *Chem. Mater.* **26** (17), 4984-4991 (2014).
37. T. H. Ly, D. L. Duong, Q. H. Ta, F. Yao, Q. A. Vu, H. Y. Jeong, S. H. Chae and Y. H. Lee, *Adv. Funct. Mater.* **23** (41), 5183-5189 (2013).
38. Y. Wang, Y. Zheng, X. Xu, E. Dubuisson, Q. Bao, J. Lu and K. P. Loh, *ACS Nano* **5** (12), 9927-9933 (2011).
39. L. Gao, W. Ren, H. Xu, L. Jin, Z. Wang, T. Ma, L.-P. Ma, Z. Zhang, Q. Fu, L.-M. Peng, X. Bao and H.-M. Cheng, *Nat Commun* **3**, 699 (2012).
40. A. Mohsin, L. Liu, P. Liu, W. Deng, I. N. Ivanov, G. Li, O. E. Dyck, G. Duscher, J. R. Dunlap, K. Xiao and G. Gu, *ACS Nano* **7** (10), 8924-8931 (2013).
41. Q. Yu, L. A. Jauregui, W. Wu, R. Colby, J. Tian, Z. Su, H. Cao, Z. Liu, D. Pandey, D. Wei, T. F. Chung, P. Peng, N. P. Guisinger, E. A. Stach, J. Bao, S.-S. Pei and Y. P. Chen, *Nat Mater* **10** (6), 443-449 (2011).



## CHAPTER 7.

### **Summary, Conclusions**



After discovery of two-dimensional graphene lattice by micromechanical exfoliation, alternative graphene growth methods have been suggested. Among them, chemical vapor deposition enables large scale and reproducible graphene synthesis on catalytic metal. Despite of many advantages of graphene synthesis by CVD, two main problems need to be solved in terms of materials science. First one is transfer-free graphene growth on target substrate and second one is polycrystalline nature.

In this dissertation, fundamental understanding on graphene synthesis on Cu surfaces was done including review on graphene growth. Unique aspects of graphene growth were dealt with such as Johnson-Mehl Avrami type growth and role of metal catalyst. Many empirical factors for graphene growth were studied in chapter 2. Effect of source gas feeding rate, temperature, surface roughness of catalytic metal, morphology evolution, hydrogen induced etching, and several pioneering work in graphene growth were discussed.

As an approach for transfer-free growth on target substrate, direct graphene synthesis by metal-induced crystallization of a-C was studied in chapter 3. Combining agglomeration behavior of thin metal and metal-induced crystallization of a-C, graphene was grown on dielectric surface via few seconds of heating. Ultra-thin metal (3~10 nm) reacts with a-C and crystallize it to graphene and metal itself agglomerates. Thus, rapid annealing of bilayer of a-C and Ni deposited on SiO<sub>2</sub> or quartz substrate leads to the formation of graphene-metal hybrid film which can be used as transparent conducting film. Basic property of transparent conducting film such as transparency at visible wavelength and electrical resistance were measured and growth mechanism of graphene-metal composite was studied via overall performance.

Also, carburizing Si substrate forms graphene layer on Si substrate by simple heating in chapter 4. Various orientations of Si wafer ((100), (110), and (111)) were prepared and we found that Si (110) substrate forms 3C-SiC(111) surfaces by simple heating with  $C_2H_4$  gas. Direct carbon deposition enables few layer graphene/3C-SiC(111)/Si(110) epitaxial interface and crystallographic study revealed that it is well matched having lattice mismatch less than 2 %. The surface consists of hexagonal array that can act as a template for graphene growth and finally graphene layers were formed on SiC/Si substrate.

As an approach for overcoming polycrystalline nature of graphene growth and understanding growth mechanism, in chapter 5, gas transport was investigated via employing micrometer scale gap jig. Due to the small size of the gap, a boundary layer is believed to develop inside the gap, and gas molecule transport is controlled by molecular flow. Three effects of jig gap was shown as below. The first one is suppression of Cu evaporation during graphene growth and smoothing Cu surface which are the result of static vapor environment inside the jig gap. The second one is gas conductance control which was proved by graphene coverage vs. jig gap and distance graph. Dividing coverage term by nuclei density and growth rate reveals that heteronuclei effect governs graphene growth. The last one is morphology control due to source gas depletion in the jig gap and hydrogen-induced etching. Graphene growth morphology was sharper in the jig gap forming hexagon shape compared to graphene morphology outside the jig gap showing dendritic shape.

In chapter 6, as a concept for Mesoepitaxy, graphene growth on liquid Cu was investigated. Suppressing nuclei density and enlarging grain size is limited due to low gas feeding rate and resulted slow grain growth rate. Graphene growth on liquid Cu shows self-assembly behavior under well controlled condition. In order

to obtain full coverage graphene layer on liquid Cu, two step growth concept was introduced and confirmed the continuity of film by H<sub>2</sub> etching and NaCl oxidation. Two-step growth was developed under the assumption that supersaturation ratio cannot build up if carbon monomer supply is lower than critical limit. Also, TEM study emphasizes self-assembly of graphene islands on liquid Cu by diffraction pattern analysis. Overall performance of graphene's electrical transport on liquid Cu was compared to typical graphene on solid Cu after transfer.

In summary, two novel graphene growth methods were developed in order to overcome transfer process. Also, with the fundamental understanding on graphene growth, approaches for solving polycrystalline nature of graphene were suggested in terms of suppressing nuclei density and Mesoepitaxy.



## Abstract (in Korean)

본 학위 논문에서는, 두 가지 그래핀 성장에서의 화두에 대해 접근하고 이를 해결하고자 진행한 연구에 대해 언급하였다. 첫 번째 화두는 바로 전사 공정이 제거된 그래핀의 성장이며, 다른 하나의 화두는 그래핀 합성에서의 임의의 방향을 가지는 핵의 생성 및 성장으로 인한 다결정 형성의 문제이다. 첫 번째 화두는 주로 3 장과 4 장에서 다루었으며 두 번째 화두는 5 장과 6 장에서 다루었다.

서론에서는, 우선 그래핀 자체의 물성 및 여러 특성에 대한 언급과 더불어, 그래핀을 주목 받도록 한 기계적 박리법을 극복하기 위한 여러 그래핀 성장 방법에 대해서 소개하였다. 각각의 성장 방법의 장단점에 대해 소개하고, 이 중에 본 논문에서 연구한 화학기상증착법으로 그래핀을 성장할 때의 문제점에 대해서 언급하였다. 구리 위에서 그래핀 성장을 하는 경우에 일반적인 학문적 연구와 더불어, 이전 논문들에서 어떠한 식으로 그래핀 성장에 대해 접근하는지에 대한 선행 연구를 소개하였다. 그래핀의 성장 메커니즘에 대한 기본적인 이해를 돕고, 열역학 및 속도론적 관점에서 어떠한 부분에 대한 이해를 하였는지 언급하였다. 가장 문제가 되는, 다결정의 그래핀이 형성되는 원인에 대해 분석하고 단결정 혹은 결정립의 크기가 큰 그래핀을 얻기 위해 어떠한 점들이 고려되어야 하는지에 대하여 분석하였다. 특히 2 장에서는 결정립의 크기가 큰 그래핀을 얻기 위한 다른 논문들에 대해 연구한 바를 요약하였으며 온도나 기판, 탄화수소의 공급, 압력 등이 그래핀 성장에 미치는 영향에 대해 언급하였다.

3 장에서는, 전사가 필요 없이 원하는 기판 위에 그래핀을 바로 형성하는 시도로써, 금속을 통한 반도체의 결정화 방법과 얇은 금속의 응집 현상 두 가지를 복합하여 그래핀과 금속의 하이브리드 구조를 형성한 방법에 대해 설명하였다. 니켈과 비정질 탄소를 증착한 이후에 이를 급속 열처리하여 비정질 탄소는 결정질이 그래핀으로 변화하고 얇은 금속은 응집현상을 통해 해체되도록 하여 그래핀과 금속의 하이브리드 구조를 형성하면 높은 투과도와 그래핀의 형성으로 인한 전기 전도도를 얻을 수 있으며, 이로 인해 형성된 그래핀의 가시광선 영역에서의 투과도 및 면저항을 분석하였다. 또한 분석한 바를 토대로, 얇은 금속 박막을 이용해 그래핀을 형성할 때의 메커니즘에 대한 이해도 진행하였다.

4 장에서는, 실리콘 기판 위에 바로 그래핀을 형성하기 위한 시도로써, 실리콘 기판 위에 탄화수소 기체를 주입하여 바로 그래핀이 증착되는 연구에 대해 언급하였다. 탄화수소 가스의 주입에 의해 실리콘 (110) 면은 3C-SiC (111) 면으로 대체되었으며, 이 위에 그래핀이 증착되는 것을 FT-IR 및 Raman 스펙트럼을 통해 확인할 수 있었다. 투과전자현미경 분석을 통해 그래핀/3C-SiC(111)/Si(110) 의 epitaxial relationship 을 분석하였으며, 3C-SiC (111) 과 Si (110) 면의 경우 격자의 불일치가 2%이기 때문에 비교적 잘 형성됨을 알 수 있었다.

5 장에서는 구리 촉매 위에서의 그래핀 성장의 다결정 형성에 관한 연구로써, 그래핀 성장에 있어서 기체 수송의 역할에 대해 연구하기 위하여 micrometer gap 을 가지는 jig 를 고안하여 이를 통해 그래핀 성장에 미치는 역할을 분석하였다. Jig 안에서의 small gap 으로 인하여

기체 수송이 molecular flow 에 의해 지배 받는다고 생각하였으며, jig 의 3 가지 효과에 대해 보고하였다. 첫 번째 jig 의 효과는, 우선 정적인 기체 흐름의 형성으로 인하여 구리의 승화 현상이 대폭 감소하여 표면의 거칠기가 완화되었다. 두 번째로, 기체 수송을 효과적으로 조절하여 그래핀 성장에 영향을 미쳤으며 핵의 밀도 및 결정립의 크기로 나누어 분석하였을 때, 핵의 밀도에는 영향을 미치지 않는 것을 통해 heteronuclei 영향이 그래핀 성장을 지배하는 것을 알았다. 마지막으로, 탄화수소 기체가 jig 안에서 계속 고갈됨에 따라 상대적으로 수소의 양이 많아져서 식각에 의한 영향이 나타났고, 이로 인해 그래핀이 자라는 형태가 dendritic 모양에서 육각형의 가장자리가 정돈되어 있는 형태로 변하는 것을 확인할 수 있었다.

6 장에서는 이전에 그래핀 성장에서 많이 치우쳐 있던 시도인, 초기 핵 생성의 밀도를 줄여서 결정립 자체의 키움에 따라 결정립계를 줄이는 방법의 경우, 성장 속도 또한 필연적으로 낮아질 수 밖에 없는 점에 대해 지적하였고, 이를 해결하기 위해 액체 구리 위에서의 그래핀 성장인 Mesoepitaxy 에 대해 연구하였다. 액체 구리 위에서 그래핀 성장 조건을 확립하고 자라는 mechanism 에 대해 분석하였으며, 자가배열이 잘 일어나는 조건의 경우, 과포화도가 낮기 때문에 결정립 사이에 틈이 있는 것을 확인하여 two-step 성장 조건을 확립하여 진정한 의미에서의 full coverage 그래핀을 형성하였다. 또한, 투과전자현미경 분석을 통해 자가배열이 잘 되는 경우와 그렇지 않은 경우에 회절 패턴을 분석하였다. 그래핀의 결정립이 같은 방향으로 만나는 경우에 있어서 간접적으로 저항을 측정하여 결정립의 저항 성분이 무시할 만큼 작은 것을 보였으며,

기존의 결정립과 다른 특성을 보고하였다.

**주요어:** 그래핀, 투명 전극, 전사 공정, direct formation, 실리콘 카바이드, 니켈, 구리, 핵 생성 및 성장, heteronuclei, 기체 수송, jig, Mesoepitaxy, 액체 구리, 자가배열

**학번:** 2009-20638

## List of publications

### Papers

- (1) Seong-Yong Cho, Min-Sik Kim, Min-Su Kim, Ki-Ju Kim, Hyun-Mi Kim and Ki-Bum Kim, "Proving transport behavior of graphene grown on liquid Cu", *submitted*.
- (2) Ki-Ju Kim, Seong-Yong Cho, Hyun-Mi Kim, Hyoji Choi, and Ki-Bum Kim, "Direct graphene growth on SiO<sub>2</sub>/Si substrate by using carbon diffusion barrier", *to be submitted*.
- (3) Min-Sik Kim, Seong-Yong Cho, Ki-Ju Kim, Hyun-Mi Kim, and Ki-Bum Kim, "Liquid Cu catalyst effect on graphene growth", *under preparation*.
- (4) Min-Hyun Lee, Ashvani Kumar, Kyeong-Beom Park, Seong-Yong Cho, Hyun-Mi Kim, Min-cheol Lim, Young-Rok Kim and Ki-Bum Kim, "A low-noise solid-state nanopore platform based on a highly insulating substrate", *Scientific report* 4, 7448 (2014).
- (5) Do-Joong Lee, Jangyeon Kwon, Jiyeon Kim, Ki-Ju Kim, Yeong-Ho Cho, Seong-Yong Cho, Soo-Hyun Kim, Jimmy Xu and Ki-Bum Kim, "Ultrasmooth, high electron mobility amorphous In-Zn-O films grown by atomic layer deposition", *The Journal of Physical Chemistry C* 118, 408 (2013).
- (6) Seong-Yong Cho, Ki-Ju Kim, Hyun-Mi Kim, Do-Joong Lee, Min-Hyun Lee, and Ki-Bum Kim, "Gas transport controlled synthesis of graphene by employing a micro-meter scale gap jig", *RSC Advances* 3, 26376 (2013).

- (7) **Seong-Yong Cho**, Hyun-Mi Kim, Min-Hyun Lee, Do-Joong Lee, and Ki-Bum Kim, “Single step formation of a graphene-metal hybrid transparent and electrically conductive film”, *Nanotechnology* 23, 115301 (2012).
- (8) **Seong-Yong Cho**, Hyun-Mi Kim, Min-Hyun Lee, Do-Joong Lee, and Ki-Bum Kim, “Direct formation of graphene layers on top of SiC during carburization of Si substrate”, *Current Applied Physics* 12 1088 (2012).
- (9) Min-Hyun Lee, Hyun-Mi Kim, **Seong-Yong Cho**, Kipil Lim, Soo-Yeon Park, Jae Jong Lee and Ki-Bum Kim, “Fabrication of ultra-high-density nanodot array patterns (~3 Tbits/in.2)”, *The Journal of Vacuum Science and Technology B* 29, 061602 (2011).

## **Patents**

1. K. B. Kim, H. Lee, H. M. Kim, **S. Y. Cho**, “Graphene structure, method of forming the graphene structure, and transparent electrode including the graphene structure” PCT/KR2011/001642
2. “그래핀 구조, 그 제조 방법 및 그래핀 구조를 이용한 투명 전극 (Graphene structure, method of the same and transparent electrode using the graphene structure)” 김기범, 이흥희, 김현미, **조성용**, 2010-1197639
3. “성장 방향이 제어된 그래핀의 제조 방법 (method for manufacturing graphene with controlling a direction of growth)” 김기범, **조성용**, 김기주, 2012-0010384
4. “국부적인 촉매의 상변환을 이용해서 특성이 향상된 그래핀 제조방법” 김기범, 김민식, **조성용**, 출원중

## **First author presentations**

- (1) **Seong-Yong Cho**, Ki-Ju Kim, Min-Sik Kim, Min-Su Kim and Ki-Bum Kim, “Study on Mesoepitaxy: graphene growth on liquid Cu” ENGE 2014 (international)
- (2) **Seong-Yong Cho**, Ki-Ju Kim, Hyun-Mi Kim, Do-Joong Lee, Min-Hyun Lee, and Ki-Bum Kim, “Gas transport controlled synthesis of graphene by employing a micro-meter scale gap jig” MRS Spring meeting 2014 (international)
- (3) **Seong-Yong Cho**, Ki-Ju Kim, Hong H. Lee, and Ki-Bum Kim, “Effect of gas transport inside a micrometer-scale gap jig on the growth of graphene on copper foil” Nano Korea 2013 (international)
- (4) **Seong-Yong Cho**, Ki-Ju Kim, Hong H. Lee, and Ki-Bum Kim, “Gas transport controlled synthesis of graphene by chemical vapor deposition on copper foil: Micro-meter gap jig effect” MRS (international) Fall meeting 2012
- (5) **Seong-Yong Cho**, Hyun-Mi Kim, Min-Hyun Lee, Do-Joong Lee, and Ki-Bum Kim, “Single step formation of graphene-metal hybrid transparent conductive film” IEEE NMDC 2011 (international)
- (6) **Seong-Yong Cho**, Hyun-Mi Kim, Min-Hyun Lee, Do-Joong Lee, and Ki-Bum Kim, “Direct graphene growth by carbon deposition on Si substrates and its orientations dependence” Korean conference on semiconductors 2011 (domestic)
- (7) **Seong-Yong Cho**, Hyun-Mi Kim, Min-Hyun Lee, Do-Joong Lee, Hong H. Lee, and Ki-Bum Kim, “Direct graphene formation on dielectric substrates by metal-induced crystallization” MRS Spring meeting 2011 (international)